



CONTINUOUS PHOTOCATALYTIC FUEL PRODUCTION OVER WIDE-BANDGAP METAL OXIDES.

Antonio Bazzo

Dipòsit Legal: T 1544-2014

ADVERTIMENT. L'accés als continguts d'aquesta tesi doctoral i la seva utilització ha de respectar els drets de la persona autora. Pot ser utilitzada per a consulta o estudi personal, així com en activitats o materials d'investigació i docència en els termes establerts a l'art. 32 del Text Refós de la Llei de Propietat Intel·lectual (RDL 1/1996). Per altres utilitzacions es requereix l'autorització prèvia i expressa de la persona autora. En qualsevol cas, en la utilització dels seus continguts caldrà indicar de forma clara el nom i cognoms de la persona autora i el títol de la tesi doctoral. No s'autoritza la seva reproducció o altres formes d'explotació efectuades amb finalitats de lucre ni la seva comunicació pública des d'un lloc aliè al servei TDX. Tampoc s'autoritza la presentació del seu contingut en una finestra o marc aliè a TDX (framing). Aquesta reserva de drets afecta tant als continguts de la tesi com als seus resums i índexs.

ADVERTENCIA. El acceso a los contenidos de esta tesis doctoral y su utilización debe respetar los derechos de la persona autora. Puede ser utilizada para consulta o estudio personal, así como en actividades o materiales de investigación y docencia en los términos establecidos en el art. 32 del Texto Refundido de la Ley de Propiedad Intelectual (RDL 1/1996). Para otros usos se requiere la autorización previa y expresa de la persona autora. En cualquier caso, en la utilización de sus contenidos se deberá indicar de forma clara el nombre y apellidos de la persona autora y el título de la tesis doctoral. No se autoriza su reproducción u otras formas de explotación efectuadas con fines lucrativos ni su comunicación pública desde un sitio ajeno al servicio TDR. Tampoco se autoriza la presentación de su contenido en una ventana o marco ajeno a TDR (framing). Esta reserva de derechos afecta tanto al contenido de la tesis como a sus resúmenes e índices.

WARNING. Access to the contents of this doctoral thesis and its use must respect the rights of the author. It can be used for reference or private study, as well as research and learning activities or materials in the terms established by the 32nd article of the Spanish Consolidated Copyright Act (RDL 1/1996). Express and previous authorization of the author is required for any other uses. In any case, when using its content, full name of the author and title of the thesis must be clearly indicated. Reproduction or other forms of for profit use or public communication from outside TDX service is not allowed. Presentation of its content in a window or frame external to TDX (framing) is not authorized either. These rights affect both the content of the thesis and its abstracts and indexes.

CONTINUOUS PHOTOCATALYTIC FUEL PRODUCTION OVER WIDE-BANDGAP METAL OXIDES



UNIVERSITAT
ROVIRA I VIRGILI

ANTONIO BAZZO

Doctoral Thesis
2014



DOCTORAL THESIS

Continuous Photocatalytic Fuel Production Over Wide-Bandgap Metal Oxides

ANTONIO BAZZO

Supervised by:

Dr. Atsushi Urakawa

ICIQ-URV



UNIVERSITAT ROVIRA I VIRGILI

Tarragona

2014

Dr. Atsushi Urakawa,
Group Leader
Institute of Chemical Research of Catalonia (ICIQ)
Av Països Catalans 16
43007 Tarragona, Spain

CERTIFIES

that the present work, entitled “Continuous photocatalytic fuel production over wide-bandgap metal oxides”, presented by Antonio Bazzo for the award of the degree of doctor, has been carried out under his supervision at Institute of Chemical Research of Catalonia (ICIQ), and that it fulfils all the requirements to obtain the degree of Doctor in Chemical Science and Technology.

Tarragona, 21st May 2014

浦川 篤

Dr. Atsushi Urakawa



UNIVERSITAT ROVIRA I VIRGILI

*“The sun was shining on the sea,
Shining with all his might:
He did his very best to make
The billows smooth and bright—
And this was odd, because it was
The middle of the night.
...”*

Lewis Carrol

1872

ACKNOWLEDGEMENTS

First of all, I would like to deeply thank my supervisor, Dr. Atsushi Urakawa, for giving me the opportunity to undertake my doctoral studies in his new-born group. I am really grateful for having being honoured from the beginning with his trust, allowing for freedom of exploration as well as the best motivation. I am grateful to him for the intense multidisciplinary discussions, his expert guidance, and his heartfelt interest for my improvement. In these years I learnt the valuable life lesson to feel responsible for my decisions and pursue my goals. Thank you also for the opportunities I had to enrich my scientific and communication expertise in our missions to synchrotron facilities and international conferences. Last but not least I would like to give special thanks for the few late Friday acoustic live lab sessions.

I would like to express my sincere gratitude to the ICIQ and its staff as a whole, for making this unique institution work as a charm. Special thanks go to the technical/scientific support for accommodating the most unusual requests and providing constant support. In particular, I am really grateful to Miguel Gonzalez for his everlasting support and patience. Without his generous flexibility and always kind character, this project could not start or develop by any means. Thanks to Xavi Asensio and José Luis León for making possible the impossible, with glass, metal and plastic: I really enjoyed the designing and making process in your company, as much as I enjoyed the nattering. Also special thanks to the Spectroscopy, Chemical Reaction Technology, and X-Ray units crews for their great job and highly professional help.

The next thoughts go to the lab-family. Especially, the other two pioneering PhD students with whom I started sailing in unknown waters four years ago: Jordi Ampurdanés and Atul Bansode. And the not much later joining (la-Piri)Dina

Fakhrnasova. The kilometres of roads we walked together paved our paths into one. One page is not enough to explain the list of nicknames, slang terms and jokes we forged during this time together. The complicity, the reciprocal support in very challenging times, as well as the perpetual mutual dissing is a very unique treasure that I will always keep with me, wherever I will end up springing. Thank you for every moment shared together. I also would like to thank all the other journey mates that were stopping by in P2.11. Special mention for Noelia Barrabés, Bertam Kimmerle and Sven(y) Reimann that shared their scientific and life experience in the most generous way, and greatly supported in the early days. Joon-ki Choi for being such a nice element and a delicatessen lover. A big hug to the present colleagues Luis, Sergio (Thor), (mini) Sergio, Dragos, Rohit, and Rezza for continuing making the lab a warm and fun place to stay. Thanks to Aurora for her solid irreplaceable support. To Ta, because she knew us and had the stamina to come back. Also, the lab would not be the same without the presence of such good neighbours in the all floor 2 phase 2. Special credit goes to (escooty)Pep and Caye for smooth and acclaimed shuttling through the lab with heavy loads. Super special credit to Asraa Ziadi for making life sparkling in and out ICIQ, being such a cracking human being and a crowd motivator of two continents. Thanks also to the kitchen inhabitants meeting at lunch time every day; loud lively discussion with you all was really enjoyable and enriching. I'd also like to thank the blood circulation system of ICIQ, Logistica guys Jesus and Marc for their rocky efficiency: you could bring good vibes along with parcels.

Leaning the head out the ICIQ (but not too much), I wish to thank all the people that shared these years with me. It was beautiful to find so many friends quickly self-assembling in a community of people with so much in common and so many countries of origin. It's difficult to express my greatest esteem and thank every element of a fast changing living organism, where everybody easy comes and easy goes. I will not forget

all the times we enjoyed Tarragona's and surrounding wonderful distractions, whether they be culinary, tasty, winey, musical, athletic, naturalistic, sandy or cinematographic. I would like to give special thanks to what can be referred to as the Reina Maria Cristina community centre. Phil, Gizem, Berta, Andrea, Ori, Asraa (aggain), Charles and Hanqing, thank you for what we shared during these years! Thanks to the marten, the cat and the fox (in random order) James, Chris, and Giovo: the underworld has lost its classy landlords since you left. Special thanks also to the Czech community, always in the first line, generous and professional in every field. Thanks with a big accent to the Italian community of the past and present, you always remind me that a piece of home is everywhere.

Thanks to all my flatmates of these years. Especially the most bearded metal one, Ximo(hamed) Soriano (and his extension Dolores) with whom I shared the highest top of my career as a rockstar. Thanks also to Paco Mitos for making that happen.

Ringrazio con grande affetto gli amici dei tempi che furono e gli amori perduti per ricordarsi ancora la mia faccia quando le strade si incrociano fuori da un display. Molti di voi avete fatto le mie stesse scelte e rimbalzate da un Paese all'altro in cerca della felicità. Se non lo avete ancora fatto, probabilmente tra poco lo farete. Insomma chi è rimasto a casa è quasi tanto expat quanto gli altri che se ne sono andati. Sarebbe bello un giorno invertire l'entropia. Nel frattempo, buona fortuna a tutti!

Un ringraziamento speciale a mio padre e mia madre per il loro incondizionato affetto e sostegno, che non smetto mai di sentire vicino. Un abbraccio forte a Roberta, Gianfranco, Francesco, Matteo e Maria Ada: siete una meraviglia!

Fundació ICIQ and Ministerio de Economía y Competitividad (MINECO) are greatly acknowledged for financial support, making this doctoral project possible.



TABLE OF CONTENTS

Chapter 1 Introduction	1
1.1 The energy and sustainability problem.....	2
1.1.1 The energy paradigm shift	2
1.1.2 Climate change and possible scenarios.....	3
1.1.3 The vector-energy cycle system.....	6
1.1.4 Closing the cycle: one promising solution.....	8
1.2 Artificial photosynthesis: heterogeneous photocatalytic CO ₂ reduction and water splitting	11
1.2.1 Catalysts and mechanism	11
1.2.2 Strategies to improve catalytic efficiency	17
1.2.3 The use of sacrificial agents.....	19
1.2.4 Landmarks and current status of heterogeneous artificial photosynthesis	21
1.2.5 Material/element recurrence.....	24
1.3 Motivation and subject of the thesis	25
Bibliography	28
Chapter 2 Methods	31
2.1 Photocatalytic reaction setup	32
2.1.1 Background.....	32
2.1.2 Reaction setup and method	35
2.1.3 Analytical system.....	37
2.1.4 Reactor	40
2.1.5 Light Source and filters.....	43

2.2 Infrared spectroscopy setup.....	46
2.2.1. DRIFT spectroscopy	46
2.2.2 Diffuse reflectance accessories and UV excitation setup.....	47
2.3 Photophysical characterization of materials.....	49
2.3.1 Importance of optical/photophysical properties	49
2.3.2 UV-Vis diffuse reflectance spectroscopy	50
2.3.3 Photoluminescence spectroscopy and decays	52
Bibliography.....	57
Chapter 3 TiO₂ and Pt/TiO₂ catalysts for CO₂ photoreduction _____	59
3.1 Introduction.....	60
3.2 Experimental section.....	61
3.2.1 Catalyst preparation	61
3.2.2 Gas-phase continuous flow photocatalytic reaction setup.....	61
3.2.3 Reaction procedure	62
3.2.4 <i>In situ</i> DRIFTS	63
3.3 Overview of catalytic activity	63
3.4 Gas phase H ₂ O-saturated CO ₂ photoreduction	65
3.4.1. Activity of fresh P25 and with Pt co-catalyst	65
3.4.2. Effect of oxidative and reductive pretreatments	69
3.4.3 Reactivation of photocatalytic activity under dark condition	70
3.4.4 Isotopic study of catalytic activity	76
3.5 <i>In situ</i> DRIFTS characterization.....	80
3.6 Conclusions.....	84
Bibliography.....	85

Chapter 4 Catalyst tuning with Zn and Rh-Cr for overall water splitting	87
4.1 Introduction	88
4.2 Experimental section	89
4.2.1 Catalyst preparation	89
4.2.2 Continuous flow photocatalytic reaction setup	90
4.2.3 Reaction procedure	91
4.3 Water splitting photocatalysts and modification series with Zn and Rh/Cr:	
slurry reactor	91
4.3.1 Gallium oxide based material: reactivity features	91
4.3.2 Gallium oxide modification series	93
4.3.3 Gallium oxide modification series: slurry activity	94
4.3.4 Tantalum and Titanium oxides modification series: slurry activity	96
4.3.5 Effect of excitation wavelength	100
4.3.6 Ga, Ta, Ti oxides series upon Zn doping and Rh/Cr deposition:	
discussion and mechanistic remarks	103
4.4 Water splitting photocatalysts and modification series with Zn and Rh/Cr:	
gas phase reactor	105
4.4.1 Ga ₂ O ₃ Zn-Rh/Cr and Ta ₂ O ₅ Zn-Rh/Cr: gas phase activity	105
4.4.2 Ga ₂ O ₃ Zn-Rh/Cr: K promotion	108
4.5 Zn and Rh/Cr modifications over tantalates	111
4.5.1 Tantalate class materials: synthesis and properties	111
4.5.2 Tantalate class materials reactivity for water splitting	116
4.6 Conclusions	118
Bibliography	121

Chapter 5 Photophysical characterization of photocatalytic materials _____	123
5.1 Introduction.....	124
5.2 Experimental section	124
5.2.1 UV-Vis diffuse reflectance measurements	124
5.2.2 Photoluminescence measurements	125
5.3 UV-Vis diffuse reflectance measurements: results	125
5.4 Photoluminescence measurements: results	129
5.4.1 Photoluminescence spectra	129
5.4.2 Photoluminescence decays	133
5.5 The Role of Zn and Rh-Cr promoters.....	135
5.6 Conclusions.....	137
Bibliography.....	139
Chapter 6 Summary and outlook _____	141
6.1 Summary	142
6.2 Outlook.....	146
6.2.1. Open challenges	146
6.2.2 GaN:ZnO Rh-Cr catalyst for visible light harvesting.....	148
6.2.3 PEC cell.....	149
6.2.4 Metal oxide nanoporous membranes	153
Bibliography.....	156
Shorthands and glossary _____	157
List of publication _____	159
Curriculum vitae _____	161

CHAPTER 1

INTRODUCTION

1.1 THE ENERGY AND SUSTAINABILITY PROBLEM

1.1.1 THE ENERGY PARADIGM SHIFT

The paradigm we are currently living in is the *fossil fuel economy*. In order to sustain human activities we are largely relying on fossil fuels as the source of energy and raw materials. Oil, coal and natural gas are the major source of energy used for transportation, electricity production and heating. At the same time, they are the major industrial resources for synthetic materials production. In particular oil, the blood of petrochemical industry, serves as most of the transportation fuel consumed daily by billions of people and as the pristine material of commodity materials such as plastic, required by modern industry.



Figure 1-1. Energy resources (left) and usage (right) in the fossil fuel economy paradigm according to the International Energy Agency (IEA) [1] and the U.S. Energy Information Administration (EIA) [2].

The fact that carbon resources derived from fossil fuels account for more than 80 % of the present total world primary energy supply raises great concerns dealing with sustainability. These concerns are complex and involve political, economic, and most importantly, environmental issues [3]. The key point, dealing with fossil resources, is that they are limited and non-renewable on the human timescale.

Intense and systematic exploitation of these natural resources by humans started in the XIX century. They acted as a tremendous driving force for the industrial revolution

and the figures of their usage grew almost monotonically ever since. Although the estimates may differ for some tens of years about the future availability, there is no doubt about the exhaustible nature of fossil fuels. Ranging from some decades for oil to over a century or more for coal, the overreaching of the peak of available extraction of fossil fuels (the notorious *Hubbert's peak*) is not just a possible scenario. It is rather a certainty in a relatively short, human life cycle timescale. The actual timescale of depletion of these natural resources will depend on many factors, especially technological advances. As an example, resources that a few years ago were considered non-economical, namely shale gas and oil, are currently subjected to enormous expansion. They could potentially lead countries like the U.S. to complete energetic independence in the next few decades, at least according to U.S.-friendly world-leaders oil producers such as BP and ExxonMobil [4, 5]. Ultimately economic factors will rule out when extraction technology cannot be any more capable of levelling off the price to a sustainable point. Concerns exist that, at that stage, the "thermodynamic price" of the overexploitation of those resources will be probably much higher. The depletion of valuable resources and environmental damage caused by excessive extraction and atmospheric pollution will be a debt which will be simply inherited by the future generations.

1.1.2 CLIMATE CHANGE AND POSSIBLE SCENARIOS

Among the fossil fuel related environmental concerns, the one drawing the highest attention of public and governments is the climate change.

Since the beginning of the industrial revolution, a quick unprecedented rise in the average temperature in the Earth troposphere (ca. 1 °C) was witnessed. In the last decades, a considerable amount of data and studies correlated the temperature rise to

anthropogenic atmospheric emissions [6]. In particular carbon dioxide deriving from hydrocarbons combustion, but also methane, nitrous oxide, hydrofluorocarbons (HCFs) and perfluorocarbons (PFCs) were pointed out as the main contributors to the so called *greenhouse effect*, responsible for the temperature change. These gases are collectively called *greenhouse gases* (GHGs), and their greenhouse potential is quantified in CO₂ equivalents.

At the end of the XX century a number of nations started to actively take actions, under the hood of the United Nations, in order to reduce the atmospheric emission of GHGs. This concerted endorsement culminated in *The Kyoto Protocol to the United Nations Framework Convention on Climate Change* agreement in 1997. Unfortunately, the insufficient global coordination in the actions promoted by the Protocol seemed to have weakened its goals and efficacy, already at the first check point in 2012. Although the process is still ongoing, the international coordination on climate issues is slowing behind the fast undergoing changes of the world. As a result, CO₂ atmospheric concentration is still constantly rising. From the 280 ppm level of the preindustrial era, we were breaking over 400 ppm level in 2013. The rise of the temperatures plays a role in the radical change of equilibrium that the Earth is experiencing, most notably leading to reduction of permanent ice reservoirs (in the Polar Regions and in the mountain glaciers), rise in sea levels, and causing exacerbation of climatic extreme phenomena (e.g. tropical storms and droughts).

During 2010's 16th Conference of the Parties (COP 16), the countries partaking in UNFCCC agreed that, in order to preserve the climatic equilibrium and containing the temperature increase within 2 °C, GHGs concentration must be maintained below the level of 450 ppm (CO₂ equivalents) [7]. This dramatic restriction will certainly require more determined efforts than what has been made to date.

The world economy, growing under the concept of *infinite growth* and the current paradigm of fossil fuel economy, is a very complex living organism which is very difficult to regulate. Rather, it appears to auto-regulate and slow down when reaching a breaking point of economical or energetic crisis, to speed up at even higher pace in post crisis phases (e.g. World Wars in 20th Century and oil crisis in the 1970s). Depending on the way the coming changes will be managed, different extreme scenarios could be imagined. According to Shell's 2008 outlook [8], two routes could be undertaken, defined *scramble* or *blueprint* scenario. In *scramble* scenario, society would react slowly to the change relying too much on fossil fuels for its needs, and ultimately causing abrupt and unprepared modification of the energetic system. The sudden change would cause high political instability and intermittent energy supply. In *blueprint* scenario, the world would start much earlier to plan a smoother change, investing in alternative forms of energy, starting from smaller local entities and industries seeking for higher energetic independence and stability. The governments would then sustain the change by pushing investments in alternative energies and disfavoursing fossil fuels by a carbon taxation policy.

Either way, in order to avoid the outburst of a dramatic energetic crisis and at the same time mitigating the climate changes, a modification of the current energetic paradigm must be faced in the near future. A shift from fossil fuel to alternative forms of energy will have to be planned in order to allow a sustainable change towards a "greener" economy. It is certainly complex to predict the way and the timescale these changes will be undertaken. However, expectedly more options and technologies will be available by the time of need, and better adaptation will be possible.

1.1.3 THE VECTOR-ENERGY CYCLE SYSTEM

The current picture of energetic flow is a one way stream. Most of the energetic and feedstock components are coming from fossil fuels and no regeneration of the resource is possible (Figure 1-1).

The new energy scheme we need to build should be cyclic. Multiple energetic resources, ideally of renewable nature, should together feed the cycle. The matter within the cycle should not follow the usage-disposal flow but rather work as vector of the real value they deliver. This value is associated with the energy these molecules or materials store in form of chemical bonds, and the task they were engineered to accomplish (e.g. fuel, drugs, food, etc.). After their function is performed, the exhausted materials or by-products should be reprocessed in the cycle. Suitable energy demanding processes should be designed to reload their energy content (or Gibbs free energy G), thus renewing the cycle.

Our economy relies, for its energy demand, on compounds of carbon, hydrogen and oxygen. Their most stable chemical states on the Earth biosphere are water and carbon dioxide, which also are the ultimate products of hydrocarbons combustion. It would be therefore ideal to find a sustainable process allowing us to convert CO_2 and H_2O to highly energetic compounds, closing the energy cycle. The most simple and ideal chemical energy vectors would be light hydrocarbons and oxygenated compounds such as methane, methanol, ethanol, and dimethyl ether (DME). These are well-known and versatile compounds which would find a variety of applications in the bulk chemistry and fuel sector. This is the fundamental principle of the emerging *methanol economy* scheme [3, 9-11], summarized in Figure 1-2.

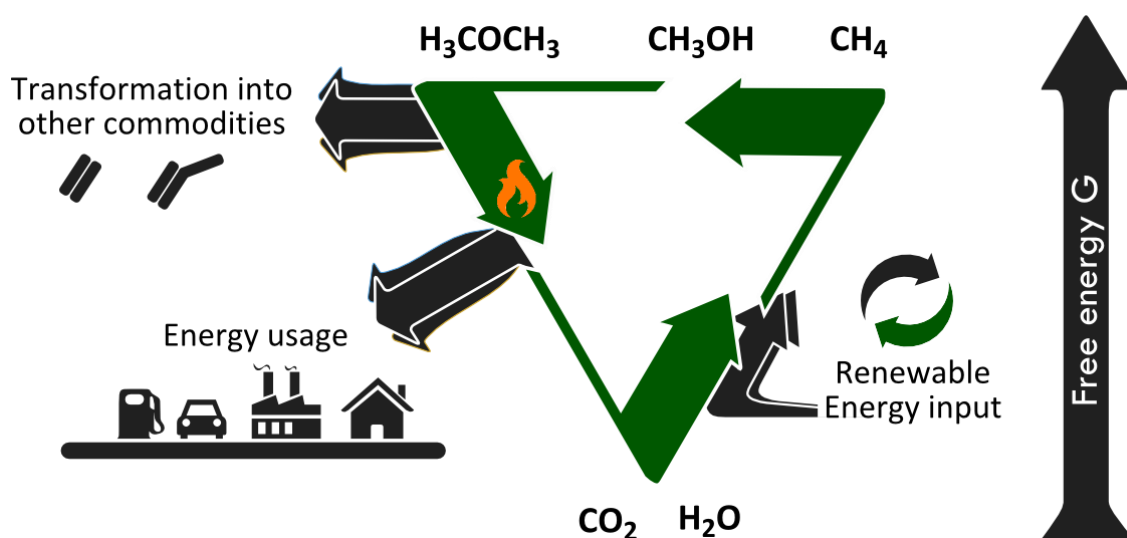


Figure 1-2. Methanol economy scheme.

Alternatively or complementarily, hydrogen has been postulated as the energy vector of the future, in the analogous *hydrogen economy*. In this scheme carbon is not present as an energy carrier. Hydrogen combustion, producing only water as by-product, would be the key reaction thought to satisfy our energy demand. Water would be then again used as a feedstock for renewable production of hydrogen (where oxygen would be the only by-product). Even though hydrogen is a chemical of central importance in the established chemical industry, greater efforts would be required to bring it outside the bulk chemical industries as a common fuel. The more complex issues of safety, transportation and lower energy density allowed by hydrogen, in comparison to most carbon based fuels, might be a real bottleneck for the implementation of such an energy vector. Carbon based fuels like methanol and DME could much more readily substitute the current liquid fuels without the need of radical modification of engines and fuel reservoir design. Moreover, a distribution infrastructure very similar to the currently in use could be employed. These points make the methanol economy scheme a more attractive scenario to pursue in the near future.

Independently of the vector of choice, the key point for the sustainability of the system is to find a suitable regeneration process in the cycle. Clearly any fossil energy resource must be discarded in the long term. Despite the serious safety and environmental concerns periodically raised by nuclear power plants, fission based technologies are getting safer and more efficient, and they might be playing a key role in the future. Nevertheless it is worth noting that the drawbacks of these technologies often come from the post-production period. The cost of nuclear waste disposal and safe shutdown of old power plants always exceeds the actual estimates. In many cases they become a burden recklessly given to the next generations. Nuclear fusion technologies promise to be cleaner and highly efficient, but at the present time the technological gap to overcome makes it difficult estimate the timescale of their possible exploitation.

Therefore, it is of absolute priority to radically improve the usage of renewable energy resources: wind, hydroelectric potential, tides, geothermal heat, biofuels and most importantly the solar radiation. The Sun, on which all renewable resources depend (excluding tides and geothermal energy), irradiates on the Earth's surface with an average power of 1 kW at the standard value AM 1.5 [12]. Looking at a bigger picture, the Sun irradiates the Earth with an amount of energy about 3.5 orders of magnitude higher than the present human power demand (19 TW in 2013) [13, 14]. Much more effort in capturing this energy must be clearly endeavoured, since its usage alone could satisfy all our energy demands in the cleanest possible way.

1.1.4 CLOSING THE CYCLE: ONE PROMISING SOLUTION

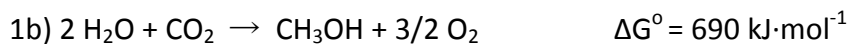
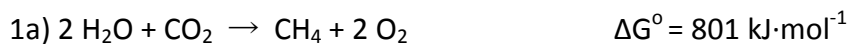
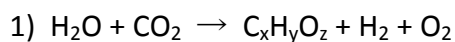
One of the most attractive strategies to tackle the energetic problem and the climatic problem at once would be finding an artificial process to close the carbon cycle (like suggested in the methanol economy scheme), making use of the most

abundant renewable energy available: sunlight. In nature, this job is performed by plants and has the name of photosynthesis, generating glucose from carbon dioxide and water. This process is the basis of life as we know it, bridging simple inorganic molecules to the complexity of molecular processes and structures of living organisms. Also, it is the basis of our fossil fuel economy, as most of our present energy resources are the results of millions of years of past photosynthetic activity.

The process we seek to design is therefore a form of *artificial photosynthesis*. By this term we strictly mean any chemical process that allows us to produce reduced forms of carbon compounds out of carbon dioxide and water, using sunlight as energy source.

The beauty of this strategy lies in a double advantage. On the one hand we would be able to produce fuel or other chemicals out of sunlight and of abundant starting materials (CO_2 and H_2O). Unnecessary use of natural resources would be avoided and they could be preserved for wiser non-combustive use. On the other hand, CO_2 could be trapped and transformed. Its atmospheric concentration could be equilibrated, minimizing its impact on climate change.

It is important to mention that a less strict definition of the term *artificial photosynthesis* is also widely employed in literature to describe *photocatalytic water splitting*. This process is the photo-driven scission of water molecule into its constituent elements, hydrogen and oxygen. This process is intimately related to photocatalytic CO_2 reduction. CO_2 photocatalytic reduction in presence of water always competes with water splitting, producing gaseous hydrogen from the reduction of protons to elemental hydrogen.



Scheme 1-1. Artificial photosynthesis reactions. 1) General scheme of carbon dioxide reduction with water (not balanced); examples of CO₂ reduction to 1a) methane and 1b) methanol [15]. 2) Water splitting reaction [16].

In order to perform these reactions at sufficiently high rates and with high quantum yields (exploiting the most of the incident sunlight power), different strategies have been attempted. Both homogeneous and heterogeneous catalytic approaches are under investigation. For the sake of the future industrial implementation of these technologies, it is more advisable to pursue the gas phase heterogeneous catalytic route, which generally allows easier product separation and continuous flow operation. This would be the most advisable solution, as it would be the most suitable process to obtain cleanest products in a continuous fashion. On the contrary, liquid phase reactors would suffer from the important issue of product separation from water.

This reaction is also widely investigated with an electrocatalytic approach, where an electrical potential is applied to a cathode and an anode to drive the reaction at the surface of materials acting as electrodes. These two approaches can be synergistically applied together in the same system by means of a proper photoelectrochemical cell (PEC). Possibly, a careful optimization of photo and the electro-contributions to the catalytic process might be the key to accomplish the artificial photosynthesis at significant rates.

In the following section an overview of the process of artificial photosynthesis and a selected historical perspective on the heterogeneous approach will be presented.

1.2 ARTIFICIAL PHOTOSYNTHESIS: HETEROGENEOUS

PHOTOCATALYTIC CO₂ REDUCTION AND WATER SPLITTING

1.2.1 CATALYSTS AND MECHANISM

As summarized in the previous section, artificial photosynthesis is a process that converts electromagnetic radiation (sunlight) and stores it as chemical energy in the form of chemical bonds (e.g. C-H and H-H). This conversion is mediated by a photocatalyst that harvests light and transduces it into a chemically reactive high energetic state that drives the transformation of the adsorbed reagents. The way a photocatalyst converts electromagnetic energy into chemical energy involves a photon driven charge separation in a material. A photocatalyst must be capable of absorbing light in the widest possible range of wavelength and use that energy to generate a charge separation state. This state has to be sufficiently long-lived to consequently generate reactive charged states on the surface [17]. Due to the required electronic properties, the solid materials to perform this task are semiconducting materials, typically metal oxides [18-21]. These materials are characterized by electronic band structure in which a lower energy *valence band* (VB) is nearly completely filled with electrons and a *conduction band* (CB) is substantially empty. The energy difference between these two bands is called *bandgap* (E_g). By absorption of a photon with energy higher than the bandgap, an electron can be promoted from the VB to the CB, generating an electrostatically bound charge separation state called *exciton* (hole-electron pair). This state can then be separated into its two components, the hole and

the electron. Subsequently, independent migration of the charges towards different confined states can occur. Eventually they can reach specific chemical sites on the surface and become active for redox reaction. It is worth nothing that each of these steps is affected by a strong probability of hole-electron recombination, associated to emission of light or non-radiative dissipation phenomena [22-24]. Only a small fraction of the photo-generated electron and holes effectively reaches the chemically active sites on the surface and drives the reaction, constituting a real bottleneck for the boost of the quantum yield [21].

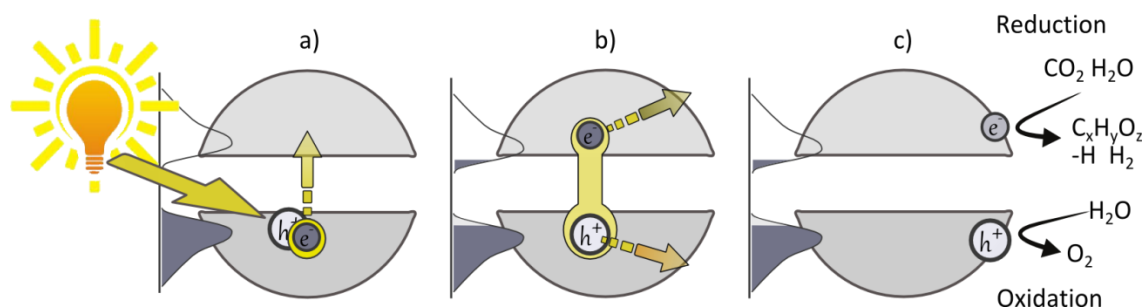


Figure 1-3. Artificial photosynthesis reaction scheme in a semiconducting material: a) light excitation; b) exciton formation/separation and charge migration to the surface; c) charge confinement on the surface and redox reactions. On the left side of each section a picture shows the population of VB (bottom half) and CB (upper half)

When the excited electron and hole are effectively transferred to a reactive surface state, they can react with CO₂ and H₂O adsorbed on the surface to give products or their intermediates. At the reduction sites, both CO₂ and H₂O could accept electrons with generation of different reduced carbon oxygenated compounds or H₂. To close the reaction pathway, at the oxidation site H₂O has to be oxidized to O₂ or to other oxygen compounds with intermediate oxidation number (e.g. peroxides, radicals). The

latter process is surely the most complex and the one offering the most of the challenges.

From an electrochemical perspective, the bandgap and the band's edge energy location are believed to play a critical role in the mechanism [25, 26]. For the effective charge transfer to the reagents, the electron and the hole must be promoted to energy bands respectively at potentials more negative (for the reduction half reaction) and more positive (for the oxidation half reaction) than the reduction or oxidation potential of the reaction they have to perform. Altogether the bandgap energy must be higher than the energy required for the full redox process. Taking water splitting as an example, the thermodynamic requirement is fulfilled when $E_g > 1.23$ eV. At the same time, the band edges must lie at a correct potential so that $E_{CB} < -0.41$ V and $E_{VB} > 0.82$ V at neutral pH [27].

Many semiconductors feature correct band potentials to perform the reduction process of water or CO₂ but they do not satisfy the requirement for water oxidation, closing the way to the overall artificial photosynthetic process [16].

On the other hand, the bandgap absolute value is also a very important characteristic of materials, setting limits for light absorption. The energy of the incident photon must be larger than the bandgap to be absorbed by a material. The larger the bandgap, the shorter the edge wavelength of adsorption, as follows from the following relation

$$\text{Equation 1-1. } \lambda_{\text{onset}} = 1240 / E_g,$$

where wavelength λ is expressed in nm and E_g in eV. This value is particularly important because it defines the range of the solar spectrum that can be harvested by the material.

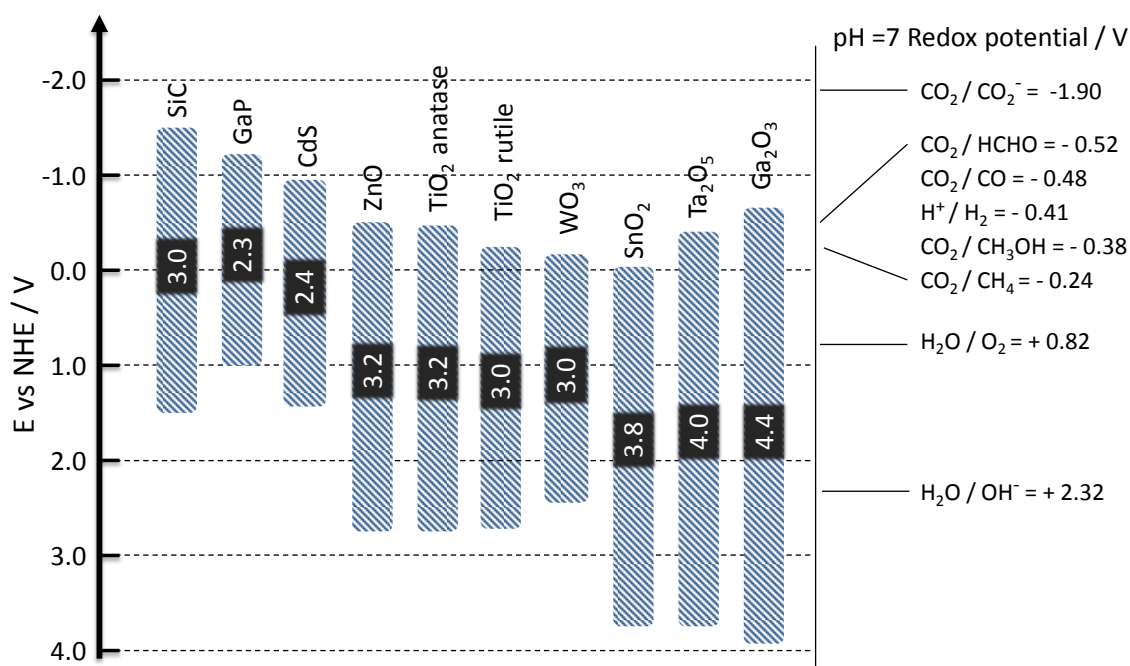


Figure 1-4. E_g extension (in blue; value/eV in the black squares) and band edge potentials (vs NHE) of different materials in comparison with the half reaction potential of relevant artificial photosynthesis phenomena [25, 26, 28].

The portion of the solar spectrum incident on the Earth's surface (Figure 1-5), and therefore usable for photocatalysis, has its intensity peak in the visible range (about $380-400 < \lambda_{\text{vis}} < 780-800$ nm). About only 4 % of incident radiation sits in the ultraviolet (UV) region ($\lambda_{\text{UV}} < 380-400$ nm). Most of the energy is actually delivered as near infrared (NIR) radiation ($\lambda_{\text{NIR}} > 780-800$ nm). As an important set point, even though the distinction only has meaning in terms of human vision perspective, absorption of visible light by a semiconductor photocatalyst can only occur when $E_g < 3.1 - 3.2$ eV (according to Equation 1.1). The majority of the available photocatalysts, including the ubiquitous titania, can only harvest and use UV light; therefore, great efforts have been invested to extend the adsorption range of these materials. This is because the UV range only contributes to a minimal fraction to the energy irradiated on the Earth's surface. Even though the band excitation mechanism makes the most accepted and

consistent scheme in heterogeneous photocatalysis, other mechanisms have been proposed to work on a more localized level.

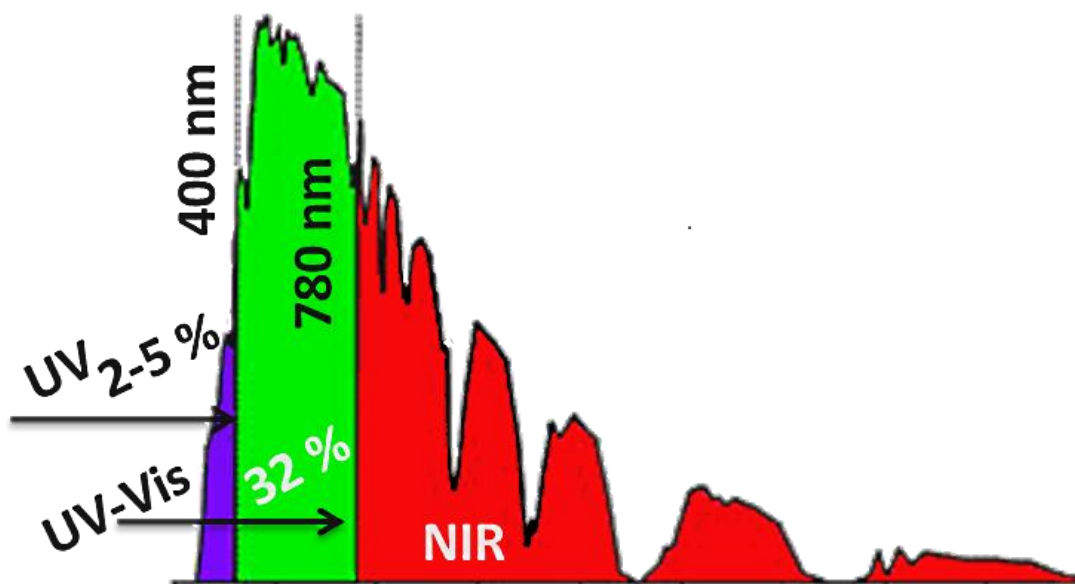


Figure 1-5. Solar spectrum at the Earth's surface and the relative energy contribution

Anpo and co-workers have worked with titanium oxide based catalysts and observed that not only bulk titania is active but also its smallest unit, in form of TiO_4^{n-} tetrahedral units, is an efficient photocatalyst [29-31]. Corroborating their theory with photoluminescence and XAS evidences, they demonstrated how TiO_4^{n-} units grafted over a mesoporous material could function in a very similar fashion as TiO_2 . The absorption of a photon of a suitable energy ($\lambda < 300 \text{ nm}$) would promote an electron charge transfer from the oxygen to the titanium centre with generation of a reactive molecular excited state in the form of a $(\text{Ti}^{3+} - \text{O}^-)^*$. Due to quantum effects, the photon energy required to generate this excited state in a nanoscale clusters is higher than the energy required to generate an exciton in a band structure of the extended semiconductor. Translating further the concept to the molecular scale, the energy

required is the highest in case of isolated TiO_4^{n-} tetrahedrons, where quantized molecular states describe the energy levels more accurately (Figure 1-6).

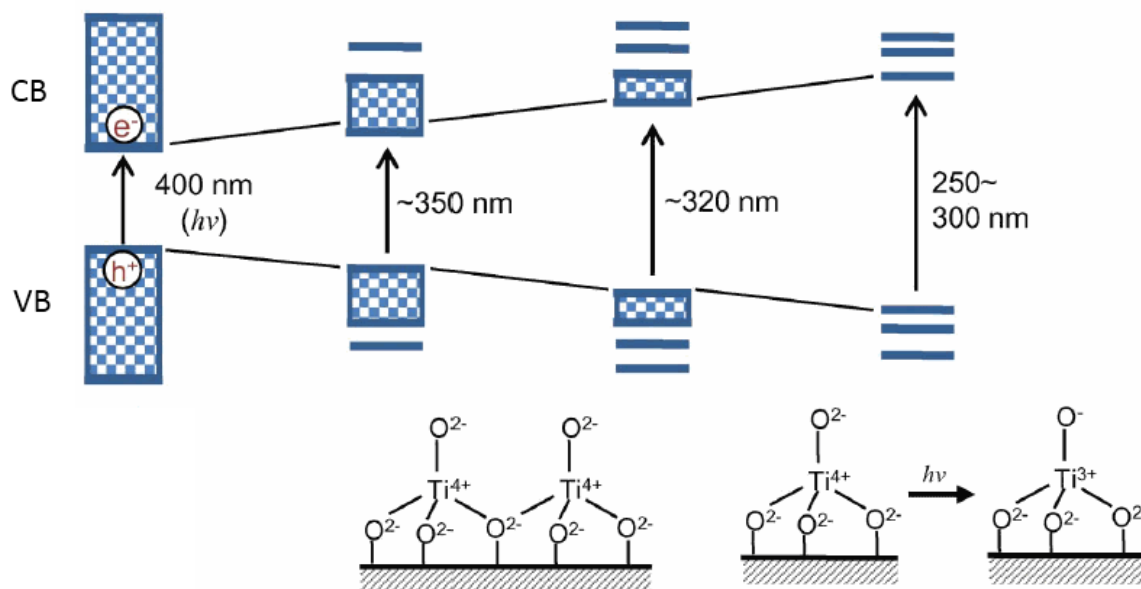


Figure 1-6. Photon excitation energy requirements for bulk and nano-scale titanium oxide based materials (adapted from ref. [32] with permission from The Royal Society of Chemistry).

Bulk semiconductor materials are certainly more efficient in light harvesting compared to their nano-sized counterparts due to the lower photon energy requirements and wider absorption spectrum. Nevertheless, it is important to point out that more localized molecular structure and surface defects could play an important role in photocatalysis.

Correct band positioning alone may not be a sufficient condition to ensure formation of redox active surface species and adsorption sites for the reagents. A pure electrochemical approach is thus insufficient to design an efficient photocatalyst.

1.2.2 STRATEGIES TO IMPROVE CATALYTIC EFFICIENCY

Due to energetic requirements and position of electronic bands, at present time the most successful photocatalysts for heterogeneous artificial photosynthesis are relatively wide bandgap metal oxides. Titania is the most studied example and by far the most used material. Different strategies have been attempted in order to improve the still very poor yields of artificial photosynthesis.

One important route is the widening of the absorption spectrum of active materials. Typically, if photoactivity is present in the UV range for a wide bandgap material ($E_g > 3.2$ eV) it is possible to increase its light sensitivity by doping it with non-metal elements such as B, N, C, P and S [20, 33]. The substitution of a fraction of the oxygen atoms with such elements can produce artificial electronic states within the bandgap, enabling lower energy transition and resulting in a wider light spectrum harvesting. This can be visibly confirmed by a colour change from white to different coloured shades when the bandgap is reduced. For instance, titania powder is perfectly white in its undoped form but becomes yellow or greenish upon doping with N or C atoms. At higher doping levels it shows deep hues of the same colours. Also, very defective electron rich forms of titania (known as Magneli phases) can assume deep blue or black hues. In these phases, the bandgap energy can be reduced to such a low level that titania displays electrical conducting properties [34]. Nonetheless, the extension of the absorption range may have a positive effect in light harvesting features, but it does not always imply that such a material is a more efficient catalyst. This property mostly depends on how efficiently the electrons and the holes are produced and separately driven towards chemically reactive sites, slowing down and avoiding the recombination process.

In the attempt to enhance photocatalytic activity by optimisation of charge separation, the most explored strategy is metal doping, used as *co-catalyst*. By supporting a co-catalyst (typically noble metal nanoparticles or oxides with a proper band potential) we can create potential sinks attracting and trapping electron or holes at the surface of the material (Figure 1-7a).

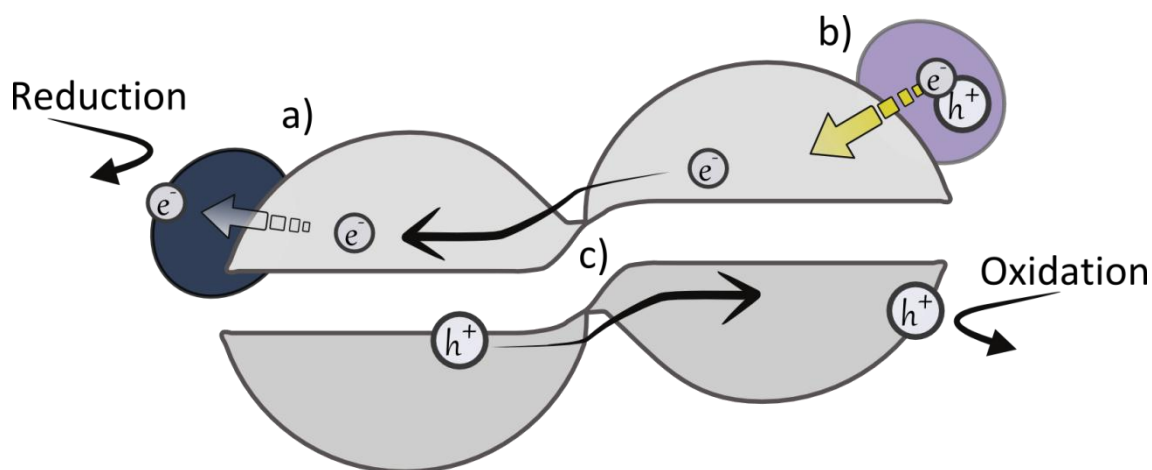


Figure 1-7. Strategies to improve photocatalysis: a) co-catalyst as charge trap (i.e. Pt); b) photosensitization (i.e. Au); c) coupling semiconductors to drive separation of photo-generated charges.

At a metal-semiconductor interphase a Schottky barrier is formed. Due to the generated band potential bending, it allows the metal to accept photoexcited electrons and trap them, protecting them from recombination with the holes [21, 35-37]. Platinum particles are excellent reduction sites and hydrogen evolution sites when coupled with a suitable photocatalyst.

In an analogous way, coupled photoexcited semiconductors can hop electrons or holes and exchange charges according to their relative band potentials (Figure 1-7c). These free charges are physically separated in different domains of the material, thus longer-living, and have more chances to independently undergo redox reactions with the substrates.

In other cases a material or molecule can be coupled to a photocatalyst enhancing its light harvesting features and acting as a *photosensitizer* (Figure 1-7b). Gold nanoparticles [38], quantum dots [39] or molecular antenna system in form of metal complexes [40] or dyes [41] are good examples. They are capable of absorbing light in a wide wavelength range into the visible producing excited electrons. These are then transferred to the conduction band of the coupled semiconductor producing an indirect excitation of the catalyst.

1.2.3 THE USE OF SACRIFICIAL AGENTS

For the majority of the photocatalysts, the reduction half reaction is more readily accomplished as compared to the oxidation counterpart. Water oxidation reaction (or oxygen evolution reaction, OER) is particularly challenging. Oxygen is thermodynamically and kinetically very stable in the oxide state. Removing electrons from the shell yields highly oxidising radicals as intermediates, which could readily react with products of the photoreduction pathway, “short-circuiting” the process. Nonetheless, both half photoreactions involve complex steps and they are far from being optimized and well understood.

A widely used approach that allows the independent study of the two half reactions is the use of *sacrificial agents* [37]. This strategy employs a reacting compound soluble in the liquid suspension and acting as a stoichiometric charge scavenger. When one focuses on CO₂ photoreduction as the target reaction and H₂O oxidation is sluggish or not occurring, the process is not catalytic and the reduction is not sustainable. In this case, a sacrificial positive hole scavenger can be added. This compound is readily oxidized by the holes accumulating on the catalyst, opening a steady photoreduction pathway. In an analogous way, water oxidation can be enhanced by adding a sacrificial electron scavenger (Figure 1-8).

Typical hole scavengers are oxidisable organic compounds such as methanol and ethanol or inorganic ions like OH^- , HCO_3^- and SO_3^{2-} . The more common electron scavengers are easily reducible metal cation or molecular ion such as Ag^+ , Ce^{4+} and I_3^- .

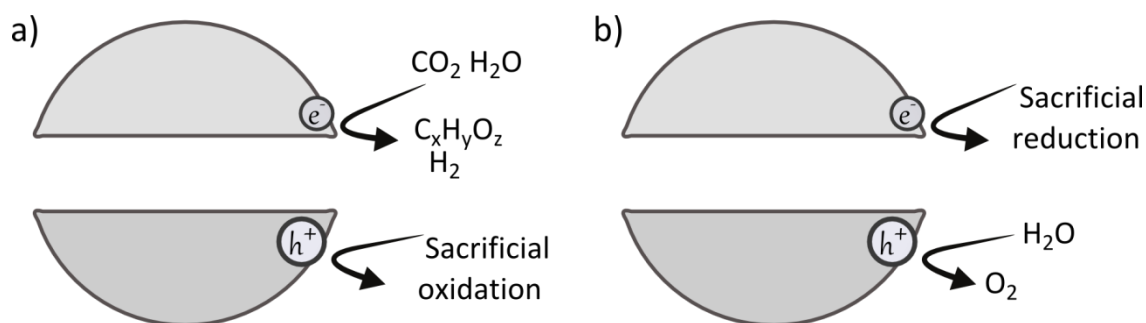


Figure 1-8. Schematic concept of sacrificial agent driven half photoreactions: a) photoreduction; b) water oxidation.

In principle, one could use any organic compound as a hole scavenger to drive photoreductions. This approach is of high interest when considering the possibility to couple water depuration by means of photocatalytic mineralization of contaminants with artificial photosynthesis. Such kind of process could have the double benefit to purify waste water from compounds like urea and other organic contaminants [42, 43], producing at the same time energy in form of hydrogen from photocatalytic water splitting.

However, on a practical perspective, it is important to point out that driving CO_2 photoreduction or water splitting with sacrificial organic compounds like methanol or ethanol is highly undesirable and counterintuitive. Light hydrocarbons and alcohols are the desired product of the reaction and highly valuable compounds. Thus we would not seek to sacrifice them to produce methane or hydrogen. Also, the introduction of sacrificial agent might add unnecessary variables in an already complex system. Their

use as investigation tool could then be source of controversies and artefacts rather than a simplification.

For the described reasons, the use of sacrificial agents has been debated in photocatalysis and their use was avoided throughout this thesis project.

1.2.4 LANDMARKS AND CURRENT STATUS OF HETEROGENEOUS ARTIFICIAL PHOTOSYNTHESIS

The first steady steps of artificial photosynthesis research were moved in the 1970s. The pioneering work by Honda and Fujishima demonstrated for the first time that water splitting and CO₂ reduction can be achieved in a photoelectrochemical cell [44-46]. Hydrogen and light organic compounds (e.g. methanol and formaldehyde) could be produced from water and CO₂ at a titania based cathode surface, irradiated with UV light and subjected to electrical bias.

At the same time, the mechanistic basis for artificial photosynthesis using powder suspension was set by Bard [18, 47]. He set the foundation on which the research on the following decades would build up. Platinum and other co-catalysts were then found to be capable of drastically improving the photocatalytic activity.

It is important to mention that the typical photocatalytic activity reached with this systems (and very common still today) is rarely higher than a few tens $\mu\text{mol}\cdot\text{g}_{\text{cat}}^{-1}\cdot\text{h}^{-1}$ for hydrocarbon reduction products, more commonly below ten, especially in absence of sacrificial agents. As a matter of fact practical applications of such technology still appear to be a long term goal in the 2010s.

In the 1980s the researchers focused on powdered catalysts, mostly titanium based (titania, titanates). Pure water splitting showed higher potential. Remarkable contributions to photocatalytic water splitting were brought by, among others, Wagner [48] and Domen [13, 49, 50] who explored water splitting on SrTiO₃ based

materials in liquid suspension and in gas phase. NiO co-catalyst emerged as a hydrogen evolving site. Overall water splitting started to be a more realistic goal and H₂ productivity started to climb up towards mmol·g_{cat}⁻¹·h⁻¹ level.

In the 1990s, Anpo and co-workers gave great insights in the CO₂ photoreduction process investigating isolated TiO₄ units grafted on mesoporous zeolite-like materials. Functionalising Ti on nanostructured materials such as MCM-41, MCM-48, and SBA-15, yields of CH₄ and CH₃OH could be enhanced in the gas phase under UV irradiation as compared to bulk Ti oxide materials [29-31]. As mentioned in the previous section, they demonstrated that the underlying mechanisms different from semiconductor excitation could play a central role in this catalytic process.

At the turn of the new millennium, artificial photosynthesis field attracted increasing attention as the legitimate worries for depletion of natural resources and climate changes appear more and more evident. The number of materials that proved to be active catalysts or co-catalysts (with or without sacrificial agents) is increasing daily, and the majority of them are still designed following Bard's concept (semiconductor powder based) rather than Anpo's (isolated semi-molecular unit concept).

During the last decade, great attention has been also given to the class of materials of tantalates, niobates and titanates. In particular tantalates became a hot topic thanks to the work of Kudo and Kato who demonstrated a very high overall water splitting activity (several mmol·g⁻¹·h⁻¹ H₂ and O₂ production) in liquid suspension for NiO/NaTaO₄ nanocubes [51-53].

Nevertheless, titanium oxide based materials continue to be an unlimited source of discovery, also due to their unmatched morphological variability and fine nanoscale tunability [54, 55]. For instance, electrochemically synthesized TiO₂ nanotubular

structures were reported by the group of Varghese to be efficient catalyst for CO₂ reduction to a wide range of hydrocarbons under solar irradiation [56]. The implementation of such nanotubes in a flow-through membrane form would be a highly interesting goal, as it could be a tool for separating oxidation and reduction sites and their products.

Notably, again Domen, Maeda and co-workers enriched the set of materials active for water splitting under visible excitation, culminating with the discovery of GaN:ZnO mixed phase catalyst and Rh-Cr co-catalyst [57].

Moreover, starting from the late 2000s, also the class of gallium oxide materials was found to be extremely active in water splitting. Modified with a wide range of dopants and co-catalysts (most interestingly Zn as the former, and Rh-Cr as the latter), these wide bandgap materials show very high H₂ production under UV light, reaching almost 10 ml·g_{cat}⁻¹·h⁻¹ productivity [58-60]. A few reports are also available, suggesting Ga₂O₃ materials can be actively drive CO₂ photoreduction to CO or CH₄ along with water splitting [61, 62]. The potential development of Ga₂O₃ materials is surely one of the most promising paths nowadays.

Recently, very important steps forward in the design one-component water splitting device with separate evolution of oxygen and hydrogen were achieved by Nocera and co-workers [63]. They demonstrated for the first time the possibility to design an *artificial leaf*, capable of splitting water at a high rate and generating stoichiometric H₂ and O₂ in its two opposite faces. Thanks to the efficient charge separation in the photovoltaic inner layer working as light harvester, the oxidation catalyst (cobalt oxide based) and the reduction catalyst (NiMoZn) were efficiently and independently activated in liquid water.

This last example clearly suggests that much has to be done not only on the catalyst point of view. New smart device and reactor designs are to be carefully considered in

order to tackle the challenges of efficient light harvesting, surface reactivity and, last but not least, product separation. The last point certainly represents a problem for the presence of oxygen in the product mixtures, possibly limiting the reactivity due to reverse reaction and clearly creating explosive mixtures unsafe to store as synthesized. Future research would certainly have to focus more on these issues, growing along with the relevant reactivity improvements brought about during the last decade.

1.2.5 MATERIAL/ELEMENT RECURRENCE

More strictly focusing on the CO₂ photoreduction rather than water splitting, an attempt to graphically display the relative diffusion of the wide set of materials/elements currently known and reported is shown in Figure 1-9.

Indeed, a hegemonic presence of titania as catalyst is clearly visible from the plot. Among TiO₂ materials, Degussa P25 and anatase phases are certainly the most reported in literature. Cu, Pt, Ru and Ag are on the other hand the most common metals used as co-catalysts. Ga oxide materials could not be included in this diagram, reflecting the fact that their application for CO₂ conversion technology is still very little explored and reported in literature reviews.

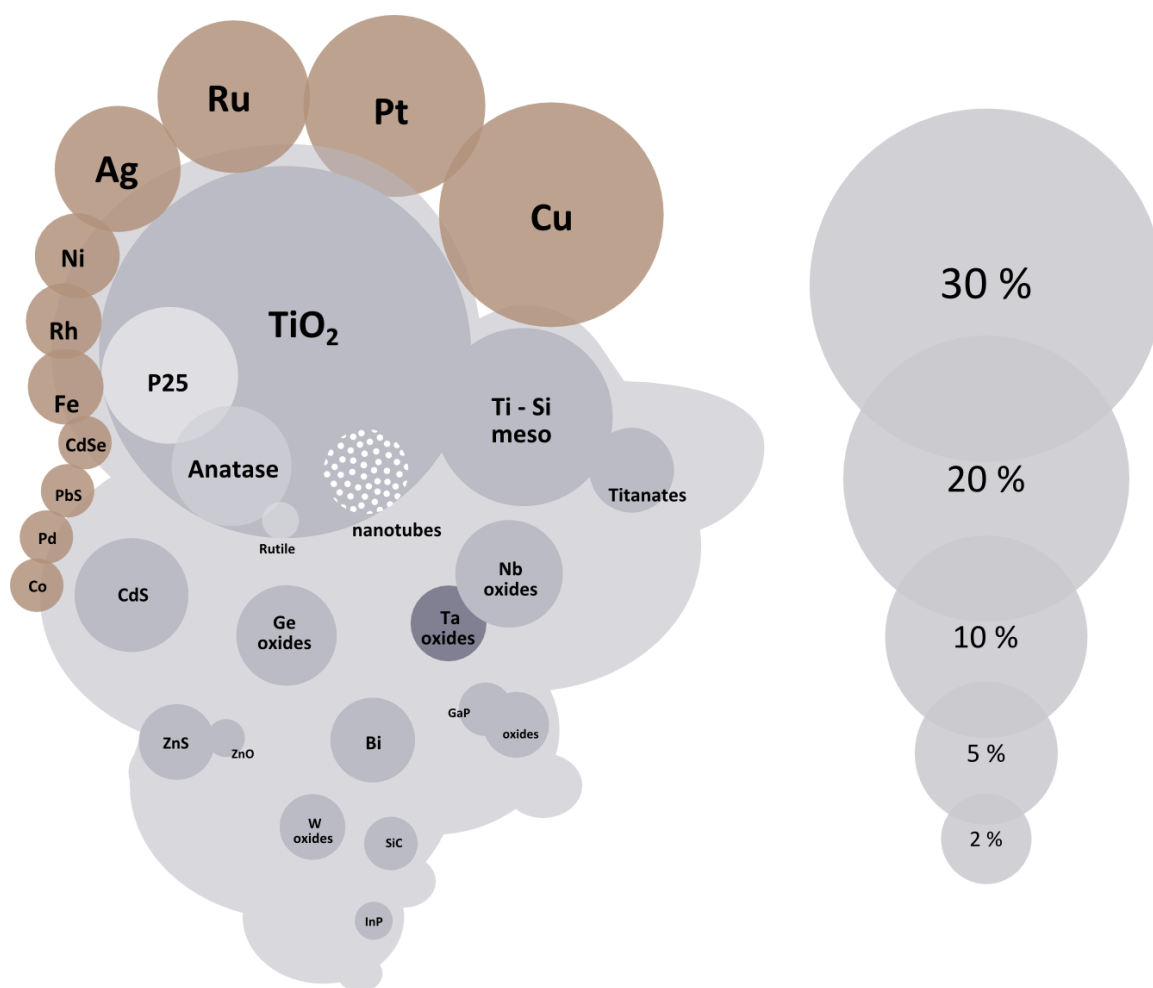


Figure 1-9. Percent distribution of catalysts (grey) and co-catalysts (brown), based on the frequency of recurrence of tabulated entries in recent reviews on CO₂ photocatalytic conversion [26, 36, 64, 65].

1.3 MOTIVATION AND SUBJECT OF THE THESIS

Even though great research effort has been spent in past decades in the field of CO₂ photoreduction, this technology has still to overcome many issues hindering its applicability. Firstly and most importantly, the yields are at the present time still too low. This does not only render the process obviously uneconomic but also challenging to study. The products, hydrogen and light organic compounds, are typically measured at ppm level of concentration, pushing the analytical equipment close to the detection limit. In such conditions impurities and related artefacts can be detrimental for proper

investigation of the reaction. Also, an abuse of sacrificial agents to push forward incomplete or low yield reactions could give a biased picture of the catalyst pool at our disposal. Radically different testing condition and application of sacrificial agents make it very challenging to compare the catalysts described in literature and correctly judge their efficiency. Another important issue, that pairs with the low yields, is the low reproducibility of catalytic testing and the stability of the catalysts. The catalysts quite often suffer from fast deactivation, meaning that the outcome of a catalytic testing might drastically depend on pre-treatments, lamp power and emission spectrum and several other experimental parameters.

The question might rise whether the widespread implementation of the batch reactor approach might not be the ideal system for studying this process, even though it allows the accumulation of products and their concentration over a long period of reaction testing. Typically, the reaction is conducted by irradiating a CO₂ saturated water suspension kept in a closed reactor for several hours. A few headspace samples per hour are collected, and the products are analysed by means of gas chromatography. This approach has the clear disadvantage of poor time resolution and to give poor information on the process under dynamic condition (e.g. temperature changes and switching off and on of the irradiation). Moreover the batch approach makes it difficult to notice and evaluate possible deactivation of the catalyst and the presence of a steady state production.

Despite clear advantages of continuous flow operation over batch operation (in terms of future applicability, product separation and scale-up), an extremely limited number of studies have been reported to date for continuous operation of artificial photosynthesis. For this reason, we chose to study CO₂ photocatalytic reduction with a continuous flow reactor approach using slurry and gas phase reactors. In order to enhance the product analysis time resolution, we monitored product concentrations

by means of mass spectrometry. This analytical method allowed the simultaneous detection and quantification of products on the second timescale and improved the access to detailed dynamic information on the process. This approach is promising to facilitate gaining mechanistic insights and the nature of the active sites.

The same reaction conditions could be also tested while probing the catalyst by means of *in situ* diffuse reflectance infrared Fourier transform spectroscopy (DRIFTS). This technique allowed us to study the surface species active in the process under the conditions completely matching with those operational during the catalytic testing.

In order to avoid interferences, and thanks to the very low detection limit allowed by mass spectroscopy and by DRIFTS, all the tests were performed in absence of sacrificial agents.

The mechanism of photocatalytic reactions is intimately bound to the photophysical properties of the used materials. In particular their light absorption and emission properties follow similar mechanistic pathways. For this reason, techniques like diffuse reflectance spectroscopy, photoluminescence spectroscopy, and time-resolved photoluminescence techniques were used to characterise the catalytic materials. The evidence collected by comparing different material's properties, finally allowed to propose a mechanism explaining each catalyst's activity in relation to different structural modifications.

BIBLIOGRAPHY

1. U.S. International Energy Agency, *Key World Energy Statistics 2013*, **2013**.
2. Energy Information Administration, *International Energy Outlook 2013*, **2013**.
3. G. A. Olah, A. Goeppert, G. K. S. Prakash, *Beyond Oil and Gas: The Methanol Economy*, Wiley, **2009**.
4. British Petroleum, *BP Energy Outlook 2030*, **2013**.
5. ExxonMobil, *The Outlook for Energy: A View to 2040*, **2013**.
6. Intergovernmental Panel On Climate Change, *IPCC Fifth Assessment report. Climate Change 2013: The Physical Science Basis*, **2013**.
7. K. Levin, R. Bradley, *Comparability of Annex I Emission Reduction Pledges*, **2010**.
8. Shell, *Shell energy scenarios to 2050*, **2008**.
9. G. A. Olah, *Angewandte Chemie International Edition* **44**, 2636, **2005**.
10. G. A. Olah, A. Goeppert, G. K. S. Prakash, *The Journal of Organic Chemistry* **74**, 487, **2008**.
11. G. A. Olah, G. K. S. Prakash, A. Goeppert, *Journal of the American Chemical Society* **133**, 12881, **2011**.
12. American Society for Testing and Materials, *ASTM G173* **2012**.
13. Energy Information Administration, *International Energy Outlook 2013*, **2013**.
14. V. Smil, *General energetics*, **1991**.
15. Ş. Neaţu, J. Maciá-Agulló, H. Garcia, *International Journal of Molecular Sciences* **15**, 5246, **2014**.
16. R. Abe, *Journal of Photochemistry and Photobiology C: Photochemistry Reviews* **11**, 179, **2010**.
17. M. R. Hoffmann, S. T. Martin, W. Choi, D. W. Bahnemann, *Chemical Reviews* **95**, 69, **1995**.
18. A. J. Bard, *Journal of Photochemistry* **10**, 59, **1979**.
19. A. J. Nozik, R. Memming, *The Journal of Physical Chemistry* **100**, 13061, **1996**.
20. M. X. Tan, P. E. Laibinis, S. T. Nguyen, J. M. Kesselman, C. E. Stanton, N. S. Lewis, *Energy Conversion* **41**, **1994**.
21. A. L. Linsebigler, G. Lu, J. T. Yates, *Chemical Reviews* **95**, 735, **1995**.
22. J. Liqiang, Q. Yichun, W. Baiqi, L. Shudan, J. Baojiang, Y. Libin, F. Wei, F. Honggang, S. Jiazhong, *Solar Energy Materials and Solar Cells* **90**, 1773, **2006**.

23. X. Wang, Z. Feng, J. Shi, G. Jia, S. Shen, J. Zhou, C. Li, *Physical Chemistry Chemical Physics* **12**, 7083, **2010**.
24. I. a. Shkrob, M. C. Sauer, *The Journal of Physical Chemistry B* **108**, 12497, **2004**.
25. Y. Matsumoto, *Journal of Solid State Chemistry* **126**, 227, **1996**.
26. S. N. Habisreutinger, L. Schmidt-Mende, J. K. Stolarczyk, *Angewandte Chemie International Edition* **52**, 7372, **2013**.
27. K. Hashimoto, H. Irie, A. Fujishima, *Japanese Journal of Applied Physics* **44**, 8269, **2005**.
28. M. Tahir, N. S. Amin, *Applied Catalysis B: Environmental* **142–143**, 512, **2013**.
29. M. Anpo, H. Yamashita, Y. Ichihashi, S. Ehara, *Journal of Electroanalytical Chemistry* **396**, 21, **1995**.
30. M. Anpo, H. Yamashita, Y. Ichihashi, Y. Fujii, M. Honda, *The Journal of Physical Chemistry B* **101**, 2632, **1997**.
31. M. Anpo, H. Yamashita, K. Ikeue, Y. Fujii, S. G. Zhang, Y. Ichihashi, D. R. Park, Y. Suzuki, K. Koyano, T. Tatsumi, *Catalysis Today* **44**, 327, **1998**.
32. K. Mori, H. Yamashita, M. Anpo, *RSC Advances* **2**, 3165, **2012**.
33. C. Di Valentin, G. Pacchioni, *Catalysis Today* **206**, 12, **2013**.
34. F. C. Walsh, R. G. A. Wills, *Electrochimica Acta* **55**, 6342, **2010**.
35. H. Gerischer, *The Journal of Physical Chemistry* **88**, 6096, **1984**.
36. G. Liu, N. Hoivik, K. Wang, H. Jakobsen, *Solar Energy Materials and Solar Cells* **105**, 53, **2012**.
37. X. Chen, S. Shen, L. Guo, S. S. Mao, *Chemical Reviews* **110**, 6503, **2010**.
38. C. u. Gomes Silva, R. Juárez, T. Marino, R. Molinari, H. García, *Journal of the American Chemical Society* **133**, 595, **2011**.
39. C. Wang, R. L. Thompson, J. Baltrus, C. Matranga, *The Journal of Physical Chemistry Letters* **1**, 48, **2010**.
40. T. Peng, K. Dai, H. Yi, D. Ke, P. Cai, L. Zan, *Chemical Physics Letters* **460**, 216, **2008**.
41. R. Abe, K. Shinmei, K. Hara, B. Ohtani, *Chemical Communications*, 3577, **2009**.
42. J. Kim, D. Monllor-Satoca, W. Choi, *Energy & Environmental Science* **5**, 7647, **2012**.
43. A. Patsoura, D. I. Kondarides, X. E. Verykios, *Catalysis Today* **124**, 94, **2007**.
44. A. Fujishima, K. Honda, *Bulletin of the Chemical Society of Japan* **44**, 1148, **1971**.
45. A. Fusishima, K. Honda, *Nature* **238**, 37, **1972**.
46. T. Inoue, A. Fujishima, S. Konishi, K. Honda, *Nature* **277**, 637, **1979**.
47. A. J. Bard, *Science* **207** 139, **1980**.

48. F. Wagner, G. Somorjai, *Journal of the American Chemical Society* **102**, 5494, **1980**.
49. K. Domen, A. Kudo, T. Onishi, N. Kosugi, H. Kuroda, *The Journal of Physical Chemistry* **90**, 292, **1986**.
50. K. Domen, S. Naito, M. Soma, T. Onishi, K. Tamaru, *Chemical Communications*, 543, **1980**.
51. H. Kato, K. Asakura, A. Kudo, *Journal of the American Chemical Society* **125**, 3082, **2003**.
52. H. Kato, A. Kudo, *The Journal of Physical Chemistry B* **105**, 4285, **2001**.
53. A. Kudo, H. Kato, *Chemical Physics Letters* **331**, 373, **2000**.
54. K. Nakata, A. Fujishima, *Journal of Photochemistry and Photobiology C: Photochemistry Reviews* **13**, 169, **2012**.
55. D. Kowalski, D. Kim, P. Schmuki, *Nano Today* **8**, 235, **2013**.
56. O. K. Varghese, M. Paulose, T. J. Latempa, C. a. Grimes, *Nano letters* **9**, 731, **2009**.
57. K. Maeda, T. Takata, M. Hara, N. Saito, Y. Inoue, H. Kobayashi, K. Domen, *Journal of the American Chemical Society* **127**, 8286, **2005**.
58. Y. Sakata, Y. Matsuda, T. Nakagawa, R. Yasunaga, H. Imamura, K. Teramura, *ChemSusChem* **4**, 181, **2011**.
59. Y. Sakata, Y. Matsuda, T. Yanagida, K. Hirata, H. Imamura, K. Teramura, *Catalysis Letters* **125**, 22, **2008**.
60. Y. Sakata, T. Nakagawa, Y. Nagamatsu, Y. Matsuda, R. Yasunaga, E. Nakao, H. Imamura, *Journal of Catalysis* **310**, 45, **2014**.
61. H.-a. Park, J. H. Choi, K. M. Choi, D. K. Lee, J. K. Kang, *Journal of Materials Chemistry* **22**, 5304, **2012**.
62. H. Yoshida, K. Maeda, *Studies in Surface Science and Catalysis* **175**, 351, **2010**.
63. M. W. Kanan, D. G. Nocera, *Science* **321**, 1072, **2008**.
64. Y. Izumi, *Coordination Chemistry Reviews* **257**, 171, **2013**.
65. A. Dhakshinamoorthy, S. Navalon, A. Corma, H. Garcia, *Energy & Environmental Science* **5**, 9217, **2012**.

CHAPTER 2

METHODS

2.1 PHOTOCATALYTIC REACTION SETUP

2.1.1 BACKGROUND

This doctoral project was initiated as a new line in the research group, without specific and direct previous experience for photocatalysts and also appropriate reactor systems. Therefore, equipment and strategies for photocatalytic materials and reactor systems were designed and improved throughout the project in order to solve technical issues as well as to meet the demands of the scientific challenges arising.

The goal of this project was primarily to investigate CO₂ photoreduction in presence of water as the source of reducing agent (hydrogen atom or molecule) and to gain mechanistic insights. Photocatalytic water splitting is a reaction intimately related to the latter. This reaction is thermodynamically challenging and it is generally accepted to represent a prerequisite to reduce CO₂ to generate hydrocarbons and oxygenates like alcohols. Therefore the two photocatalytic pathways should be considered as coexisting reactions in photocatalytic CO₂ reduction. For these reasons the primary target reaction, CO₂ reduction, was accompanied by the study of water splitting as a parallel reaction (*chapter 3*) or as the main focus, when CO₂ reduction was not detected and outstanding H₂ production was observed (*chapter 4*).

The scientific community is paying an increasing attention to challenges related to energy and sustainability. Artificial photosynthesis is certainly one of them; experiencing an unprecedented growth in terms of number of publications, visibility and related discussions [1-7]. As a consequence, catalysts of different complexity and morphology with a variety of dopants, co-catalysts and their combinations have been reported. However, the efficiency of such processes is at the present time very low for practical application, resulting often in poor reproducibility. This is partly due to

sometimes peculiar and uncommon catalyst preparation methods, rendering the synthesis of reported catalyst materials difficult to be reproduced. Another, probably more important, cause for the irreproducibility is the absence of standardisation of equipment and photocatalytic reaction procedures. Lamps of different power and spectral irradiance, use of sacrificial agents, pretreatments and many other details could be responsible for radically varying results. Very importantly, proper use of materials and cleanness for the reactors and catalysts, especially in terms of carbon contamination, are of paramount importance and very seldom treated in literature [8].

The most common reaction setup reported in literature is the *slurry batch reactor*. Aqueous suspension of powder catalyst is typically saturated with gaseous CO₂ at atmospheric pressure and room temperature. A light source is then turned on and gaseous head space and liquid solution are sampled at regular intervals for chromatographic analysis of the products. The products slowly accumulate during several hours and their concentration can be monitored with a frequency of few samples per hour using a common GC or HPLC for gas and liquid phase products respectively. This approach allows the quantification of a wide range of gas and liquid products and has the advantage to allow the gradual accumulation of the products in a confined space. These compounds are normally detected in the ppm range of concentration and their detection is clearly enhanced at longer reaction times. On the other hand, this approach is only suitable to investigate the total productivity averaged over a long period of time (commonly in the range of several hours). Very little knowledge can be obtained on processes involving activation, deactivation or steady-state production, especially if different trends are co-present and overlapping (Figure 2-1a).

In order to discriminate these detailed features and investigate the dynamic catalyst response to different stimuli, e.g. under the alternation of irradiation and dark

conditions (switching on and off the light source) and temperature, an analytical technique with higher time-resolution is required (Figure 2-1b). In this project, quadrupole mass spectrometry was the analytic technique of choice, as it allows fast tracking (in a timescale of seconds, or even hundreds of milliseconds) of multiple molecular fragments in the product gas stream of a continuous flow reactor. Implementation of a MS coupled continuous flow reactor was technically more challenging as compared to a simple batch reactor, but finally resulted in a more flexible system being more informative about the reaction mechanisms.

In the following sections the photocatalytic reaction setups used in this project and the mode of operation will be described in detail.

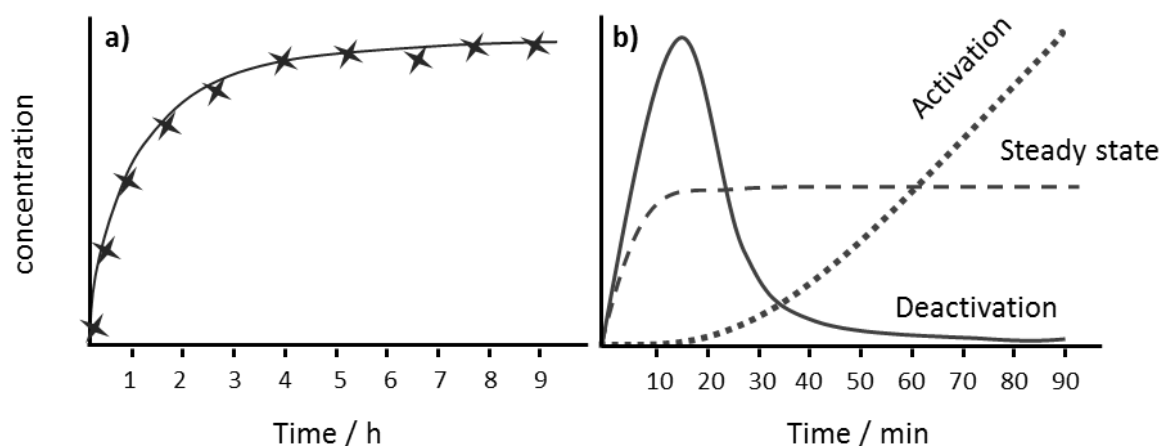


Figure 2-1. Example of product concentration profiles for: a) batch reaction monitored by gas chromatography; b) flow reaction monitored by mass spectrometry.

2.1.2 REACTION SETUP AND METHOD

The reaction setup in its typical operating configuration is schematically shown in Figure 2-2

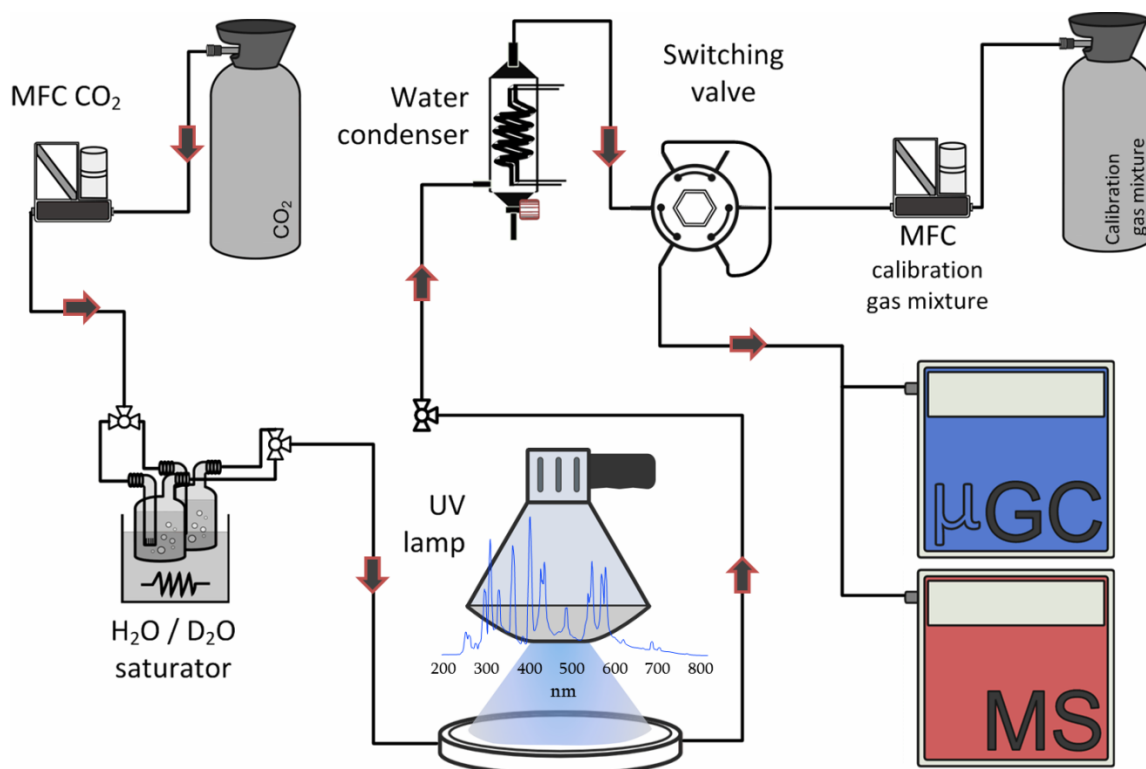


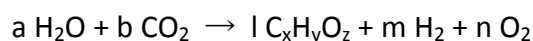
Figure 2-2. Continuous photocatalytic reaction system.

The reactor was equipped with (in the order of path for the gas flow):

- Gas supply system controlled by mass flow controllers (MFCs) to feed the system with gas CO₂ and calibration gas mixtures;
- Temperature controlled water saturators (H₂O and D₂O) to humidify the CO₂ stream;
- Gas phase (represented in Figure 2-2) or slurry photocatalytic reactor;
- High pressure mercury UV light source, equipped with programmable time switch;

- Water-cooled trap to condensate liquids from the gas stream and avoid their sampling by the GC and MS;
- Pneumatic switching valve used for calibration of the MS;
- MS (Pfeiffer Vacuum, Omnistar GSD 320) analytical system.
- GC (Agilent Technologies, micro GC 490) analytical system. Added to the system at a later stage of the project.
- Control system for MS (software Quadera), GC and *LabVIEW* for PID heat controllers and relays (programmable time switch)

In a nutshell, the purpose of the system is to deliver a steady and precisely regulated stream of H₂O saturated CO₂ to a continuous flow photoreactor (the design of which will be discussed in the following sections), where the reaction



takes place in presence of UV-light irradiation.

The sealing of the system is extremely important to properly quantify the products and to minimize the contamination of the system with atmospheric oxygen. This is particularly critical because materials catalysing artificial photosynthetic processes promote the opposite process; mineralization of organic compounds, where oxygen works as the oxidising agent. Consistently, prior to catalytic runs the system was flushed with water saturated CO₂ (*w*-CO₂) and then checked for gas tightness up to an inner pressure of 2 bars. Afterwards, the pressure was released and a steady *w*-CO₂ flow was set to a defined value (ca. 4.5 ml·min⁻¹) and let stabilise until a stable signal was obtained by the on line MS. At the flow and MS signal stabilisation (typically less than 30 min) calibration of gaseous products concentrations was performed (see *section 2.1.3*). Subsequently, the light source was turned on and the formation of products due to photocatalytic activity was monitored in real time. After the designed

experiment was completed, the calibration procedure was usually repeated. The time-dependant traces of the followed mass fragments were then processed according to the calibrations to finally yield time-dependant concentration profiles. As a further development, a micro GC instrument was added at a later stage of the project, in parallel to the MS system. It was equipped with a backflush optimised molecular sieve (5A) column that allowed detection and quantification of permanent gases. It was used to confirm or substitute the MS calibration as further explained in the next section.

2.1.3 ANALYTICAL SYSTEM

The MS (Pfeiffer Vacuum, Omnistar GSD 320) is equipped with a quadrupole mass analyser capable of separating fragments with molecular mass to charge ratio (m/e) up to 100. It is designed exclusively for the analysis of gases, therefore a water cooled condenser was used to trap liquids (mostly water from the feed gas) and avoid contamination. The analysis chamber is kept under high vacuum ($\approx 10^{-9}$ bar) by a turbomolecular pump. A system with pre-chambers and a membrane pump produces a gradient of pressure up the atmospheric pressure at the continuous sampling capillary port. Before the sampling capillary, a flow splitting device (essentially a T-piece open to atmospheric pressure), must be placed to avoid overpressure at the inlet of the MS. The geometry of the splitter can affect the signal intensity and the response speed, depending on dead volume and tube diameter; its configuration must be maintained fixed during the reaction operation.

In multiple ion detection mode (MID) the MS dedicates a programmable time (down to few milliseconds) to the isolation and detection of each mass fragment in the stream of the ionized gas produced by a filament. In the scale of seconds or minutes the pre-selected mass signals appear as a bundle of continuous time traces. The signal intensity is proportional to the ions concentration and can be used for their

quantitative analysis. It is noteworthy that MS analysis requires more careful handling in order to get consistent measures as compared to GC analysis. Change in inlet pressure, cleanness of the chamber and contamination can dramatically affect the baseline of the signals and the response to concentration change. For this reason multiple calibrations of the system were performed in proximity of a catalytic testing (before and after the testing, and even during *dark times* between runs).

The calibration was performed in continuous flow condition, passing a stream of calibration gas mixture by means of a pneumatic 6 way valve (Valco) equipped with a 35 μl sample loop (Figure 2-3).

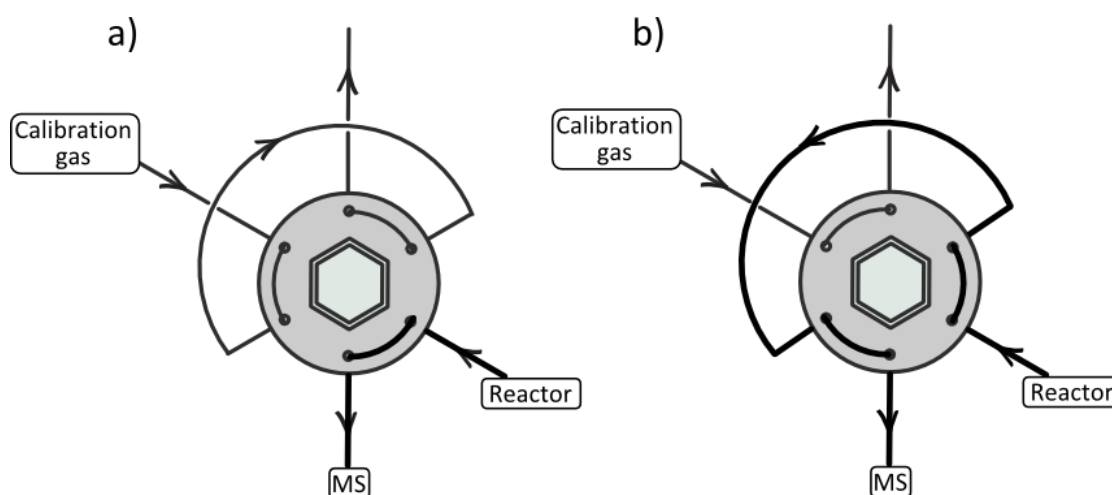


Figure 2-3. 6-way valve operation during a) reaction and b) calibration gas mixture injection. Thick lines describe the path of the reaction gas stream finally detected by MS, whereas the thin ones show the path of the calibration gas mixture.

Under reaction conditions the valve is in position a) and the effluent stream from the reactor flows directly to the MS, whereas on the parallel circuit the sample loop is continuously fed with the calibration gas mixture at atmospheric pressure. Upon switching the valve to b) position, the reactor stream flows through the sample loop carrying the calibration mixture to the MS. The MS response to the calibration mixture

injection is shaped into a peak. Multiple injections of the calibration gas mixture assure reproducibility of the procedure. During the data processing, the peaks are integrated to obtain a response value k for each gas in the mixture (Equation 2-1; each k factor is weighed on the concentration of the gas considered in the total volume of gas mixture injected); along with the volumetric flow ϕ , this value is sufficient to calculate the conversion factor k_{conc} (Equation 2-2) to express the reaction profiles in terms of concentration (volume or molar ratio) (Equation 2-3).

Equation 2-1. $k = \text{Integrated MS signal (peak)} / \text{Volume of calibration gas injected}$

Equation 2-2. $k_{conc} = k \phi$

Equation 2-3. $\text{Concentration} = \text{MS signal} / k_{conc}$

Figure 2-4 depicts the typical profiles along a catalytic testing for H_2 and CH_4 gaseous products along with their calibrations peaks. The concentrations were normalized on the catalyst weight in grams. The details of the results will be described in more detail in *chapter 3*.

If a GC is also used in parallel to the MS, valve injection for calibration can be avoided. A few GC injections, in presence of the gases of interest in the outlet stream from the reactor, are sufficient to quantify their concentration at desired times. These values can subsequently be used as *in situ* calibration reference value for the MS signal. Normalization of such curves obtained by MS with the conversion factor determined by GC finally yields reliable concentration vs. time profiles.

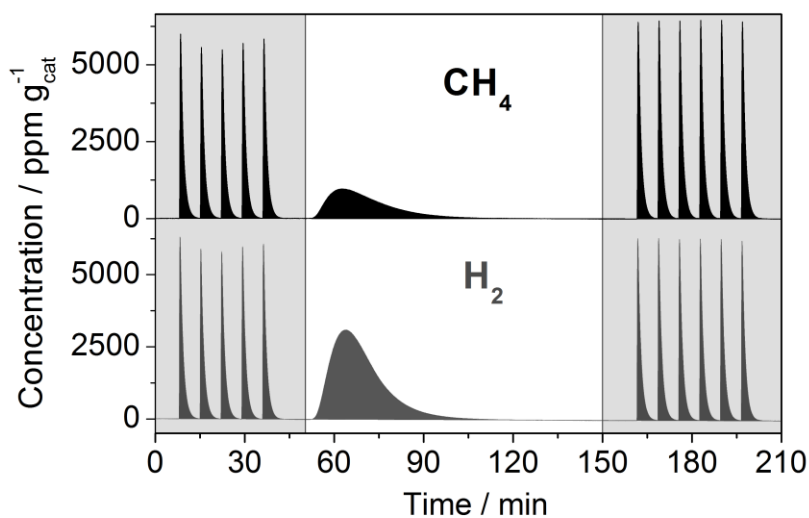


Figure 2-4. Example of H_2 and CH_4 concentration profiles during catalytic testing under UV-irradiation (50-150 min). In the shaded zones before and after the reaction multiple sequential calibration peaks are shown.

2.1.4 REACTOR

Two reactor types were examined, namely (i) gas phase reactor and (ii) liquid phase (slurry) reactor.

For gas phase testing (i.e. catalysts are in contact with reactants in gas phase), a thermally controlled round aluminium reactor was designed and developed (Figure 2-5). It was equipped with a UV transparent fused silica window allowing the irradiation of a powder catalyst, uniformly deposited over the flat bottom of the reactor by means of a metallic sieve. The inner volume of the reactor was 16.1 ml and the effective area available for irradiation was 32.2 cm^2 . The reactor was connected to the rest of the system by one gas inlet and one outlet, mutually positioned at 180° angle. Two parallel 7 mm diameter cylindrical cavities were positioned below the reactor surface (where catalysts sit) to serve as heating cartridge slot. Between the two heating cartridges, a

third 2 mm diameter cavity was placed, reaching the centre of the cell, to insert a thermocouple for temperature measurement of the reactor (effectively considered as catalyst temperature judging on the proximity between the catalyst and thermocouple).

In order to avoid corrosion of the metal body, due to temperature and high intensity irradiation in the water saturated stream, an anodizing treatment (ca. 12 V, 1 h) in 20 % sulphuric acid was applied, followed by a treatment in boiling DI water to seal aluminium oxide pores. The electrochemically generated aluminium oxide layer made the surface more mechanically and chemically resistant.

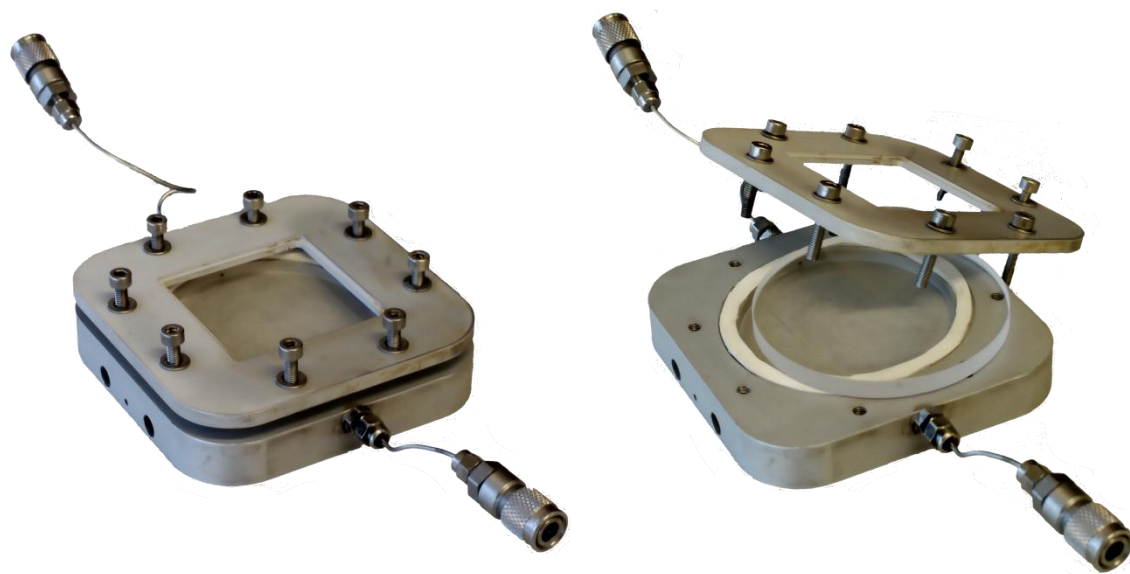


Figure 2-5. Continuous flow gas phase photocatalytic reactor.

The sealing of the fused silica window with the metallic body was achieved by tightening the assembly with a matching top cover by eight M3 screws, using an O-ring as sealing element between the window and the body (Figure 2-5). The O-ring material is critical, as UV and temperature resistance are of the highest importance. Nitrile based materials have to be avoided, as they rapidly deteriorate under relatively mild operating conditions ($T > 373$ K and 100 W UV lamp); this resulted in detection of

artefact hydrocarbons production with concentration $> 1\%$, invalidating the catalytic tests. Good resistant materials were found to be perfluorinated polymers such as Teflon and Kalrez (*DuPont*), and silicone rubber. Silicone rubber was generally preferred as it allowed shaping it into flat O-rings with superior elasticity and heat resistance up to 473 K. Kalrez O-rings probably offer the best UV and temperature resistance. Nevertheless their common toroidal shape did not suit at best our reactor design. Also frequent sealing/unsealing operation restricted their lifetime considerably due to mechanical stress.

The slurry reactor consisted of a two-pieces glassware vessel (Figure 2-6). The bottom part was a round bottom UV transparent quartz tube (35 ml up to the ground joint) which could be joined, by means of ground glass cones, to a glass head (providing 36.5 ml headspace) with GL13 screw inlet and outlet.



Figure 2-6. Continuous liquid phase (slurry) photocatalytic reactor

At the inlet, a glass capillary (ID \approx 2 mm) was sealed, reaching the bottom of the quartz tube, for bubbling CO₂ in the suspension. A powder catalyst (20 mg, 0.57 g·L⁻¹) was typically suspended in Type-I ultrapure water (Milli-Q) and kept under agitation by means of a magnetic stirrer. In order to facilitate the suspension formation and the dissolution of agglomerates, the reactor could be briefly dipped in an ultrasound bath previous to connection to the setup.

2.1.5 LIGHT SOURCE AND FILTERS

Light source is the core and trigger of the photocatalytic setup, providing the energy required for the photosynthetic process. The final aim of artificial photosynthesis is the utilization of sunlight as driving force for chemical reactions. Even though much effort is currently focused on extending the effectively useful fraction of sunlight into the Vis range, most of the available catalysts are still based on wide-bandgap metal oxides, which are only active under UV irradiation. Thus, UV light sources were the necessary starting point for our purposes. The most common and practical UV light sources are the discharge mercury lamps. Depending on the mercury vapour pressure developed inside the bulb after the high voltage starting discharge, high- and low-pressure mercury lamps are available.

The lower the Hg pressure the narrower the emission lines and the higher the UV/Vis intensity ratio. High pressure lamps are most commonly preferred for photocatalytic purposes, as they can deliver more light intensity in a wide spectrum ranging from 250 to 800 nm and peaking in the blue-violet fraction of the visible light.

Mainly three different high pressure Hg lamps were used. For purely catalytic testing, a 100 W *handy cure HLR400T-1* (Senlight corp.) with a nominal UV-light

intensity of $170 \text{ mW}\cdot\text{cm}^{-1}$ (specified by the supplier) and a 400 W custom lamp (UV-technik) were employed.

The second was controlled by a dimmable electronic ballast (*Solux*), capable of providing a voltage spike for lamp ignition and dimming the power output to the lower value of 200 W, which was typically applied.



Figure 2-7. High-pressure Hg Lamps used for photocatalytic testing: 100 W *handy cure HLR400T-1* (Senlight corp.) on the left; and a 400 W custom-made lamp (UV-technik) on the right.

Although the second lamp delivers more light intensity and luminance, it is important to point out that the power figures stated above are not exactly scalable with the intensity and have just nominal value. These two lamps could be remotely switch on and off, also in a time controlled fashion (in a timescale ranging from minutes to several hours). These operations were controlled by an in-house designed *LabVIEW* interface, controlling a *KMtronic* relay in series with the power mains.

The third lamp, a *Swift cure PLU 10 (UV consulting Peschl)*, was mainly dedicated to spectroscopy studies. This light source features a 3 mm core quartz optical fiber that can flexibly deliver a directional UV-Vis beam onto a small area of few cm^2 . A 5 V TTL

controlled built-in shutter also allows the interruption of irradiation. This could be efficiently time programmed by the spectrometer software allowing synchronization of irradiation and spectra acquisition.

According to the spectrum range of interest for testing, a UV (275-375 nm) band-pass filter and a Vis ($\lambda > 400$ nm) long pass filter (respectively FGUV11S and FGL400S, *Thorlabs*) were used to isolate the UV or Vis component. For the same purpose, an optical quality borosilicate window (BK7, *Eksma Optics*) was also employed in place of the fused silica (UVFS) one, when cutting off UV at $\lambda < 300$ nm was required (Figure 2-8).

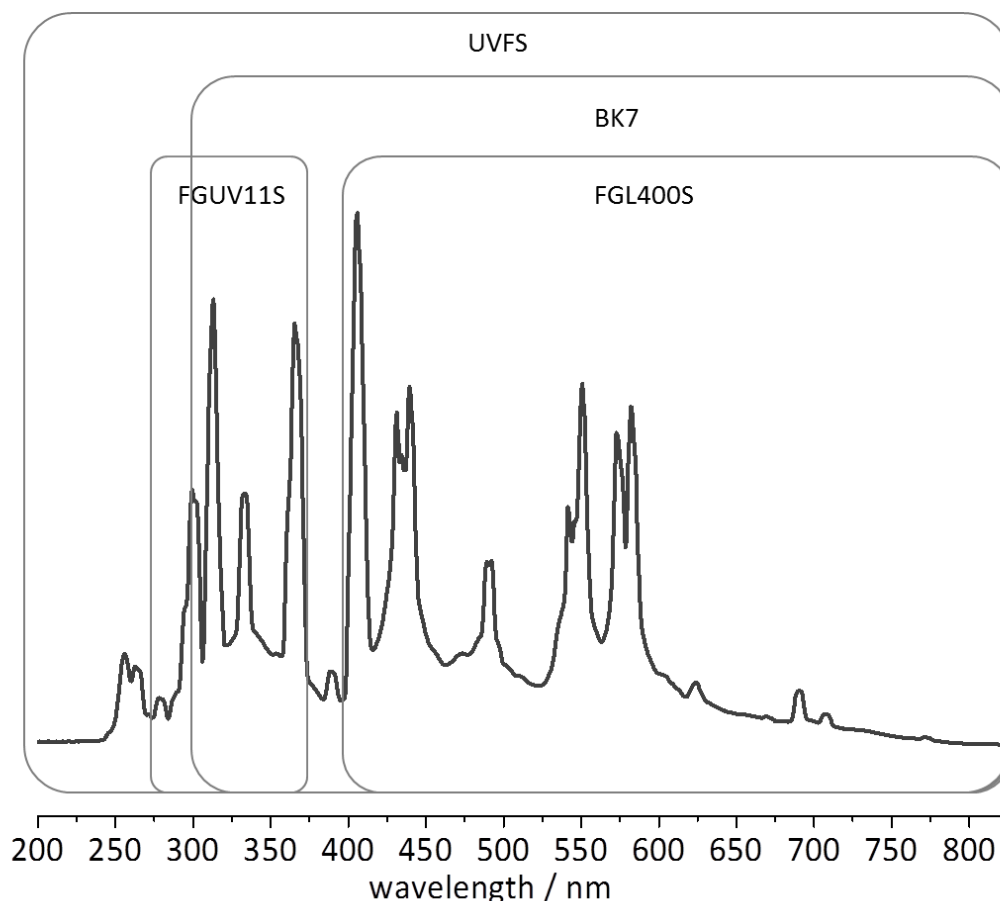


Figure 2-8. Emission spectrum (intensity in arbitrary units) of Senlight Corp. 100 W *handy cure HLR400T-1* high pressure Hg UV light. Acquired with Avantes UV-Vis spectrometer. The UV and Vis ranges isolated by the filters (i.e. the range of light not filtered and passing to a sample) are shown.

2.2 INFRARED SPECTROSCOPY SETUP

2.2.1. DRIFT SPECTROSCOPY

Infrared spectroscopy is one of the most sensitive and informative techniques for the investigation of the active species and sites in catalytic processes, as most molecules and materials absorb IR radiation at characteristic vibrational frequencies. Time-resolved acquisition of IR spectra can give dynamic information on the formation or consumption of these chemical species and sites, helping unravelling the underlying mechanism of the reaction and its active actors. The general concept of IR absorption spectroscopy relies on the absorption of specific IR frequencies, by specific chemical structures, in the wide spectrum of emission generated by a source. Interaction between the IR radiation and the sample must be maximized to trigger relevant absorption and, depending on the system under investigation, different sampling geometries are available. Depending on how IR radiation is collected relatively to the sample, transmission or reflection geometries are available. Among the reflection geometries, specular, attenuated internal or diffuse reflection mode can be adopted. Belonging to the last class, diffuse reflectance Fourier transform infrared spectroscopy (DRIFTS) is certainly the most suitable for the investigation of heterogeneous powder catalysts in gas phase reactions. This is due to the fact that under these conditions the light hitting at the surface can scatter through the powder material and interact multiple times with the particles before being reflected out of the sample in a diffuse fashion (enhancing the absorption phenomena). At the same time the reflection interaction involves only a thin layer of the single particles (few nm). It is only in this range that absorption of IR light is possible, resulting in high surface sensitivity of

DRIFTS. For these reasons, DRIFTS was selected as the main chemical analytic technique to obtain deeper insight into the photocatalytic process.

2.2.2 DIFFUSE REFLECTANCE ACCESSORIES AND UV EXCITATION SETUP

DRIFTS requires specific optical guides to couple to the spectrometer. The light coming from the source has to hit the catalyst powder, be diffusely reflected and collected in a wide dihedral angle to be sent to the detector. This task was performed by a *Praying Mantis* (Harrick) optical system equipped with a series of mirrors for redirection and collection of diffuse reflected light as well as minimization the detection of specularly reflected light (Figure 2-9).

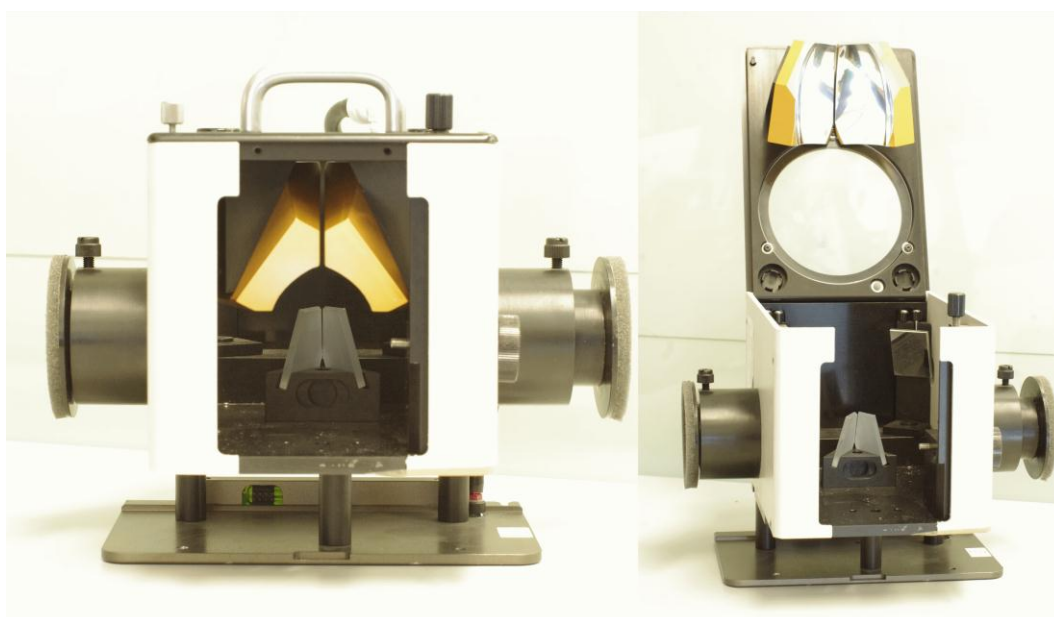


Figure 2-9. Praying Mantis diffuse reflectance mirror system accessory.

At the centre of the system, a *HVC DRP* (Harrick) reaction chamber was mounted (Figure 2-10). This is composed of a central sample holder, capable of local heating and inlet/outlet connections allowing continuous flow through operation. A refrigeration loop permits cooling of the stainless steel body. The chamber is closed by means of an O-ring sealed, screw tightened top cover with three optical windows, positioned

respectively at 120° from the centre of the chamber. Two of them are made of IR transparent CaF, whereas the third one was substituted by a fused silica window. The latter works as a UV light port for excitation of the catalyst (Figure 2-11). FGUV11S UV band pass filter was also installed on the optical port since high intensity long wavelength irradiation heavily interfered with the IR detection system.

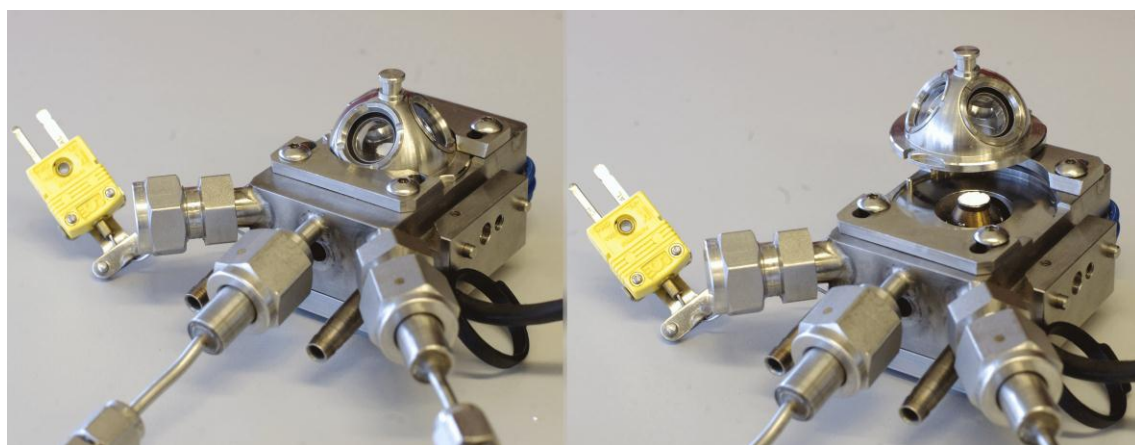


Figure 2-10. Harrick's *in situ* diffuse reflectance continuous flow reaction cell.

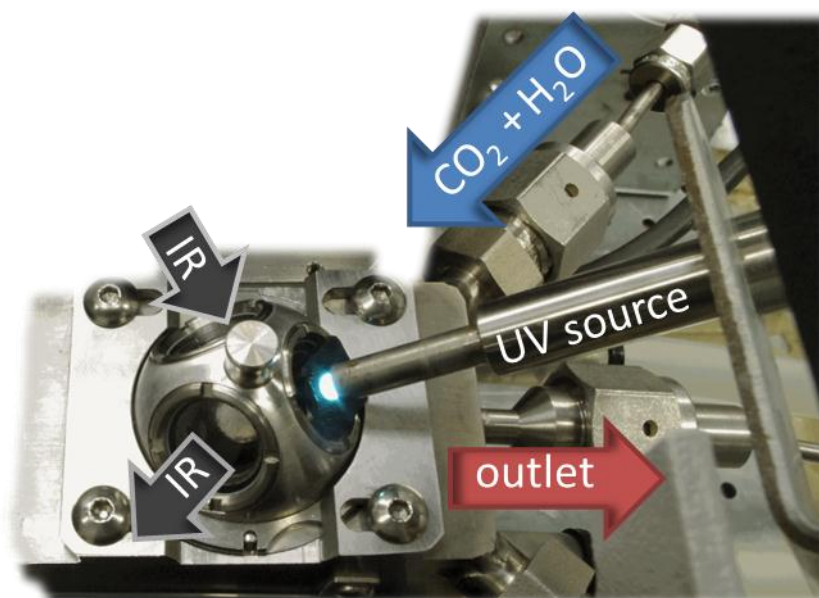


Figure 2-11. Mounted DRIFTS cell under *in situ* operation.

The spectra were collected on a Vertex70v FTIR spectrometer (*Bruker*) equipped with a liquid-nitrogen-cooled mercury-cadmium-telluride (MCT) detector.

2.3 PHOTOPHYSIC CHARACTERIZATION OF MATERIALS

2.3.1 IMPORTANCE OF OPTICAL/PHOTOPHYSIC PROPERTIES

The activity of a photocatalyst is intimately related to its photophysical properties. The efficiency of the process is dependent on how efficiently the material absorbs and harvests light. The material has to efficiently absorb electromagnetic radiation in the widest possible range of frequencies, in order to maximally utilize the amount of input energy fed to the process. Ideally, the range of absorption of a photocatalyst matches with the solar light irradiance spectrum, ranging from UV through visible (where the sun irradiate at the maximum intensity) to the first portion of the infrared (NIR, which is the most extended and represents most of sun's energy). However the absorption of light itself, despite being a necessary step, is not a sufficient condition to ensure high photocatalytic activity. Specific chemically active structures and high overpotentials were so far proven to be needed in order to drive photosynthetic class reactions. This fact is restricting the active photocatalysts to a limited class of materials and Ti, Ta and Ga oxides (studied during this doctoral project) are important examples. These materials are all sharing the common feature of being high bandgap semiconductors, with deeply buried O 2p valence bands, resulting in the restriction of UV excitation and limited or absent visible light activity.

The next sections will give an overview of the analytical methods used along this doctoral project, focusing on the theoretical background. Details of experimental parameters and results are summarized in *chapter 5*.

2.3.2 UV-VIS DIFFUSE REFLECTANCE SPECTROSCOPY

UV-Vis diffuse reflectance spectroscopy is a powerful technique for characterizing solid photocatalysts as it gives access to the light absorption features of a material, i.e. the first key step to the transformation of light energy into chemical energy. Semiconductors display an *onset* of absorption rather than absorption bands which are common for molecular compounds and metal nanoparticles. This *onset* defines the longest radiation wavelength that can be absorbed by a material. In other words, it defines the *optical bandgap* of a material (E_g), i.e. the minimum photon energy needed to promote an electron from the valence band to the conduction band. If the material thickness is not a limitation (e.g. using less than a few hundred microns thick powder sample), all the photons with higher energy than E_g are fully absorbed by the material, whereas the ones with lower energy are transmitted or scattered. The onset typically occurs within a range of a few tens of nanometers in wavelength where light absorption turns from nearly zero to 100 %. An estimate of the bandgap can be determined from absorption or diffuse reflectance spectra of a material. This methodology was pioneered theoretically and experimentally by I.P. Shapiro [9] and J. Tauc [10]. It then became a very common procedure in the field to estimate λ_{onset} and thus E_g from the linear fit to the steep dip in the absorption curve and from the position where the value equals to zero in absorbance. Different models and interpretation based on a multitude of parameters have been proposed during the past years to explain the light absorption features. The absorption, reflectivity, and scattering properties of the material as a whole contribute to the physical measurement and should be taken into account when choosing a model for correct interpretation [11, 12]. Thickness of the sample or their nanostructure are also critical parameters [11, 13, 14].

The transmission absorption spectroscopy is not suited for opaque solids due to their relatively high optical density, resulting in quick saturation in light absorption. For this reason, this analytical technique typically requires thin film preparation of sample material or dilution in non-absorbing agents. Furthermore, commonly used powdered materials have prominent light back scattering properties. For this reason, diffuse reflection UV-Vis spectroscopy is generally the most efficient and the preferred technique for the determination of light absorption properties. As reported by R. Lopez and R. Gomez [13], many slightly different approaches, giving often contradictory and unreliable results [11], are reported in literature by the photocatalysis community for optical bandgap calculation. Nevertheless, they also demonstrated how these differences can be settled into a sufficiently accurate and equally simple method for powder samples by using a corrected diffuse reflectance Kubelka-Munk function (Equation 2-4) for the linear fit of the absorption dip. The function can be corrected by an exponential factor taking into account the nature of the absorptive transition of the semiconductor material, namely *direct allowed* or *indirect allowed transition*.

Reflectance (R) is defined as the ratio of diffuse-reflected light intensity over incident light ($R(\lambda) = I(\lambda)/I_0(\lambda)$), where $I_0(\lambda)$ can be experimentally obtained using a standard with similar properties, but maximally reflected light in the sampled λ range). Then Kubelka-Munk (KM) function for spectra representation is defined as a function of R as follows

$$\text{Equation 2-4. } KM(\lambda) = (1-R)^2 / 2R.$$

This equation better accounts for the absorption phenomena occurring along with the diffuse reflection than how light absorbance is calculated ($A(\lambda) = -\log_{10} I(\lambda)/I_0(\lambda)$), which is usually more valid using transmission sampling configuration. Alike absorbance in transmission geometry, $KM(\lambda)$ function is proportional to the extinction coefficient of the material, $\alpha(\lambda)$.

Since the slope of the reflectance curve is used for graphic bandgap calculation, the function we use to represent the reflectance is highly critical. It has been shown that a multitude of factors should be taken into account to correct KM function depending on the material and specific application of the function [13].

A common procedure, based on further development of Tauc theory, is to rescale KM to KM' as follows:

$$\text{Equation 2-5. } KM' = (KM(\lambda) hv)^{1/n},$$

where $h\nu$ is the spectral photon energy and $n = 1/2$ for direct allowed transitions; 2 for indirect allowed transitions, 3 for indirect forbidden transitions, and 3/2 for direct forbidden transitions (where forbidden transitions are much less probable than allowed and are rarely considered). This correction would ensure a better linearity with $\alpha(\lambda)$, which is the correct physical entity to use Tauc plots.

In contrast to what has been reported by R. Lopez, in our experience the best agreement with literature data (in particular dealing with the well-known properties of P25 titania) was obtained by directly using the unmodified KM function for bandgap calculations. Therefore KM vs. λ plots were used for the bandgap calculations of all materials under investigation of this thesis project.

2.3.3 PHOTOLUMINESCENCE SPECTROSCOPY AND DECAYS

Photoluminescence (PL) spectroscopy is a very informative tool for the characterization of photocatalysts. The mechanism leading to light emission follows very similar principle and pathways as the photocatalytic ones. In both phenomena, a light excitation drives the formation of an electronic excited state, which can further evolve into excitons and to charge separation states. Regardless of its nature, the excited state is bound to decay, and this can occur in two ways: in a radiative path (pathways c and e in Figure 2.12) or in a non-radiative path (pathway f). The former

leads to different kind of luminescence, while specific paths of the latter, non-radiative path, can lead to formation of trapped surface charged state (catalytically active site) being reactive towards other chemical species in the surrounding. The excitation (pathway a) is common for both pathways. If a catalyst modification promotes the lifetime of the excited state, this is likely to trigger an enhancement in both luminescence and catalytic properties. Focusing on luminescence, under equilibrium condition of light excitation (which is the condition of typical PL spectral measurements), more populated and longer living excited state translates into more intense signal of PL bands.

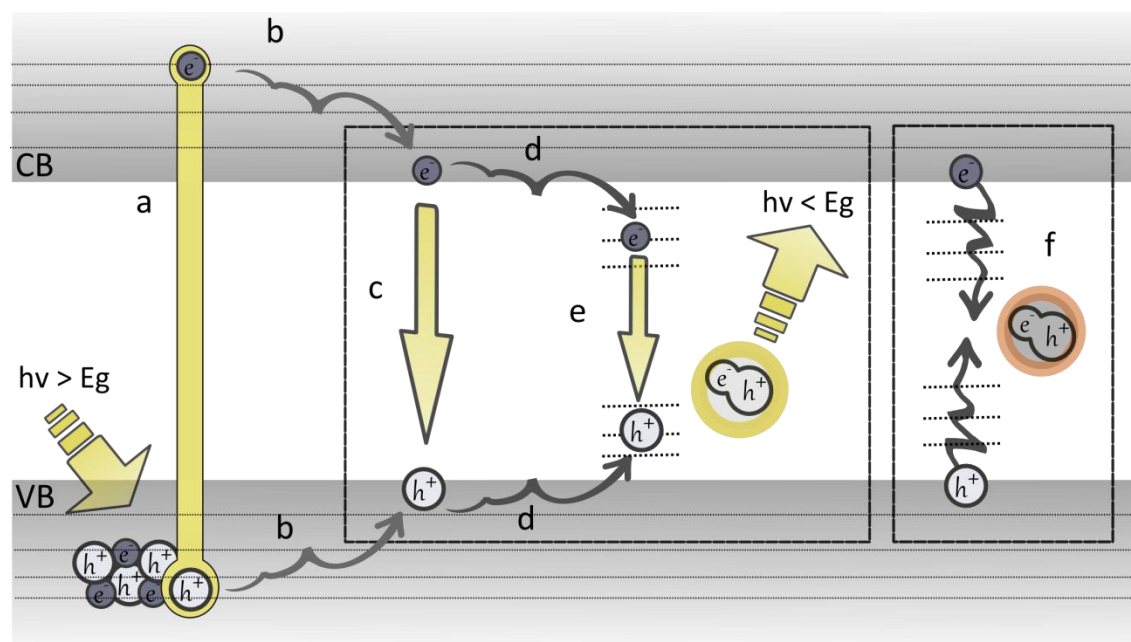


Figure 2-12. Pictorial representation of events associated with light absorption and emission in a semiconductor: a) excitation and charge separation; b) non-radiative relaxation of charges to band edges; c) radiative band-to-band recombination; d) further non radiative relaxation of charges to intra bandgap trap states (also possibly surface state); e) radiative recombination of lower energy than c (referred in the text as exciton emission); f) totally non radiative recombination.

However establishing a relation between PL band intensity and photocatalytic activity is not trivial because a multitude of complex electronic processes can be

present, including exciton formation/relaxation and trapping of charges in energetically shallow or deep (stable) states such as bulk or surface defects. The final spectra are the sum of many possible radiative recombination pathways (possibly preceded by a number of non-radiative relaxation phenomena) and this makes it hard to describe the phenomenon with simple models. A useful distinction used when dealing with PL-catalysis relationship is the one between band-to-band PL and excitonic PL [15]. Band-to-band PL is a radiative recombination due to the electron relaxation between CB and VB edges. Only a minor amount of energy is dissipated to relax the electron and the hole to the bottom of CB and to the top of VB, respectively. The resulting light emission has energy close to the bandgap value, i.e. the highest generally observable. The difference between excitation and emission wavelengths (*Stoke shift*) can in this case be as little as few nanometers. Excitonic PL, on the contrary, groups those radiative phenomena occurring after a series of relaxation processes like possible separation of the exciton into trap states in the bulk or the surface of the material (pathway d). Typical excitonic bands are generated from recombination of charges trapped in oxygen vacancies or defects in semiconductors. Stoke shifts of excitonic bands are larger (easily > 200 nm) and at the same time extremely variable. Their wavelength depends on the number and the relative energy level of the trap states in which the charges are hopping before radiative recombination.

The surface of a material is commonly rich in defects which can act as charge traps. They certainly contribute in large part to excitonic PL. As noted above such traps can be important for catalysis and consequently defective surfaces are considered to bear catalytic active sites. Therefore it is natural to look for correlation between excitonic PL and catalytic activity, rather than focusing on band-to-band PL. According to this scheme, a rise in excitonic PL intensity could be seen as an indication for good catalytic

potential. Nevertheless, band-to-band PL intensity may be (anti-)correlated with catalytic activity. It was hypothesized that higher band-to-band PL intensity revealed higher electron-hole recombination rate, thus being detrimental for slow catalytic processes by spoiling active charge separation before having the time to use it to drive chemical reactions [15].

As a matter of fact, dynamics of photogenerated charges are a very complex subject. The information gained from simple PL spectra is reflected by tremendous amount of phenomena occurring simultaneously with multiple kinetic timescales. The challenge can be certainly more properly tackled by non-equilibrium time-resolved techniques. Among these we find PL decay and *pump and probe* techniques, such as transient absorption spectroscopy (TAS). In PL decay experiments, an excited state is generated with a fast light pulse (usually laser) and the resulting decaying photoluminescence is sampled (at a desired λ) vs. time. In TAS a similarly short light excitation is flashed (the “pump”) in order to populate the excited species state. Another time resolved group of pulses with wavelength λ' , is then used as “probe”. The transient absorption of the probe light by the excited state species can finally give information of these states concentration vs. time.

Even using these tools, the picture is often far from being well-understood and literature is surprisingly rich with different models for charge trapping dynamics. The timescale of reported recombination phenomena investigated using such techniques can easily range from 10^{-10} to 10^{-4} seconds [16-22] (mostly based on titania). This fact can make the rationalization of the charge dynamics extremely dependent on the timescale we are looking at. The temperature and the environment of measurement (i.e. gas or solution, presence/absence of chemically interacting species) can also make a profound difference [19, 23].

Despite such drawbacks, these techniques could be a very useful tool. Especially when comparing photophysical properties of materials of the same family, but with different modifications. Considering the lifetime of an excitonic emission, it is reasonable to consider that a longer PL decay is symptom of longer lifetime of reactive surface species i.e. longer time to perform catalysis. Also if we modify a material with the purpose to introduce non-radiative and chemically active charge traps or if we add charge scavengers in the environment (oxygen, organic compounds etc.), we expect PL quenching. The way a catalyst modification affects the PL decay could be used to support or contrast one's mechanistic hypothesis, and help defining the role of dopants and co-catalysts as demonstrated in this project (*chapter 5*).

BIBLIOGRAPHY

1. G. Liu, N. Hoivik, K. Wang, H. Jakobsen, *Solar Energy Materials and Solar Cells* **105**, 53, **2012**.
2. A. Dhakshinamoorthy, S. Navalon, A. Corma, H. Garcia, *Energy & Environmental Science* **5**, 9217, **2012**.
3. Y. Izumi, *Coordination Chemistry Reviews* **257**, 171, **2013**.
4. S. N. Habisreutinger, L. Schmidt-Mende, J. K. Stolarczyk, *Angewandte Chemie International Edition* **52**, 7372, **2013**.
5. M. Matsuoka, M. Kitano, M. Takeuchi, K. Tsujimaru, M. Anpo, J. M. Thomas, *Catalysis Today* **122**, 51, **2007**.
6. M. Ni, M. K. H. Leung, D. Y. C. Leung, K. Sumathy, *Renewable and Sustainable Energy Reviews* **11**, 401, **2007**.
7. K. Maeda, K. Domen, *The Journal of Physical Chemistry Letters* **1**, 2655, **2010**.
8. C.-C. Yang, J. Vernimmen, V. Meynen, P. Cool, G. Mul, *Journal of Catalysis* **284**, 1, **2011**.
9. I. P. Shapiro, *Optikal Spektroskopie* **4**, 256, **1958**.
10. J. Tauc, R. Grigorovici, A. Vancu, *physica status solidi (b)* **15**, 627, **1966**.
11. A. B. Murphy, *Solar Energy Materials and Solar Cells* **91**, 1326, **2007**.
12. A. B. Murphy, *Applied Optics* **46**, 3133, **2007**.
13. R. López, R. Gómez, *Journal of Sol-Gel Science and Technology* **61**, 1, **2012**.
14. N. Ghobadi, *International Nano Letters* **3**, 2, **2013**.
15. J. Liqiang, Q. Yichun, W. Baiqi, L. Shudan, J. Baojiang, Y. Libin, F. Wei, F. Honggang, S. Jiazhong, *Solar Energy Materials and Solar Cells* **90**, 1773, **2006**.
16. M. R. Hoffmann, S. T. Martin, W. Choi, D. W. Bahnemann, *Chemical Reviews* **95**, 69, **1995**.
17. A. Yamakata, T.-a. Ishibashi, H. Onishi, *Chemical Physics Letters* **333**, 271, **2001**.
18. N. Serpone, D. Lawless, R. Khairutdinov, E. Pelizzetti, *The Journal of Physical Chemistry* **99**, 16655, **1995**.
19. J. Tang, J. R. Durrant, D. R. Klug, *Journal of the American Chemical Society* **130**, 13885, **2008**.
20. I. a. Shkrob, M. C. Sauer, *The Journal of Physical Chemistry B* **108**, 12497, **2004**.
21. D. W. Bahnemann, M. Hilgendorff, R. Memming, *The Journal of Physical Chemistry B* **101**, 4265, **1997**.

22. J. J. Cavaleri, D. P. Colombo, R. M. Bowman, *The Journal of Physical Chemistry B* **102**, 1341, **1998**.
23. K. Mori, H. Yamashita, M. Anpo, *RSC Advances* **2**, 3165, **2012**.

CHAPTER 3

TiO₂ AND Pt/TiO₂ CATALYSTS FOR CO₂ PHOTOREDUCTION

3.1 INTRODUCTION

Ti-based photocatalysts are well known and widely reported in literature for CO₂ photoreduction [1]. Nevertheless, most of the reported work to date is based on photocatalytic reaction using batch-slurry reactor setups; CO₂ photocatalytic reduction is typically conducted in a batch reactor by irradiating a stirred aqueous suspension of a catalyst with UV or visible light after saturation with CO₂. Gaseous headspace and aqueous solution are sampled and analyzed by means of GC, recording a few points per hour for a total reaction time in the order of hours as discussed in *chapter 2*. Also, very common in this field is the use of sacrificial electron donors such as OH⁻ ions and light organic compounds, such as methanol, to improve the reduction efficiency.

Recent reviews by Liu et al. [2], Dhakshinamoorthy et al. [3], and Izumi [4] summarize the historical perspective and the state-of-the-art in titania-based photocatalysts and reactor configurations. Importantly, very few reports are available on the reaction in a continuous operation [5, 6], despite clear practical advantages of such an operation for scale-up and product separation.

In this chapter, the dynamic nature of continuous photocatalytic reduction of gaseous CO₂ in the presence of water vapor and in the absence of sacrificial electron donors is presented. TiO₂ and Pt/TiO₂ were used as model catalysts and tested under UV irradiation at 353 and 423 K. A novel MS-based analytical approach (*chapter 2*) was used to study the reaction with a good time resolution (order of seconds) and to monitor product concentrations.

Two distinct photocatalytic activities, namely steady-state and transient, were identified. The former is active at the lower temperature and only for H₂ production, whereas the latter dominates for CH₄ production. The transient activity was recovered

during *dark time* (i.e. the light is off) in the reaction mixture, with the magnitude of recovery proportionally increasing with the duration of the dark time. Higher temperature was found to be more effective for the recovery. Furthermore, insights into deactivation and reactivation mechanisms are explained by *in situ* DRIFTS.

3.2 EXPERIMENTAL SECTION

3.2.1 CATALYST PREPARATION

P25 titania (*Degussa*) prepared by flame pyrolysis was chosen as photocatalyst because it is the most widely studied material for both photocatalytic CO₂ reduction and H₂O splitting. The starting white powder was calcined at 773 K in air for 3 h prior to use. Platinum-impregnated P25, Pt/TiO₂ (0.17 % Pt metal weight based and measured by inductively coupled plasma atomic emission spectroscopy), was prepared following the wet impregnation procedure. An aqueous precursor solution (H₂PtCl₄ 2.75 mL per g of titania support) was added to P25 and mixed in a mortar until a homogeneous slurry was obtained. The slurry was first dried at 363 K, crushed in a mortar, and finally calcined at 773 K in air for 3 h.

3.2.2 GAS-PHASE CONTINUOUS FLOW PHOTOCATALYTIC REACTION SETUP

The reaction setup is described in detail in *chapter 2*. Specifically for the studies presented in this chapter, 100 W high-pressure Hg lamp (Handy Cure HLR400T-1, *Senlight Corp.*) was used. The catalyst powder was diluted in quartz by crushing the powder and quartz wool in a mortar and later dispersed onto the bottom of the reactor by using a 250 μm mesh and sieving motion to improve the homogeneity of the catalyst. Photocatalytic activity per total amount of catalyst plus quartz (in total 500 mg) was at maximum at 20 wt% catalyst and thus this degree of catalyst dilution

was used throughout. The flow rate of CO₂ (> 99.9993 %, *Linde*) was regulated by means of MFC (*Bronkhorst*). The CO₂ flow passed through the water saturator maintained at 323 K and then through the reactor. After the reactor, the gas stream reached a water-cooled water trap and was transferred further to the analytical system. The transfer line where water vapor is present was heated at approximately 360 K by means of heating tapes. The gaseous products were analyzed by using the MS that allows fast sampling. The calibration gas was prepared by MFCs and its composition was 10 % H₂ (> 99.999 %, *Linde*), 10 % CH₄ (> 99.999 %, *Linde*), and 80 % Ar (> 99.999 %, *Linde*).

3.2.3 REACTION PROCEDURE

The catalyst was first pretreated with 4.5 mL·min⁻¹ of the reaction mixture of water-saturated CO₂(w-CO₂) for approximately 45 min at the reaction temperature. A pulsed calibration was performed, injecting 35 μL of the gas mixture every 7 min for several times to calibrate the MS signals for quantitative product analysis. After the calibration, the lamp was switched on and the evolution of reaction products was observed by MS. Mass-to-charge ratios (m/e) were chosen to avoid overlaps as much as possible and they are as follows: hydrogen (H₂: m/e = 2; HD: m/e = 3; D₂: m/e = 4), methane (CH₄: m/e = 15; CH₃D: m/e = 17). The reaction was terminated by switching off the lamp; another identical calibration was performed after the MS signals were stabilized to validate the quantification performed before the reaction. The catalytic testing and pretreatments were performed under different conditions using O₂ (> 99.999 %, *Linde*) or synthetic air (> 99.99 %, *Carbueros Metalicos*), D₂ (> 99.8 %, *Linde*), and D₂O (> 99.9 atom%, *Aldrich*) instead of Milli-Q H₂O, to study their influences on activation mechanism and catalytic activities. The reaction was performed at temperatures ranging from 338 to 423 K). These rather high reaction temperatures

were chosen to study the influence of temperature on the reactivity, as well as to avoid misinterpretation owed to the possible heating effects caused by the UV irradiation.

3.2.4 *IN SITU* DRIFTS

In situ DRIFTS measurements were performed by using the reaction chamber mounted in the Praying Mantis (*Harrick*) DRIFTS optical system (*chapter 2*). About 50 mg of Pt/TiO₂ was loaded in the sample holder of the chamber. The same gas supply system as for the reaction testing was used. Prior to the measurements, sample powders were first oxidized *in situ* at 423 K in 10 mL·min⁻¹ of O₂ under UV irradiation for 1 h. Subsequently, the catalyst was treated in water-saturated CO₂ (w-CO₂) flow for 2 h under dark conditions to stabilize the IR signal. The spectra were collected at 4 cm⁻¹ resolution. The DRIFT spectra were recorded approximately every 2 min to follow the evolution of surface species during UV irradiation and during the dark period.

3.3 OVERVIEW OF CATALYTIC ACTIVITY

In presence of active photocatalysts, the MS signal of the products sensibly responds after few minutes of irradiation. In the course of photocatalytic reactions, two distinct behaviours of catalytic activity, or their superposition, were typically observed; we refer to them as *transient activity* and *steady-state activity*. Transient activity is characterised by a steep increase of the signal, quickly reaching a maximum (10-15 min in gas phase setup), followed by a similarly steep decay, without turning off the irradiation. Steady-state activity is instead characterised by a milder profile change, where a plateau production is reached and sustained as long as the irradiation is present.

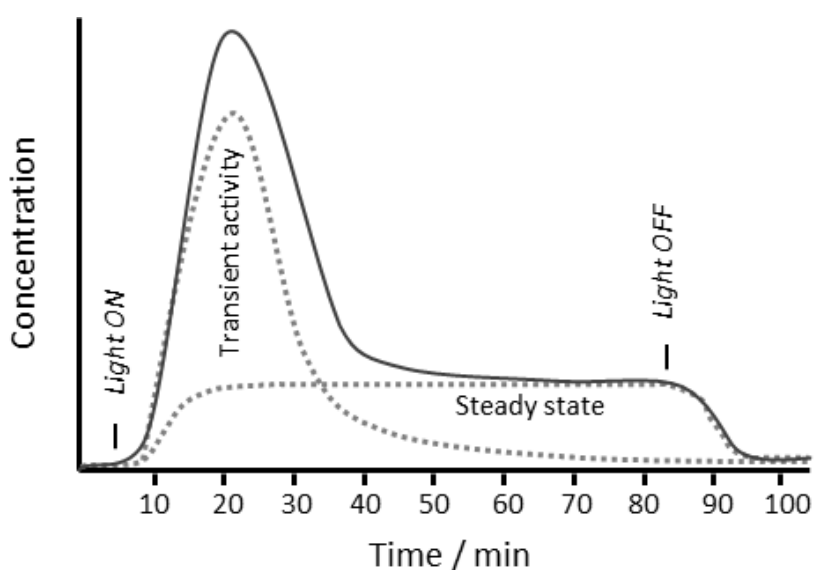


Figure 3-1. Pictorial representation of product concentration profiles observed in this work upon irradiation over an active photocatalyst in presence of $\text{CO}_2\text{-H}_2\text{O}$ mixtures. Dotted lines represent independent transient or steady-state activity, the solid their sum.

The two behaviours are not mutually exclusive and typically overlap as in the solid line in Figure 3-1. Indeed, they behave as two independent catalytic phenomena, possibly occurring at different surface sites or originating from different intermediates. Particular focus will be put on the distinction of the two features and their different properties.

The only gaseous reaction products detected and quantified with the MS setup were H_2 and CH_4 . Their detection limit was in the range of a few ppm of volumetric concentration. In the following sections a detailed description of the catalytic profile and performance of the TiO_2 -based catalysts will be presented.

Data are here presented implicitly but not strictly following the timeline of the research progresses, as the building of solid foundations required increasingly deep understanding of the system and its underlying mechanism.

3.4 GAS PHASE H₂O-SATURATED CO₂ PHOTOREDUCTION

3.4.1. ACTIVITY OF FRESH P25 AND WITH Pt CO-CATALYST

Platinum is an excellent co-catalyst, often reported in literature and coupled to photocatalysts to boost their hydrogen evolution capability. Coupling this metal with P25, probably the most celebrated titania material, has practically assumed the value of a benchmark in photocatalysis. In spite of great interest, the activity of this class of materials in a continuous flow, temperature controlled photoreactor is virtually unexplored to date. The activity of bare TiO₂ (P25) and Pt/TiO₂ (0.17 wt%) catalysts were therefore compared using the freshly synthesised samples, i.e. after thermal treatment in synthetic air at 773 K for 3 h.

Being the artificial photosynthesis reactions highly endothermic, a beneficial effect of temperature increase may be expected. Also elevating and regulating the reaction temperature may yield more reliable and consistent results because catalysts are often heated up under irradiation. In this work the reaction was investigated at different temperatures between 338 and 423 K. The lower temperature is limited by the lamp irradiation, causing a consistent radiative heating on the reactor, whereas the upper temperature is limited by the sealing element of the reactor (in this case silicone rubber). For the sake of simplicity of illustration, detailed catalytic results at 353 and 423 K are reported.

As summarised in Figure 3-2, both materials are active photocatalysts for H₂ and CH₄ production.

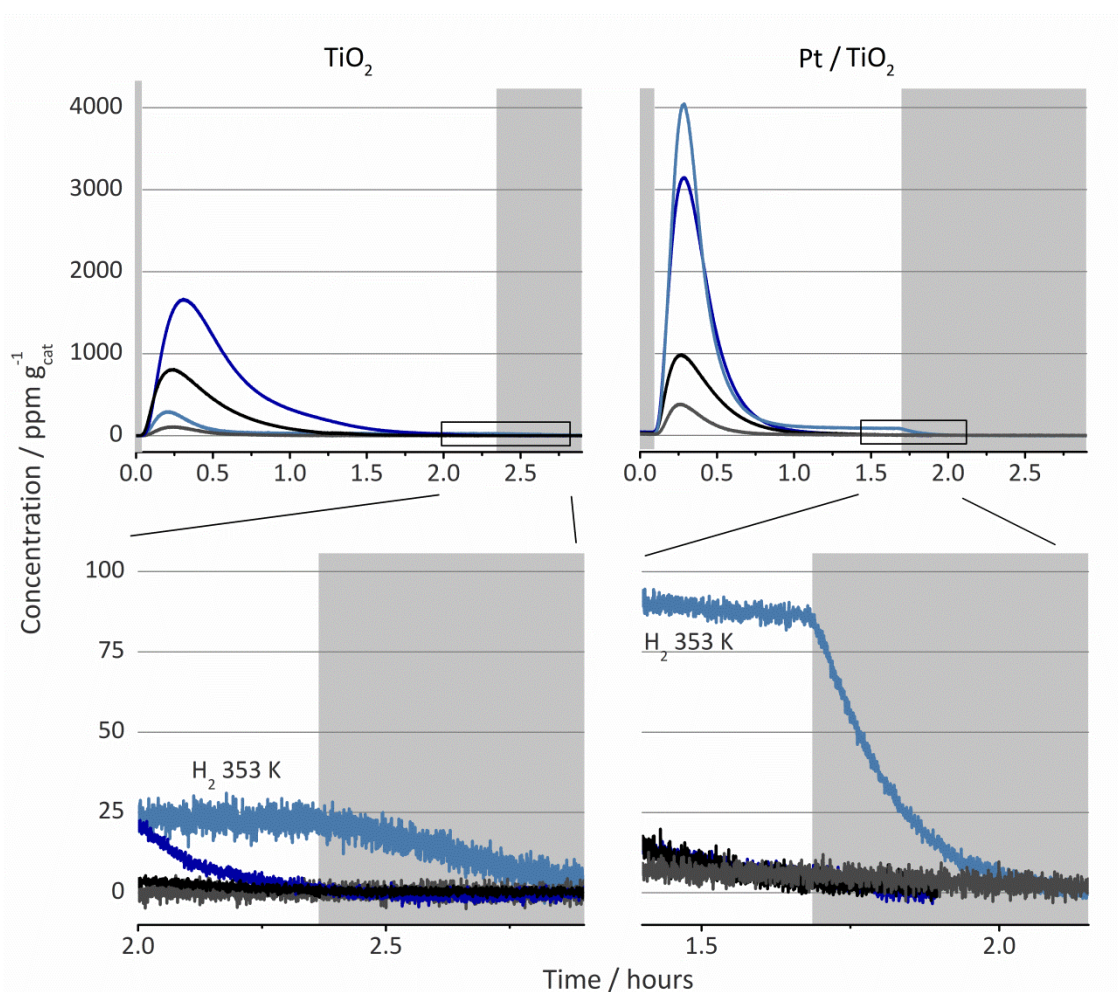


Figure 3-2. Concentration profiles of H₂ (light blue 353 K; dark blue 423 K) and CH₄ (grey 353 K; black 423 K) for bare TiO₂ and Pt/TiO₂ catalysts (top). In the panels below, the profile of steady-state hydrogen production is highlighted (353 K).

Transient activity is clearly dominant. All profiles show a steep increase up to a maximum concentration, reached in less than 20 min of irradiation, followed by an equally steep decay of production, i.e. a deactivation. Even though this transient activity is a common feature for all samples, the presence of following residual steady-state activity critically depends on the reaction temperature. At 423 K both materials are completely deactivated without the steady-state activity. On the contrary, at 353 K steady-state production of H₂ is still present as long as the sample is irradiated. Under the conditions and materials investigated, steady production of CH₄ was not observed.

Table 3-1. Productivity of bare TiO₂ and Pt/TiO₂. Marked (*) values refer to steady-state production of H₂, only occurring at 353 K (expressed in $\mu\text{mol}\cdot\text{g}^{-1}\cdot\text{h}^{-1}$). Integrated values of transient activities (calculated from the peak area of the concentration profile) are reported by subtracting the steady-state value (calculated over the actual integration time range) when present.

Catalyst	TiO ₂		Pt/TiO ₂	
	353	423	353	423
Temperature / K	353	423	353	423
H ₂ productivity / $\mu\text{mol}\cdot\text{g}^{-1}_{\text{cat}}$	0.9 0.25*	10.8	11.4 1.0*	10.6
CH ₄ productivity / $\mu\text{mol}\cdot\text{g}^{-1}_{\text{cat}}$	0.4	4.3	1.1	3.8

Combining the information summarised in Figure 3-2 and in Table 3-1, it is possible to compare the catalytic performance of the bare TiO₂ and Pt/TiO₂ catalysts. Most notably the presence of platinum co-catalyst positively affects hydrogen productivity. This effect is especially noticeable at low temperature (353 K), where H₂ transient activity increases more than tenfold, and for the steady-state level of the same product, the increase is more than three times. Also CH₄ transient production is more than doubled. Nevertheless, the positive Pt effect is completely cancelled at higher temperature, where even a slight productivity decrease is instead observed. Strikingly, and as opposed to bare TiO₂, the results is a higher H₂ transient productivity for the lower temperature run on Pt/TiO₂.

Despite the different activities, the two catalysts performed in a very similar way and it is natural to explain this by acknowledging TiO₂ as the core of the catalytic performance. Moreover, the catalytic rates are in good agreement with the literature data [3, 7, 8], which were in the vast majority of the cases collected based on batch reactor systems. As our results indicate the dominance of transient activity of both TiO₂ and Pt/TiO₂, the question could be raised whether literature batch data are

unknowingly characterised by the transient activity, i.e. the same catalyst deactivation, buried in the batch accumulation concentration profiles. Independent of the correct answer to this question, which could be certainly a matter of debate, this study clearly highlights the superior investigation potential offered by continuous flow photocatalytic reaction setups.

Another strong point of the continuous gas phase reactor is a finer temperature control in a relatively wide range. The experiments allowed recognising that, high temperature is not beneficial for hydrogen production as opposed to thermodynamic expectations. Analogous experiments performed at temperatures higher and lower than 373 K suggested that the boiling point of water is most likely the critical parameter playing a role in steady-state H₂ evolution. Below 373 K adsorption and condensation of water onto the catalyst surface is favoured and water can activate depleted catalytic sites. If this phenomenon occurs at a rate higher than H₂ evolution, the latter could be sustained in time and the steady-state activity is present. As far as transient activity is concerned, data are contrasting when investigating the temperature-activity relationship and a clear dependence on water condensation phenomenon cannot be outlined. Also catalytic tests at times suffered from unsatisfactory reproducibility, especially dealing with transient activity. Change in time and temperature of the reactor conditioning substantially affected the catalytic performance.

Reproducibility and the actual production of hydrogen and hydrocarbons using an artificial photosynthetic route is a still heavily criticised and debated topic in literature; the origin of the reduced products is still deeply questioned as it is difficult to state with certainty whether they are actually produced from CO₂ and the water fed to the system [9].

Several experiments were then performed to assess, at the best of the available possibilities, the origin of photocatalytic activity over Pt/TiO₂ and the parameters possibly affecting the low reproducibility [10]. Detailed description of the insights of such investigations will be given in the following sections.

3.4.2. EFFECT OF OXIDATIVE AND REDUCTIVE PRETREATMENTS

In the attempt to gain more solid understanding on the catalytic system and reproducibility, pretreatment procedures were investigated using Pt/TiO₂.

The effects of oxidation and reduction pretreatments were firstly investigated at 423 K. Three tests performed consist of the photocatalytic reactions with a) the fresh catalyst, b) after an oxidation treatment under the flow of synthetic air with UV irradiation, and c) after a reducing treatment in hydrogen flow under dark condition after the oxidation treatment (b). Photocatalytic performance after the three pretreatments is summarized in Figure 3-3.

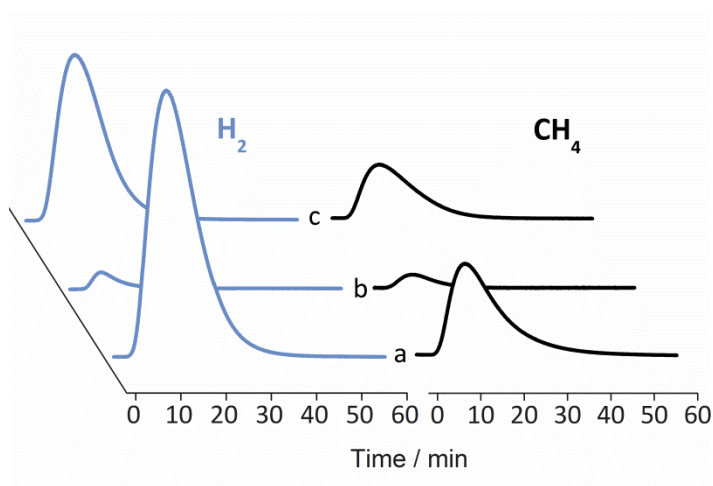


Figure 3-3. H₂ and CH₄ concentration profiles during the CO₂ photoreduction at 423 K for a) the fresh Pt/TiO₂ catalyst, b) after UV-oxidation pretreatment, and c) after subsequent reduction treatment in H₂ atmosphere. The concentrations are shown in MS counts.

As already shown in Figure 3-2, the fresh catalyst (a) completely lost its activity in both, CH₄ and H₂ production after ca. 1 h. TiO₂ is well known to be an excellent catalyst for mineralization of organic compounds to CO₂ and H₂O; therefore, the UV oxidation treatment (b) subsequently performed on the used catalyst guarantees the elimination of surface contaminants formed during the initial reaction, and also other residual organic compounds or carbon formed during the synthesis of P25 and platinum deposition. This oxidative pretreatment is expected to regenerate the catalytic sites if blocked by those surface contaminants. In contrast with our expectations, the catalytic test after the oxidative pretreatment displayed a much lower photoreduction activity. This might be explained by the low activity of the oxidized state of the catalyst. Such low catalytic activity was confirmed by the catalyst tested after the oxidative pretreatment without a preceding catalytic test (i.e., direct UV-oxidation pretreatment on the fresh catalyst). This excludes a possibility that the low activity after (b) is a result of the irreversible consumption of the “active sites/species” in the first run. The catalytic activity was recovered after the subsequent reduction treatment (c) to a similar extent to (a). Also a similar deactivation profile was observed after (c), indicating the importance of oxidation states or surface sites that are present in the fresh catalyst and can be regenerated by reducing treatment when the photocatalytic reaction takes place at 423 K.

3.4.3 REACTIVATION OF PHOTOCATALYTIC ACTIVITY UNDER DARK CONDITION

During the course of our investigation, we realized that the length of dark time (i.e., the UV lamp was switched off) under the flow of w-CO₂ after the reaction had a great influence on the catalytic performance of the subsequent photocatalytic run. The catalytic activity decreased after UV oxidation could be even regained (to the level of the fresh catalyst) after a very long period of dark time. Therefore, we systematically

studied the effects of the dark time length on the reactivation process and catalytic performance. For Pt/TiO₂ the length of dark time was varied from 1 up to 14.5 h with the reaction time of 60-100 min at 423 K until the steady state activity (i.e., inactivity at this temperature) was attained. The concentration profiles of CH₄ and H₂ are presented in Figure 3-4, where the periods of dark time were varied from 1, 1.5, 2.5, 4, and 6 h. We observed the ability of the catalyst to regenerate even in non-reducing conditions. UV irradiation after the dark period resulted in formation of the products the amounts of which increased proportionally with the length of the dark time (Figure 3-4), followed by a complete deactivation. Longer dark times resulted in more complete reactivation of the catalyst; the production levels were restored as compared to or even higher than that observed for the fresh sample with the dark period of 14.5 h (Figure 3-6).

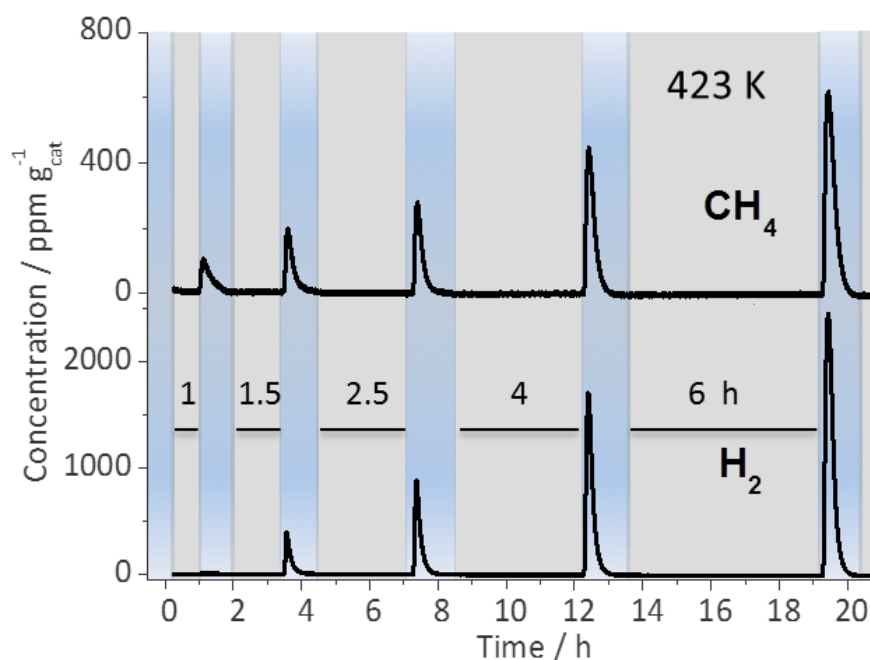


Figure 3-4. Concentration profiles of CH₄ and H₂ during the CO₂ photocatalytic reduction at 423 K with increasing dark time from 1 to 6 h (in gray).

The catalytic testing after the short dark period of 1 h produced mainly CH_4 , whereas the amount of H_2 increased more progressively as the dark time was increased (Figure 3-6). That indicates different active sites and/or precursors for CH_4 and H_2 production and their close relation to the reaction at the catalyst surface during the dark time.

Furthermore, an analogous experiment was performed at 353 K to study the effects of the dark-period length, particularly on the steady-state activity observed at the temperature (Figure 3-5). The mixed contributions of the transient and steady-state activity in H_2 production were separately estimated based on the H_2 production level just before terminating the irradiation as the steady-state activity by assuming it to be constant throughout the period of UV irradiation. Influences of dark-time length (1–19 h) were examined (Figure 3-5, up to 6 h is shown), and the catalytic performances after the respective dark periods were compared to that of the fresh catalyst (Figure 3-7).

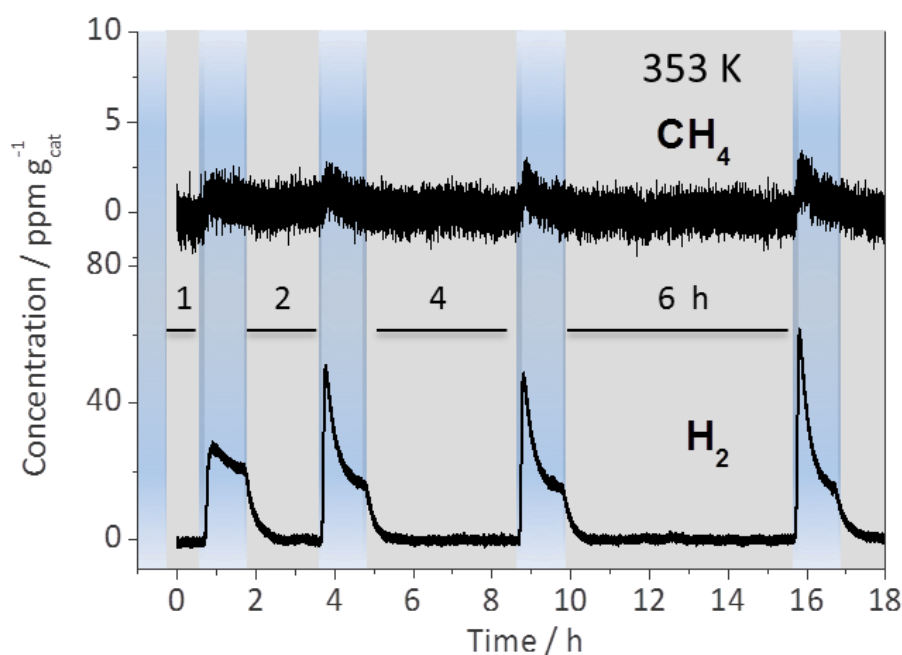


Figure 3-5. Concentration profiles of CH_4 and H_2 during the CO_2 photocatalytic reduction at 353 K with increasing dark time from 1 to 6 h (in blue).

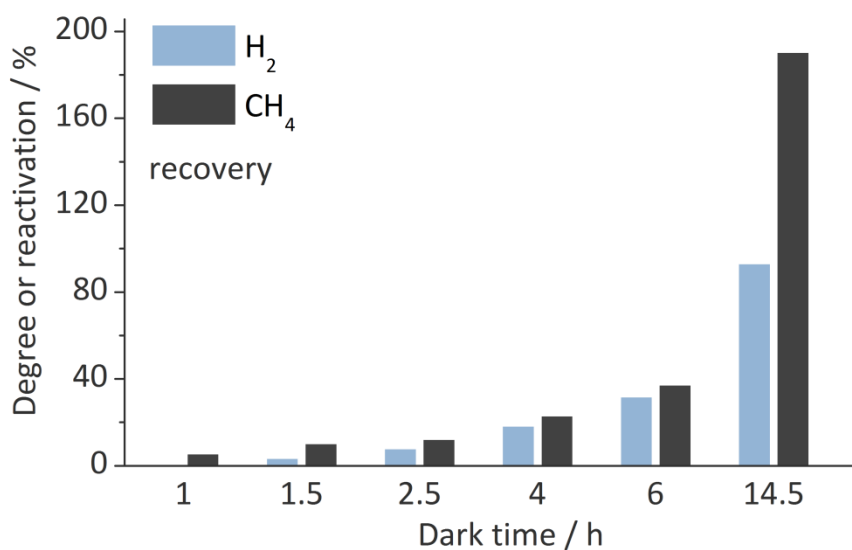


Figure 3-6. Photocatalytic activity for H₂ and CH₄ production at 423 K over Pt/TiO₂, after dark times of different lengths under the flow of w-CO₂. The degree of reactivation is referenced to the values obtained for the fresh catalyst.

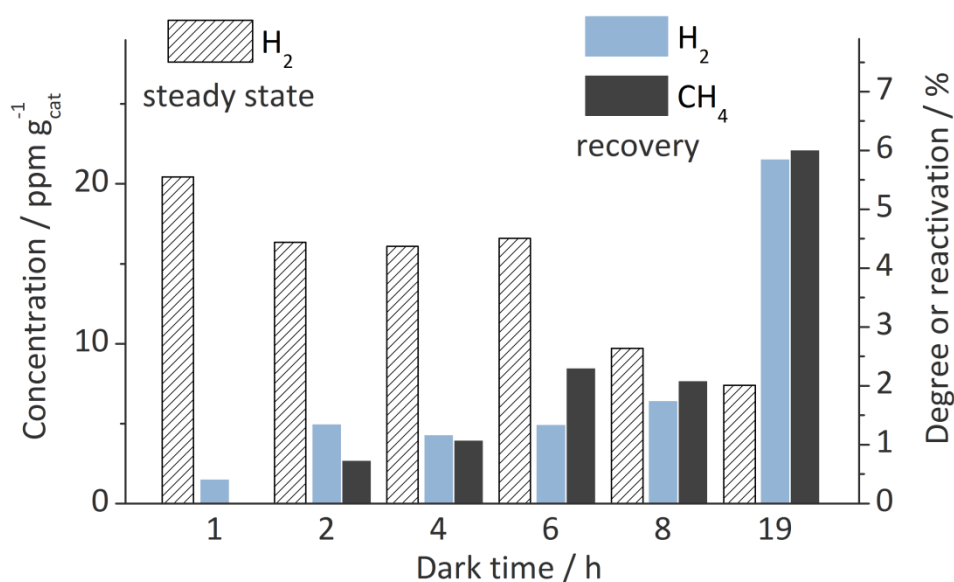


Figure 3-7. Photocatalytic activity for H₂ and CH₄ production at 353 K over Pt/TiO₂, after dark times of different lengths under the flow of w-CO₂. Degree of reactivation is referenced to the values obtained for the fresh catalyst (right y axis). The amount of steady-state hydrogen production is also shown at the corresponding dark-time length (left y axis).

At a first glance, a few differences from the experiment at 423 K can be recognized. After the short dark time (1 h) at 353 K, a negligible transient production of CH_4 was observed, whereas a steady-state production of H_2 with a very small transient profile was observed. The H_2 production stopped when the lamp was switched off. Increase of the dark time length resulted in an increase in the transient CH_4 production as observed at 423 K, but only slightly (Figure 3-5). Remarkably, the transient peak of the H_2 production becomes more prominent with a longer dark time and, as already stressed, apparently occurs independently from the steady-state formation of H_2 . We thereby confirmed that the H_2 concentration profile can be interpreted based on the sum of the steady-state activity and the transient activity. The increase of the dark-period length did not affect considerably the former (Figure 3-7), but did effectively affect the latter. There was an apparent decrease in the amount of steady-state H_2 production at increased lengths of dark time (Figure 3-7). This may be partially a result of true deactivation of the steady-state activity, but it can also be attributed to the systematic error in the way the activity was calculated (taking the last activity during the UV irradiation period as the steady-state activity). Nevertheless, it is clear that longer dark times do not positively affect the steady-state activity for H_2 production. Considering the results obtained at 423 and 353 K, the dark period in $w\text{-CO}_2$ recovers only the transient catalytic activity appearing in a peak and lasting for a limited time. The overall productivity of both CH_4 and H_2 at 353 K was consistently lower compared to that at 423 K as a result of the smaller transient catalytic activities. Notably, the overall activity for H_2 production was previously reported to be higher at 353 K when the fresh catalyst was evaluated (Figure 3-2). The state of the fresh catalyst and the state after reaction under UV irradiation should be clearly distinguished; the surface state of the catalyst with possible product precursors undergoes changes upon UV

irradiation and its recovery towards the initial surface state responsible for the transient activity occurs considerably faster at 423 K than at 353 K.

The dark time effects are also present for unpromoted TiO₂ and the results are also similar to what we have observed for Pt/TiO₂, but there are some differences. At 353 K the reactivation of CH₄ activity over bare TiO₂ is faster compared to the case of Pt/TiO₂. Nevertheless, at 423 K the situation is reversed; the transient activity for H₂ production was recovered more readily and prominently to that for CH₄ production.

Furthermore, the major difference induced by platinum is the accelerated reactivation process at 423 K as compared to bare TiO₂ (Figures 3-8 and 3-9). The presence of platinum seems to facilitate the formation of the product precursors under the dark condition or the creation of the surface sites or states, such as defects of TiO₂ under UV irradiation, thus accelerating the precursor formation under the subsequent dark condition.

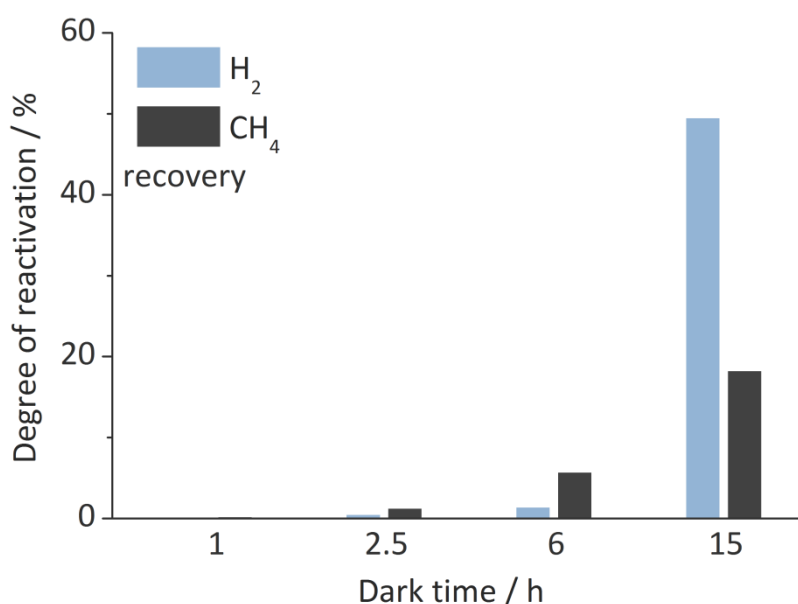


Figure 3-8. Photocatalytic activity for H₂ and CH₄ production at 423 K over bare TiO₂, after dark times of different lengths under the flow of w-CO₂. The degree of reactivation is referenced to the values obtained for the fresh catalyst.

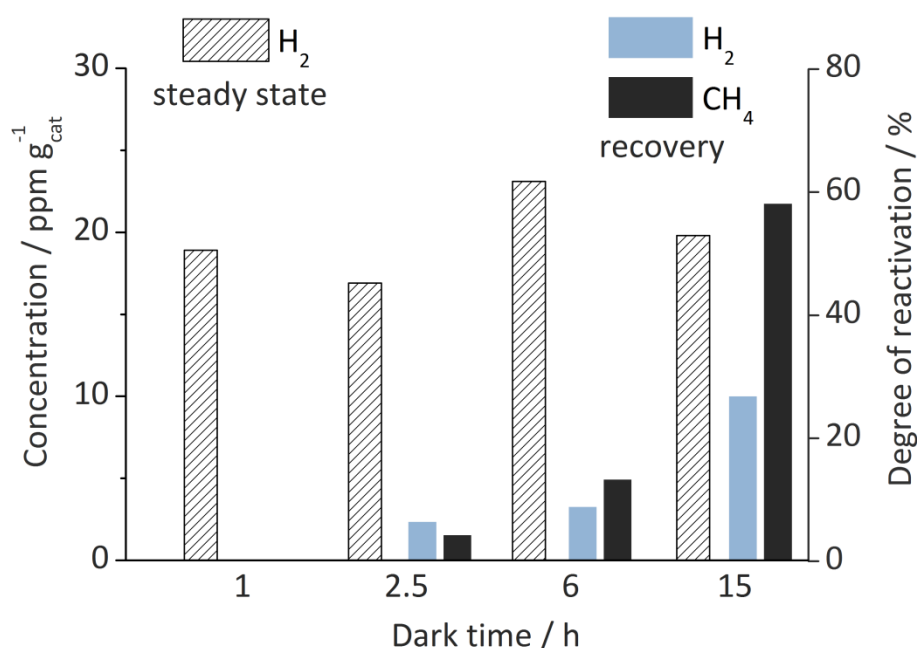


Figure 3-9. Photocatalytic activity for H₂ and CH₄ production at 353 K over bare TiO₂, after dark times of different lengths under the flow of w-CO₂. Degree of reactivation is referenced to the values obtained for the fresh catalyst (right y axis). The amount of steady-state hydrogen production is also shown at the corresponding dark-time length (left y axis).

3.4.4 ISOTOPIC STUDIES OF CATALYTIC ACTIVITY

To gain deeper insight into the active sites and reaction mechanisms involved, we performed CO₂ photoreduction with the w-CO₂ flow saturated with D₂O (dw-CO₂) over Pt/TiO₂ and different pretreatment conditions, which were UV oxidation in the air and subsequent reduction in H₂ or D₂. For the sake of clear separation of products based on m/e in MS, the evolutions of H₂, CH₄, D₂, HD, and CH₃D were studied. The temporal evolutions of the products for the following three cases, a) without pretreatment and b) D₂ and c) H₂ reduction pretreatment at 423 K after preceding UV-oxidation pretreatment, are presented in Figure 3-10.

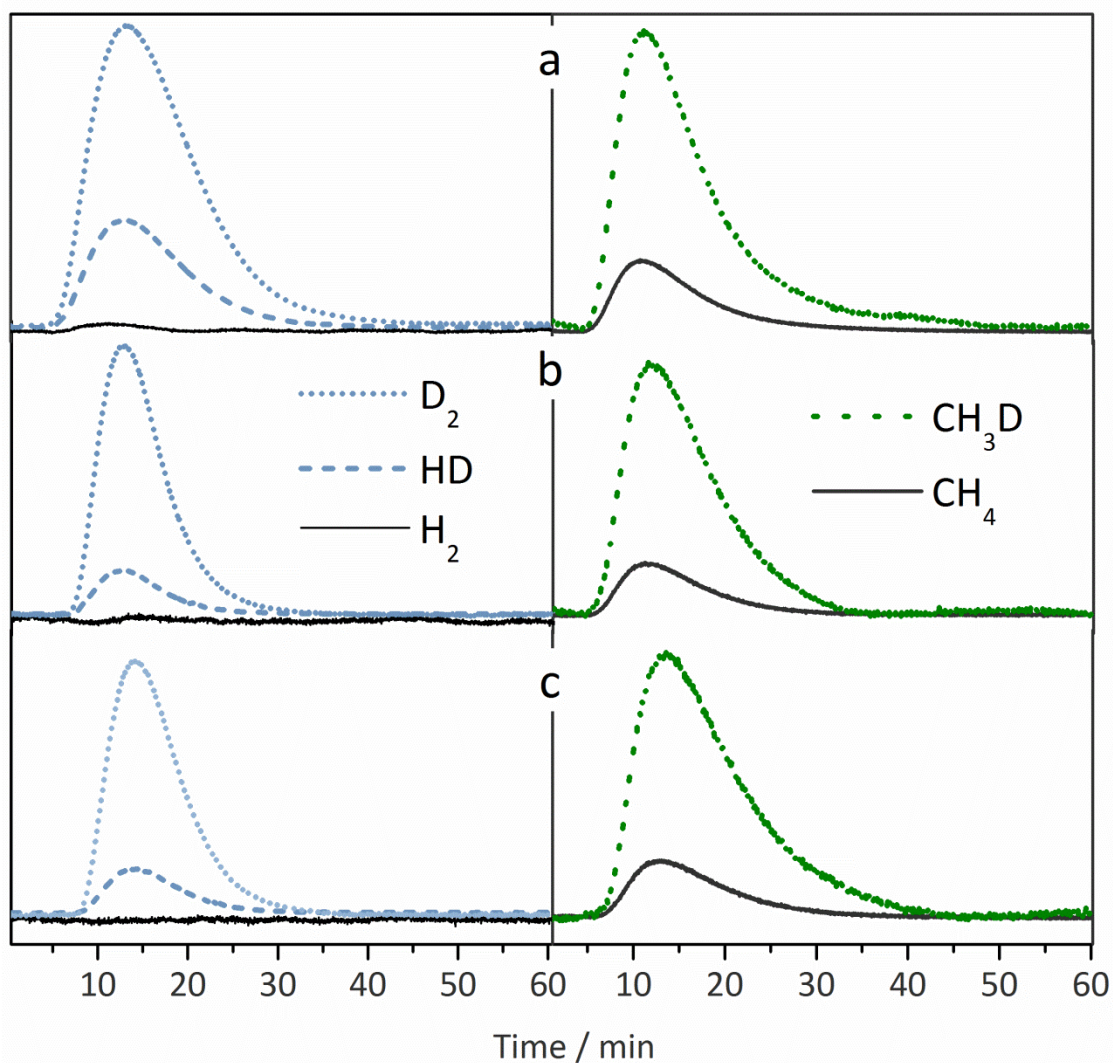


Figure 3-10. Concentration profiles of hydrogen and methane during the CO₂ photoreduction under dw-CO₂ flow at 423 K over a) the fresh catalyst, b) the catalyst first UV oxidized and then reduced by D₂, and c) the catalyst first UV oxidized and then reduced by H₂. The concentrations are shown in MS counts.

A mixture of deuterated and non-deuterated products was detected. In all three cases, a similar distribution of products was observed, except for a more prominent formation of hydrogen-containing products (H₂, HD, CH₄, and CH₃D) when the fresh catalyst was used (a). The similarity of profiles in (a), (b), and (c), particularly of the last two, clarifies that the source of the D-atom of the D-labeled products is D₂O in the dw-CO₂ flow rather than the hydrogen (D₂) used during the reduction pretreatment.

Nevertheless, it is important to point out a minor production of H_2 (only for the fresh catalyst) and CH_4 in all three cases examined, independent of the different pretreatments. This activity likely stems from the reaction of surface hydroxyl group naturally occurring on titania surface, implying slowness of the H-D exchange process of the hydroxyl group.

To understand the origin of the hydrogen atoms in hydrogen molecule produced in the transient and steady-state modes of catalytic function, a similar experiment with intermittent dark periods was performed at 353 K in dw- CO_2 . First, the catalyst was activated under a w- CO_2 flow for 15 h. Subsequently, the flow was switched to dw- CO_2 for the period necessary for MS signal stabilization (< 1 h) and the UV light was switched on. As evident from Figure 3-11, both HD and D_2 were visibly produced whereas H_2 was not detected (not shown). The concentration profiles display the transient activity and the steady-state activity described above. The major difference between the HD and D_2 profiles is the steeper decay of the transient activity for HD production.

The diminishing activity for HD production is more highlighted in the subsequent reaction (4–5 h), exhibiting the identical steady-state activity for D_2 production but a remarkable reduction in HD production. After a dark time of 14 h from this second reaction (at 19 h in Figure 3-11), the UV lamp was switched on. A steady-state activity for D_2 at the same level as that of the previous runs as well as an appreciable recovery of the transient activity was detected. On the other hand, only a very subtle but detectable transient activity and no steady-state activity were detected for HD.

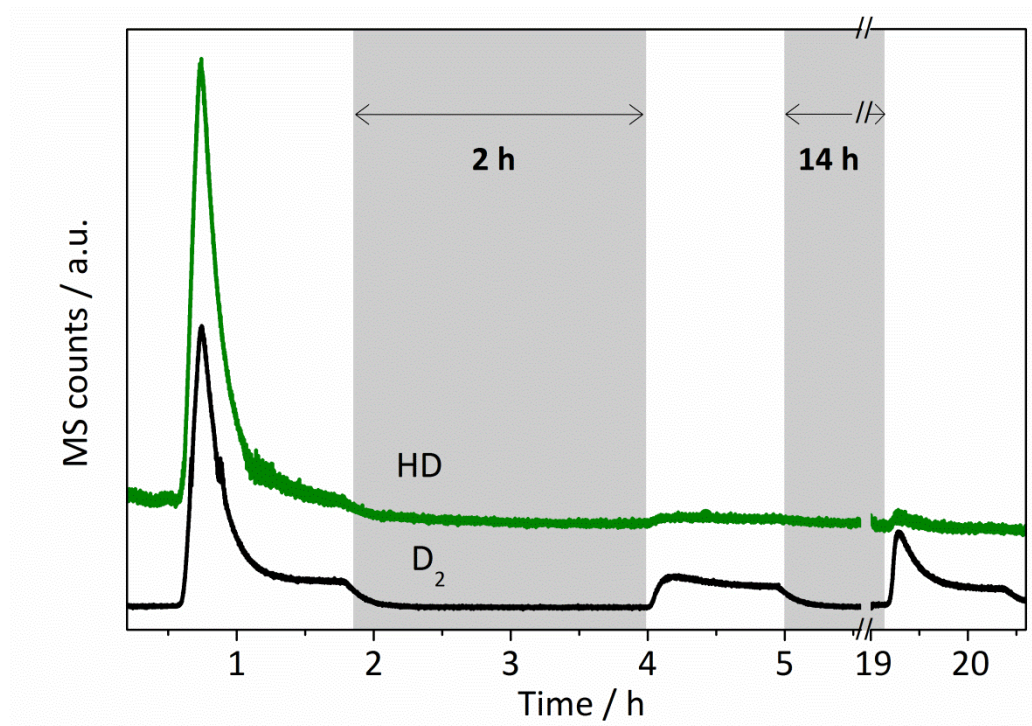


Figure 3-11. Hydrogen (HD and D₂) concentration profiles under UV irradiation and dark condition (in gray, 2 or 14 h) at 353 K. Initially, the catalyst was activated in w-CO₂ for 15 h (dark).

This study proves that the hydrogen atom is removed gradually with time during the photocatalytic reaction and replaced by deuterium atom. The exchange is a slow process as already suggested. These findings lead to a hypothesis of two distinct mechanisms responsible for H₂ production and of only one mechanism active for CH₄ production. One, responsible for the transient H₂ and CH₄ production, is strongly related to a slow process of regeneration of the active surface sites, probably involving dissociative adsorption of water, the formation of surface OH groups, and also a CH₄ precursor by CO₂ adsorption. The active hydrogen atoms generated by this slow process are available for reduction towards H₂ and CH₄ production under photoactivation. However, its regeneration does not occur at all or occurs to a negligible extent under UV irradiation, leading to quick deactivation of the catalyst and to the transient catalytic activity. The other process, responsible for steady-state H₂

production, depends on the concentration of surface H_2O , is independent of dark treatments, and does not appear to require a chemical activation process.

3.5 *IN SITU* DRIFTS CHARACTERIZATION

An *in situ* DRIFTS study was performed to shed light on the surface species involved in the reaction and the reactivation process under the dark condition (Figure 3-12). DRIFT spectra were continuously recorded during UV irradiation (1 h) and subsequent dark time (2 h). To confirm the band assignments, dw- CO_2 was also used instead of w- CO_2 . Comparison of spectrum a (light on) with spectrum b (light off) collected in w- CO_2 flow and the spectrum c (light on) with d (light off) collected in dw- CO_2 flow in Figure 3-12, clearly shows mirror images. This confirms that the same species are consumed and reversibly restored under UV irradiation and dark conditions, respectively. Isolated OH groups are formed on the TiO_2 surface during the photoreaction as evident from the increase of a characteristic O-H stretching band at 3678 cm^{-1} . As expected, this band is shifted to 2710 cm^{-1} of the hydroxyl (O-D) stretching mode in dw- CO_2 (Figure 3-12 c). Based on a previous report [11], this band may be assigned to radical titanol groups, $\text{Ti}^{\text{IV}}\text{OH}^{\bullet}$, which are long living charged species on the surface being consumed during the dark time and regenerated under UV irradiation. In the $1200\text{--}1800\text{ cm}^{-1}$ range, a number of negative bands at, for example, 1355, 1381, 1443, 1560, and 1641 cm^{-1} appear upon irradiation in w- CO_2 (Figure 3-12 a) and are restored during the dark time (Figure 3-12 b). Most of these bands do not virtually shift in dw- CO_2 ; therefore, they are assigned to surface carbonates [1381 and 1354 cm^{-1} for ν_{as} (OCO) bidentate carbonate, and 1560 cm^{-1} for ν (C=O) bidentate carbonate][9, 12].

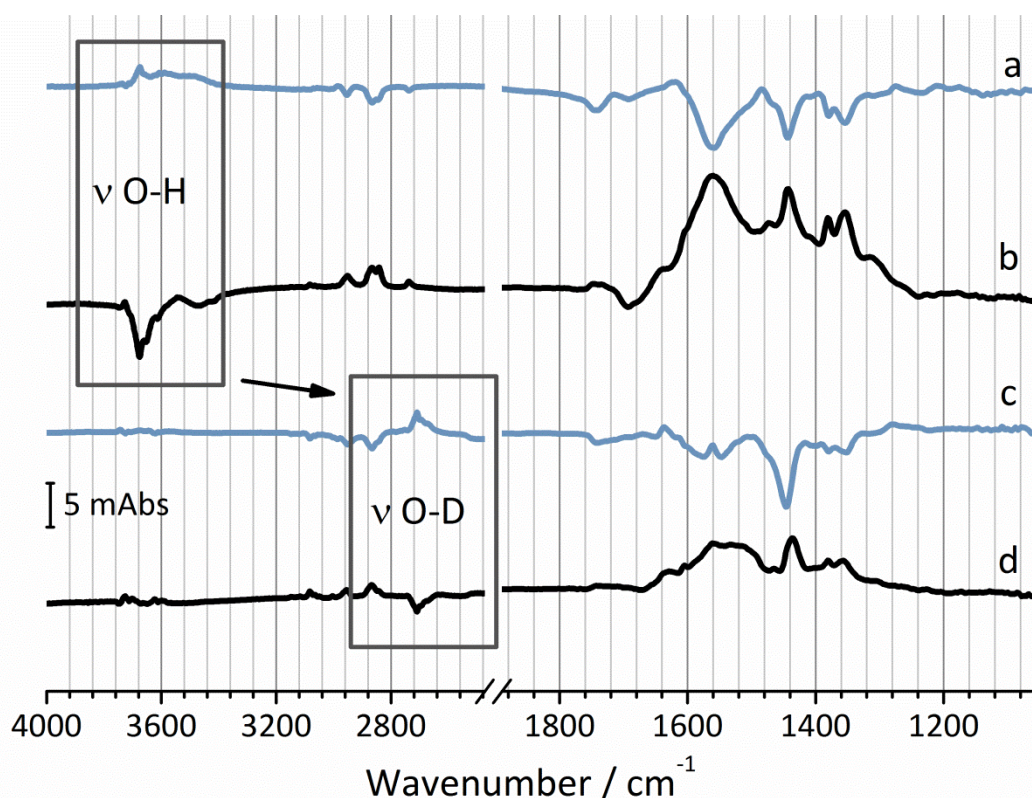


Figure 3-12. *In situ* DRIFT spectra of the catalyst when exposed to water saturated CO₂ at 423 K. The spectra were recorded after a) 1 h UV and b) subsequent 2 h dark recovery time in w-CO₂ flow and after c) 1 h UV and d) subsequent 2 h dark recovery time in dw-CO₂ flow. Spectra recorded under irradiation condition are in blue whereas the black ones were collected under the dark times.

A slight shift was observed for the strong band at 1443 cm⁻¹ and the shoulder at 1641 cm⁻¹ in w-CO₂ to 1629 and 1436 cm⁻¹ in dw-CO₂, respectively. These features were assigned to surface bicarbonate species [$\nu_s(\text{OCO})$][9, 13-15].

One may assign the bands in the typical C-H stretching region (2800-3000 cm⁻¹) observed in the spectra a and b in Figure 3-12 to be the precursor for CH₄. However, this cannot be the case because these bands are also present when C-H is replaced by C-D (spectra c and d, Figure 3-12). Therefore, these bands were assigned to overtone and combination bands of carbonate and bicarbonate bands appearing at 1300-1600 cm⁻¹. These findings highlight surface reactivity triggered by UV light, involving both

hydroxyl and carbonate/bicarbonate groups. Upon UV irradiation, the formation of new OH species, including radical groups, is suggested. At the same time, surface carbonates and bicarbonates, resulting from CO₂ adsorption in the activation dark period, are consumed and removed from the surface. This suggests a possible chemical interaction between activated OH groups and the adsorbed carbonate and bicarbonate species under UV irradiation. A picture of the complex mixture of these radical species, including OH groups and carbonates/bicarbonates, was recently illustrated in a detailed electron paramagnetic resonance (EPR) study of the photocatalytic reduction of liquid-phase CO₂ [16]. The effects of dark-time duration on the formation of surface sites and species were investigated by performing an experiment similar to the one presented in Figure 3-4. Prior to each dark-time length investigated (duration of 30, 100, and 180 min), the catalyst was treated under reaction conditions with UV irradiation for 1 h. As expected, the recovery of surface carbonate and bicarbonate species was more pronounced, proportionally to the length of the dark time, resulting in proportional consumption of these species upon subsequent UV irradiation (Figures 3-13 and 3-14). On the contrary, the band of the surface OH group did not vary with the dark-time lengths.

The *in situ* DRIFTS study clarifies that the activated surface OH groups of TiO₂ generated under UV irradiation reacts rather slowly with CO₂ to yield surface carbonates and bicarbonates. The amount of the surface species is determined by the length of the dark time the reaction mixture is exposed to. It is not clear from this study how these carbonates and bicarbonates are hydrogenated, but it evidently shows that these surface species formed under dark condition are the origin of the H₂ and CH₄ produced in a transient fashion.

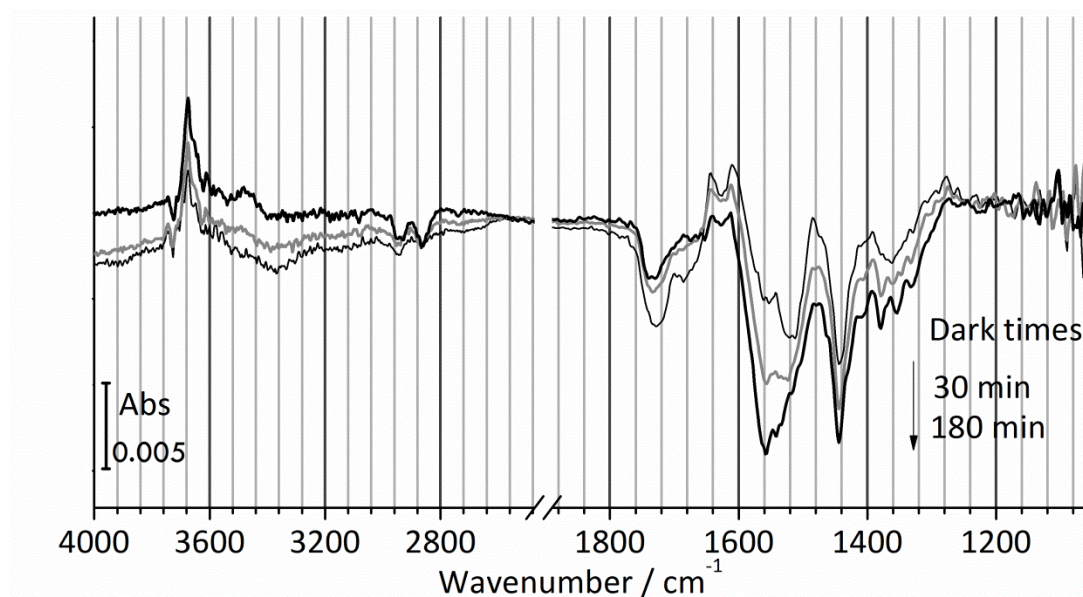


Figure 3-13. *In situ* DRIFT spectra of the catalyst when exposed to water saturated CO₂ at 423 K. The spectra were recorded after 1 h UV irradiation of the samples previously treated with increasing dark recovery times (30, 100 and 180 min). The absorbance spectra were calculated taking the first spectrum collected under the same irradiation or dark condition as the background.

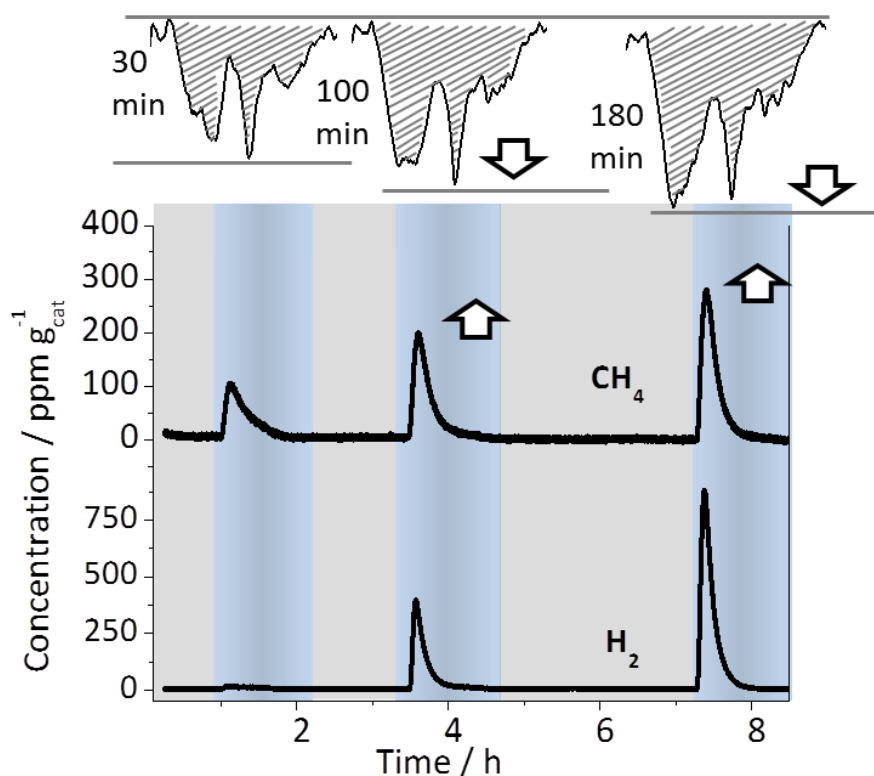


Figure 3-14. Correlation of the dark time recovery as observed during catalytic testing by MS (bottom) with the carbonate/bicarbonate consumption detected with *in situ* DRIFTS measurements (top).

3.6 CONCLUSIONS

The dynamic evolution of products during the continuous photocatalytic reduction of gaseous water-saturated CO_2 over Pt/TiO_2 was studied. Two major products, namely H_2 and CH_4 , have been detected and it was possible to differentiate two apparently independent reactivities: i) transient activity occurring at the initial phase of the reaction with a maximum activity (after 10–15 min) followed by rapid deactivation, and ii) steady-state activity only for H_2 below 373 K. Due to the better surface wetting, the water-splitting activity, both transient and steady-state ones, were enhanced below 373 K using the fresh catalyst. In contrast, the transient activity for CH_4 production was favoured at higher temperatures. These two different activities were also present for unpromoted TiO_2 and not specific to platinum-promoted TiO_2 . Oxidative and reductive pretreatment greatly influenced catalytic performance, and the reduction pretreatment was found important to create more reactive surface. Also, reactivation of the transient activity was elucidated by the dark time treatment in the reaction mixture. Longer recovery dark time and higher temperature were found to positively affect the reactivation of the transient activity.

BIBLIOGRAPHY

1. K. Nakata, A. Fujishima, *Journal of Photochemistry and Photobiology C: Photochemistry Reviews* **13**, 169, **2012**.
2. G. Liu, K. Wang, N. Hoivik, H. Jakobsen, *Solar Energy Materials and Solar Cells*, **24**, **2012**.
3. A. Dhakshinamoorthy, S. Navalon, A. Corma, H. Garcia, *Energy & Environmental Science* **5**, 9217, **2012**.
4. Y. Izumi, *Coordination Chemistry Reviews* **257**, 171, **2013**.
5. T.-V. Nguyen, J. C. S. Wu, *Applied Catalysis A: General* **335**, 112, **2008**.
6. C. Zhao, L. Liu, Q. Zhang, J. Wang, Y. Li, *Catalysis Science & Technology* **2**, 2558, **2012**.
7. G. Liu, N. Hoivik, K. Wang, H. Jakobsen, *Solar Energy Materials and Solar Cells* **105**, 53, **2012**.
8. V. P. Indrakanti, J. D. Kubicki, H. H. Schobert, *Energy & Environmental Science* **2**, 745, **2009**.
9. C.-C. Yang, Y.-H. Yu, B. van der Linden, J. C. S. Wu, G. Mul, *Journal of the American Chemical Society* **132**, 8398, **2010**.
10. A. Bazzo, A. Urakawa, *ChemSusChem* **6**, 2095, **2013**.
11. S. H. Szczepankiewicz, a. J. Colussi, M. R. Hoffmann, *The Journal of Physical Chemistry B* **104**, 9842, **2000**.
12. W. Su, J. Zhang, Z. Feng, T. Chen, P. Ying, C. Li, *The Journal of Physical Chemistry C* **112**, 7710, **2008**.
13. G. Martra, *Applied Catalysis A: General* **200**, 275, **2000**.
14. A. M. Turek, I. E. Wachs, E. DeCanio, *The Journal of Physical Chemistry* **96**, 5000, **1992**.
15. J. C. S. Wu, C.-W. Huang, *Frontiers of Chemical Engineering in China* **4**, 120, **2009**.
16. N. M. Dimitrijevic, B. K. Vijayan, O. G. Poluektov, T. Rajh, K. A. Gray, H. He, P. Zapol, *Journal of the American Chemical Society* **133**, 3964, **2011**.

CHAPTER 4

CATALYST TUNING

WITH Zn AND Rh-Cr

FOR OVERALL WATER SPLITTING

4.1 INTRODUCTION

During the last decade a new class of materials was brought to the attention of the scientific community, branching off from the research of Domen's group on photocatalytic water splitting.

Unprecedented high activity for overall water splitting in slurry batch conditions was achieved by Sakata et al. [1-3] using gallium oxide based materials as wide bandgap semiconductor photocatalyst. Doping with zinc ($2 < x < 6$ mol% w.r.t. gallium oxide) was found to be highly beneficial, resulting in a up to about one order of magnitude increase of water splitting activity (from few hundreds $\mu\text{mol}\cdot\text{g}^{-1}\cdot\text{h}^{-1}$ of hydrogen evolution of undoped catalysts). Activity was further enhanced by modifying the zinc-doped material with the previously reported nickel oxide or rhodium-chromium based co-catalysts [4]. The latter was effectively deposited on the catalyst by impregnation of a solution of the two metals followed by a mild heat treatment (1 h at 623 K in air). To the best of our knowledge these materials hold the highest reported overall water splitting activity at present, reaching 21 $\text{mmol}\cdot\text{g}^{-1}\cdot\text{h}^{-1}$ for H_2 and 10.5 $\text{mmol}\cdot\text{g}^{-1}\cdot\text{h}^{-1}$ for O_2 without sacrificial agents.

It was of high interest for our research line to test this class of materials in our continuous flow system (instead of the reported batch configuration) and to compare the slurry with the gas-phase reaction setup (*chapter 2*).

Photocatalytic activity of different combinations of dopant (Zn)/co-catalyst (Rh-Cr) on gallium oxide was examined. Slurry and then gas-phase reactor were used to confirm the reported trends and investigate the effect of the respective dopant/co-catalyst. Very similar trends were also found adopting the same modification steps on other promising catalysts such as Ta_2O_5 , MTaO_3 (tantalates), and TiO_2 , gaining new mechanistic insights into these classes of materials and modifications investigated.

4.2 EXPERIMENTAL SECTION

4.2.1 CATALYST PREPARATION

β -Ga₂O₃ (Sigma-Aldrich), β -Ta₂O₅ (Alfa-Aesar), and P25 titania (Degussa) were used as raw materials. The starting white powders were calcined at 773 K in air for 3 h prior to use. 2 wt% Zn (5.7 mol% w.r.t. Ga₂O₃) doping and Rh-Cr (0.5 and 0.75 wt% respectively) co-deposition on solid powders were performed by the wet impregnation procedure. An aqueous precursor solution (Zn(NO₃)₂·6H₂O or RhCl₃ + Cr(NO₃)₃·9H₂O; each 500 $\mu\text{l}\cdot\text{g}_{\text{cat}}^{-1}$) was added to the material and mixed in a glass container until a homogeneous slurry was obtained. The slurry was then homogenised by means of water bath ultrasonication cycles (3 min each), alternating with further mixing to optimize the homogeneity. The slurry was then dried at 363 K, crushed, and finally calcined at 1123 K for 6 h (Zn), or at 623 K for 1 h (Rh-Cr) under synthetic air flow (10 ml/min). K promoted catalysts (5 wt% K based) were prepared by impregnation with K₂CO₃ aqueous solutions (500 $\mu\text{l}\cdot\text{g}_{\text{cat}}^{-1}$), followed by mild calcination at 623 K for 1 h.

NaTaO₃ materials with different doping were synthesized by thermal [5-7], urea combustion [8], molten salt [9], and hydrothermal [10] techniques.

La-doped (2 mol%) NaTaO₃ materials were synthesized via thermal method. Ta₂O₅, Na₂CO₃ (molar ratio 1 : 1.2, to account for Na evaporation) and La₂O₃ were crushed together then ball milled for better intermixing. The mixture was then heated at temperature up to 1373 K for 10 h. For better result, the heat treatment was also suspended at 1073 K to perform extra mixing/crushing of the powders.

Urea combustion NaTaO₃ samples were prepared from Ta₂O₅, Na₂CO₃, and CO(NH₃)₂ (molar ratio 1 : 1 : 4), mixed in a thick water slurry, dried at 353 K and crushed in a

mortar. The urea blended precursors were then slowly heated (2 K/min) up to 573 K and subsequently brought to 873 K (5 K/min, 4 h).

$K_{0.4}Na_{0.6}TaO_3$ samples were prepared by eutectic molten salt technique. Ta_2O_5 , Na_2CO_3 and K_2CO_3 were mixed at the molar ratio of 1 : 0.6 : 0.4 and added to a NaCl/KCl mixture (molar ratio 0.8 : 1) of comparable total weight as the Ta_2O_5 precursor used. The mixture was crushed in a mortar and heated up at 1023 K (5 K/min, 2 h), then washed with water, filtered and dried at 353 K.

Hydrothermal N-doped $NaTaO_3$ nanocubes were prepared in a Teflon lined autoclave. A Ta_2O_5 , NaOH and NH_4OH (molar ratio 1 : 33 : 7.5) solution-suspension in water was prepared and heated at 453 K for 12 h under hydrothermal conditions. The solid product was then washed by centrifugation and dried at 353 K.

4.2.2 CONTINUOUS FLOW PHOTOCATALYTIC REACTION SETUP

The same reaction setup described in *chapter 2* and *section 3.2.2* was used for the catalytic testing. As an extra heat controlling device, a steel heat sink platform coupled to a water bath was used when studying the reaction at 323 K.

Alternatively to the gas phase reactor, also the slurry reactor described in *chapter 2* was used. Previous to reaction, the catalyst (0.02 g) was homogeneously dispersed in 35 ml of Milli-Q water in the quartz tube by means of ultrasonication, and the slurry was constantly stirred with a magnetic stirrer after coupling with the glass head.

The gaseous products were analysed by MS (*Pfeiffer Omnistar*). Calibration of MS curves was performed by an on-line micro GC (*Agilent*), injecting few samples at different times during the catalytic run for normalization reference in data post-treatment. The light source was a 400 W high-pressure Hg lamp (*UV-technik*), regulated to a source power of 200 W by means of a dimmable electronic ballast (*Solux*).

4.2.3 REACTION PROCEDURE

The catalyst was first pretreated under $4.5 \text{ ml}\cdot\text{min}^{-1}$ of the reaction mixture of water-saturated CO_2 ($w\text{-CO}_2$) for approximately 45 min at the reaction temperature. At MS signal stabilisation, the lamp was switched on and the evolution of reaction products was followed by MS. Mass-to-charge ratios (m/e) were chosen to avoid overlaps as much as possible and they are as follows: hydrogen (H_2 : $m/e = 2$), methane (CH_4 : $m/e = 15$), oxygen (O_2 : $m/e = 32$). The reaction was terminated by switching off the lamp. The reaction was tested at temperatures ranging from 332 to 423 K in the gas phase reactor (measured in the reactor body). In the slurry reactor the reaction was studied at approximately 338 K, which was the equilibrium temperature upon irradiation (measured averaging the extreme temperatures at the irradiation surface of the reactor and at the surface opposite to it). Typically, a UVFS window (6 mm thickness) was used as light source filter, buffering the high heat delivered by the lamp which would cause excessive evaporation from the slurry. Alternatively, also BK7 (*Eksma optics*) and FGUVS11 (*Thorlabs*) were used to study the effect of excitation wavelength on the catalytic activity.

4.3 WATER SPLITTING PHOTOCATALYSTS AND MODIFICATION

SERIES WITH Zn AND Rh/Cr: SLURRY REACTOR

4.3.1 GALLIUM OXIDE BASED MATERIAL: REACTIVITY FEATURES

Gallium oxide is a wide bandgap semiconductor ($E_g \approx 4.4 - 4.9 \text{ eV}$) [11]. As such, its conducting and valence bands are consistently spread apart and located at absolute energy well over the required thermodynamic limit for both water reduction and oxidation.

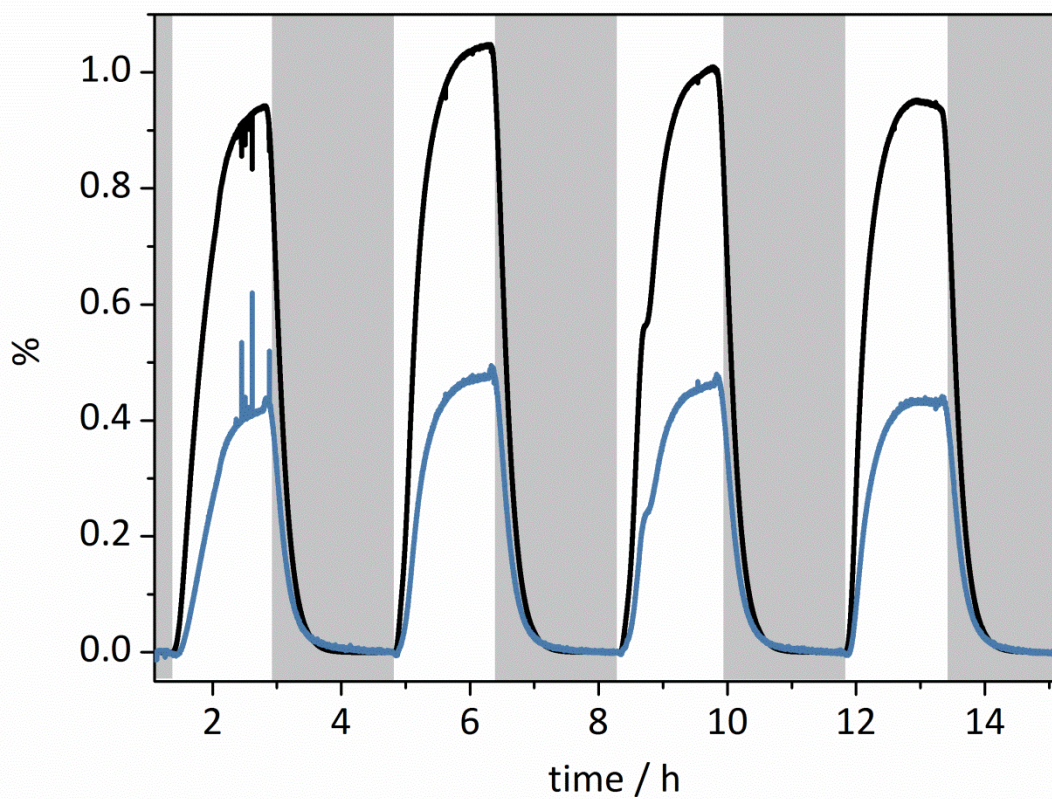


Figure 4-1. H₂ (black) and O₂ (blue) concentration profiles under UV irradiation over Ga₂O₃Zn/Rh-Cr catalyst in the continuous flow slurry reactor. Shaded parts correspond to dark time; unshaded one to irradiation period. Oxygen baseline value was subtracted. The spikes in the profiles are due to GC sampling for concentration calibration.

The drawback of such a wide bandgap lies in the fact that, according to the Bard's model for semiconductor photocatalysis [12], we are bound to excite the catalyst with highly energetic short wavelength UV light ($\lambda < 280$ nm). This represents only a little fraction of the power delivered by common high pressure Hg lamps.

Figure 4-1 shows the concentration profiles of hydrogen and oxygen evolved from a Ga₂O₃Zn/Rh-Cr slurry, when illuminated in continuous flow mode; four irradiation (1.5 h)-dark (2h) cycles were performed. Despite the relatively low effective power available, the overall water splitting in pure water is immediately and consistently

triggered by switching on the light source. High concentration of gaseous hydrogen (up to over 1 %) and oxygen in close to 2 : 1 ratio can be achieved, slowly stabilizing to a steady state under irradiation. Water splitting activity is reproducible upon subsequent dark-irradiation cycles.

4.3.2 GALLIUM OXIDE MODIFICATION SERIES

Gallium oxide based materials were studied using a modular approach to unravel how the single promoter (dopant/co-catalyst) affects the photocatalytic activity. More precisely three different materials were prepared modifying a commercial Ga_2O_3 powder (0) as follows

- 0- Commercial Ga_2O_3 , calcined at 773 K
- 1- Zn (2 wt%) impregnation, calcination at 1123 K for 6 h (doping)
- 2- Rh (0.5 wt%) - Cr (0.75 wt%) co-impregnation, calcination at 623 K 1 h (co-catalyst deposition)
- 1+2- Zn (2 wt%) / Rh (0.5 wt%) - Cr (0.75 wt%) following steps 1 and 2 consecutively (doping and co-catalyst deposition).

The effect of zinc and rhodium-chromium doping/deposition on gallium oxide crystal structure was observed by X-ray diffraction, as shown in Figure 4-2.

Gallium oxide sample used as starting material could be identified as monoclinic β - Ga_2O_3 [13]. Upon Zn doping the main crystal structure remained unchanged, with the exception of three features at $2\theta = 29.0, 35.7,$ and 63.2° respectively (Figure 4-2, * symbol). The $2\theta = 35.7^\circ$ diffraction peak was previously assigned by Y. Sakata et Al. [2] to the more intense feature in the ZnGa_2O_4 diffraction pattern, i.e. the $\text{ZnO}/\text{Ga}_2\text{O}_3$ mixed oxide. This is a key signature of the incorporation of zinc into the structure of gallium oxide.

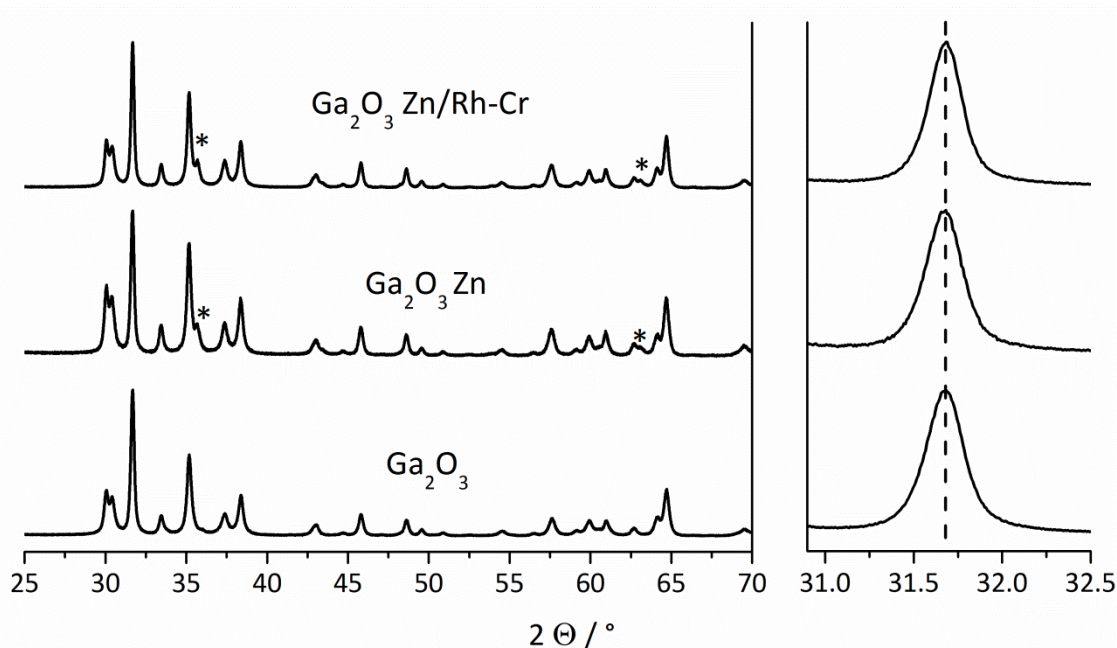


Figure 4-2. XRD pattern of Ga₂O₃, as starting material and after Zn and Zn/Rh-Cr modifications. On the right, the magnification of $\theta = 31.7^\circ$ (202) diffraction peak.

Another expected signature, according to the same reference, is the shift of (202) plane diffraction peak ($2\theta = 31.7^\circ$) to lower angles, in response of the substitution of some Ga³⁺ ions (0.060 nm) with bigger Zn²⁺ ions (0.069 nm). This shift did not noticeably occur in our samples (right plot in Figure 4-2). No effect of Rh-Cr impregnation was visible in the XRD patterns, which retained the same structural characteristics as the previous material only doped with Zn. This is consistent with low metal loading and low temperature treatment, which were not expected to drive any further phase transformation.

4.3.3 GALLIUM OXIDE MODIFICATION SERIES: SLURRY ACTIVITY

The four prepared materials were tested in the continuous flow slurry reactor where product formation was followed by GC and MS.

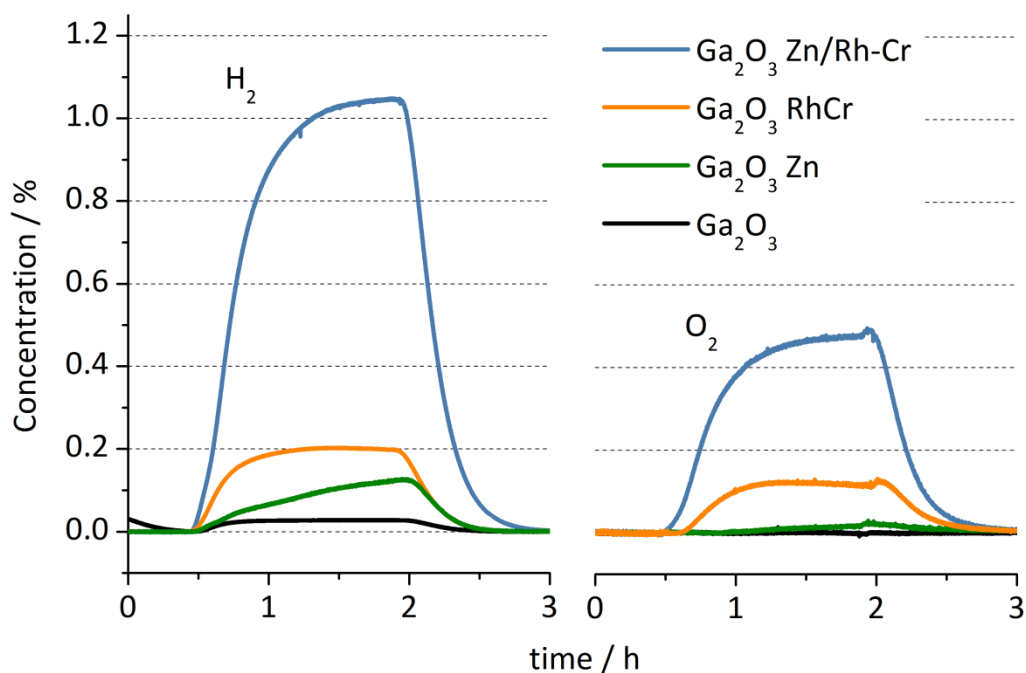


Figure 4-3. H₂ and O₂ concentration profiles under 1.5 h UV irradiation (ON at \approx 0.5 h, OFF at \approx 2 h) in the continuous flow slurry reactor for the different catalysts of the Ga₂O₃ Zn/Rh-Cr series.

As Figure 4-3 clearly shows, the doping and co-catalyst deposition drastically improved the photocatalytic performance of gallium oxide. Its base activity for hydrogen production (generating ca. 220 ppm H₂ under steady state condition in the continuous gas stream) could be enhanced by a factor of 7 by Zn doping and by 9 times with Rh-Cr co-catalyst deposition. Even more interestingly, an approximately 50 times activity increase was observed for the final Zn/Rh-Cr catalyst (Figure 4-4). This suggests a strong synergetic effect between the doping and the co-catalytic components, which cannot be explained by simple additive combination of the two contributions.

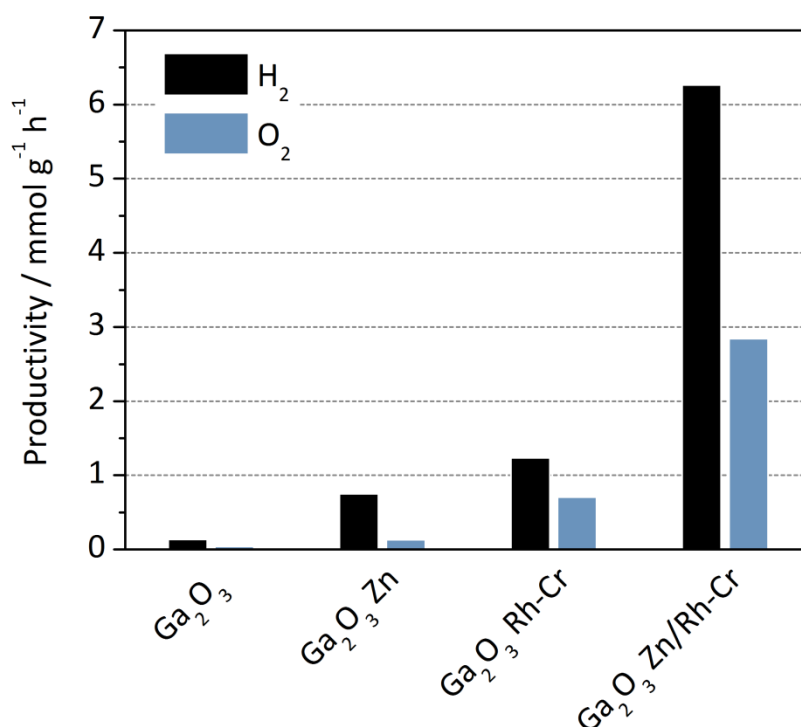


Figure 4-4. Comparison of H₂ and O₂ steady state productivity of the Ga₂O₃ based catalysts.

The activity here reported are in good agreement with the results reported for Sakata's commercial Ga₂O₃ samples modification series [1] (ca. 50 % of the reported batch reactor activity for Zn/Rh-Cr modified sample) with the exception of the reduction of oxygen evolution (very close to the detection limit as shown in Table 4-1) from bare Ga₂O₃ and Ga₂O₃ Zn samples. Contrarily to what reported in literature, our data suggests that the Rh-Cr loaded catalysts are the only capable of continuous stoichiometric oxygen evolution, i.e. sustaining overall water splitting. In all cases, production of CO₂ reduction products (e.g. CO, CH₄) was not observed.

4.3.4 TANTALUM AND TITANIUM OXIDES MODIFICATION SERIES: SLURRY ACTIVITY

The modular approach of doping/co-catalyst modification was expanded to other classes of promising semiconducting oxide photocatalysts, in order to investigate its

efficacy. Titanium oxide (TiO_2 , P25) was chosen as a second reference material because of the widely reported activity and the previous available experience. As third subject of comparison tantalum oxide (Ta_2O_5) was selected, as high photocatalytic water splitting activity was already reported in presence of a suitable co-catalyst (e.g. NiO, Ru_2O , Rh/Cr) [14-17]. Both titanium and tantalum oxides could produce hydrogen upon UV irradiation in presence of water. On the contrary, oxygen evolution was never observed during our catalytic testing using the bare catalysts. Strikingly, residual oxygen concentration was observed to drop (example in Figure 4-5) in the continuous flow stream of reacting gas.

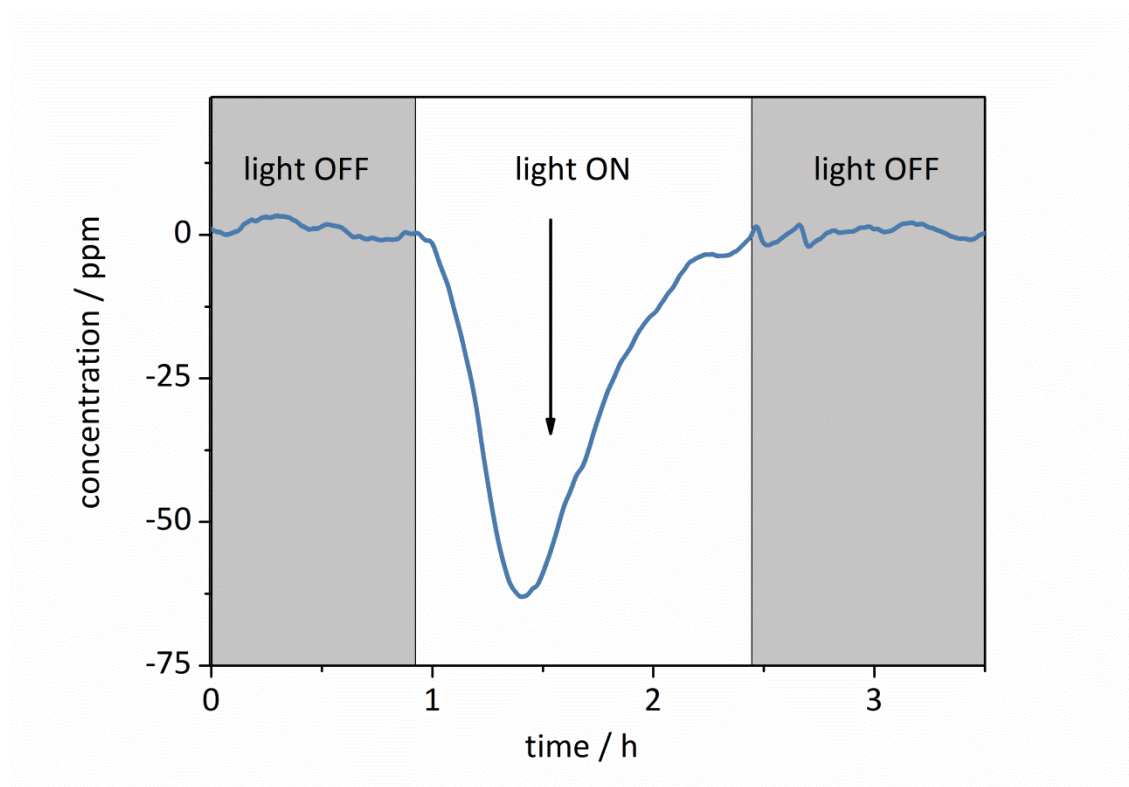


Figure 4-5. Residual oxygen consumption using Ta_2O_5 catalyst and upon irradiation. Baseline oxygen concentration has been subtracted to show only the reaction contribution.

The drop is usually mostly transient, and typically oxygen level is restored to base level before irradiation interruption. Overall water splitting reaction pattern is not

closed under such conditions and some alternative paths for oxygen reactivity might be therefore present. On the one hand, it is possible that, instead of molecular oxygen, a variety of radical or intermediate oxidation state oxygen species might be forming from O^{2-} ions generated, during water reduction. On the other hand O_2 also seems to actively react, counteracting any possible oxygen evolution. The bare (0), Zn doped (1), RhCr deposited (2), and Zn/RhCr doped/deposited (1+2) Ta_2O_5 and TiO_2 materials were prepared and tested in analogous conditions as described in the previous section about Ga_2O_3 based materials. The steady state productivity levels are displayed in Figure 4-6 and Table 4-1.

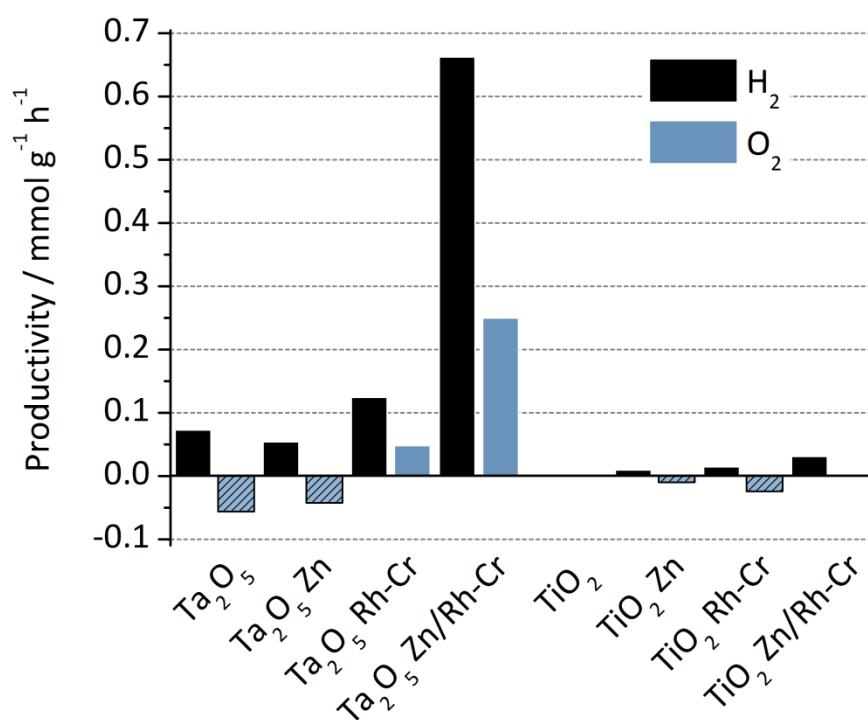


Figure 4-6. Comparison of H_2 and O_2 steady state productivity observed for Ta_2O_5 and TiO_2 based catalysts. Dashed bars represent negative productivity for oxygen: these values were calculated from the value of maximum dip of oxygen concentration upon irradiation. These values should be taken as a semi-quantitative indication of the oxygen consumption, which appears to be a transient phenomenon and not a steady one.

At a first glance, it is clear how both Rh-Cr and Zn/Rh-Cr deposition consistently enhance hydrogen productivity in a very similar fashion as observed for Ga₂O₃ series. Moreover, upon Rh-Cr modification the sign of the mentioned negative oxygen productivity is reversed, confirming even more strongly the boosting of oxygen evolution observed for gallium oxide series. The addition of Rh-Cr clearly blocks the oxygen consumption and triggers its production.

Table 4-1. H₂ and O₂ productivity (mmol·g⁻¹·h⁻¹) values for the Ga, Ta, Ti oxides modification series; summarising data displayed graphically in Figures 4-4 and 4-6.

Catalyst	H ₂	O ₂
Ga ₂ O ₃	0.13	0.04
Ga ₂ O ₃ Zn	0.75	0.13
Ga ₂ O ₃ Rh/Cr	1.23	0.70
Ga ₂ O ₃ Zn-Rh/Cr	6.27	2.84
Ta ₂ O ₅	0.07	-0.06
Ta ₂ O ₅ Zn	0.05	-0.04
Ta ₂ O ₅ Rh/Cr	0.12	0.05
Ta ₂ O ₅ Zn-Rh/Cr	0.66	0.25
TiO ₂	traces	0.00
TiO ₂ Zn	0.01	-0.01
TiO ₂ Rh/Cr	0.01	-0.02
TiO ₂ Zn-Rh/Cr	0.03	0.00

Still this data do not explain clearly how Rh-Cr allows this reactivity change. Indeed, its action might be either triggered by (i) the blockage of the catalytic sites responsible for O₂ consumption (reverse reaction) or (ii) generation of new OER sites, producing oxygen at much higher rate than the recombination sites consume it. The fact that

oxygen production appears to be sub-stoichiometric on tantalum oxide samples ($H_2 : O_2 \approx 3 : 1$) would support more strongly the second hypothesis.

The strong activity boosting by Zn-Rh/Cr combination is again observed for Ta_2O_5 series, whereas in case of TiO_2 series the boosting level appears to be more close to a simple additive combination of Zn and Rh/Cr effects. Among the Ta_2O_3 series the best catalyst yields approximately 10 % of the activity observed for Ga_2O_3 Zn/Rh-Cr catalyst, whereas the best catalyst of the TiO_2 series displays a significantly lower activity, about 250 times less than Ga_2O_3 Zn/Rh-Cr (Table 4-1).

4.3.5 EFFECT OF EXCITATION WAVELENGTH

A UVFS window was normally used to filter incident light from the Hg lamp during reaction testing. This material is transparent to the required short wavelength UV light, but was used as temperature buffer to reduce the reactor temperature to a maximum level of 348 K and limit the evaporation of water of the slurry.

In order to evaluate the excitation wavelength dependence of the catalysis on their photocatalytic activity, we performed catalytic tests with different optical filters (*chapter 2*). We used a borosilicate window (BK7), cutting off completely light with $\lambda < 300$ nm, and a FGUV11S window (bandpass $275 < \lambda < 375$ nm), as substitute to the UVFS. The window change was performed without interrupting the irradiation.

The filter effects on the activity of Ga_2O_3 Zn/Rh-Cr catalyst are shown in Figure 4-7a. Upon changing to the BK7 window the activity was suppressed. The same behaviour was sustained by subsequent switch to the FGUV11S black filter. The high level of activity was restored reverting to the starting configuration with the UVFS filter ($t > 3.7$ h).

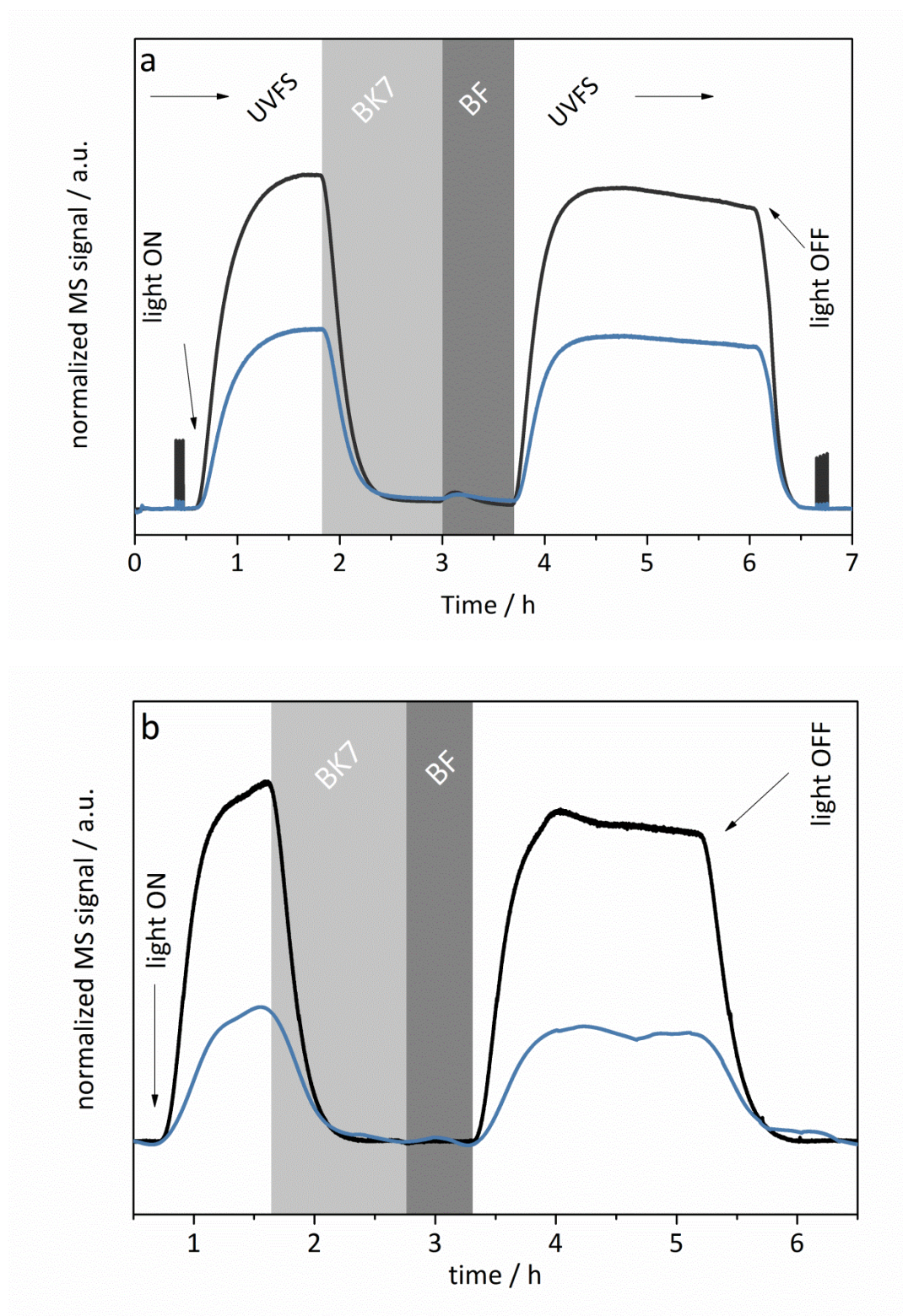


Figure 4-7. H₂ (black) and O₂ (blue) concentration profiles under UV irradiation in the continuous flow slurry reactor. Three different filters were used to highlight their influence on the reaction: UV grade fused silica (UVFS), optical borosilicate (BK7, light grey highlight), and a FGUV11S black filter (BF, deep grey highlight). Catalysts: a) Ga₂O₃ Zn/Rh-Cr, b) Ta₂O₅ Zn/Rh-Cr.

These findings are in full agreement with the semiconductor photocatalyst model as the only filter material allowing irradiation at a wavelength of approximately 250 nm is fused silica (UVFS). The other two filters only allow a small fraction of photocatalytic energetic wavelength to hit the catalyst, completely suppressing the reaction (the small increase in activity using BF (Figure 4-7a) was likely caused by a little UV irradiation during the filter change).

Ta₂O₅ has a smaller bandgap than Ga₂O₃. High variability for E_g value can be found in literature (E_g = 4.1 ± 0.3 eV [18, 19]). Our tantalum oxide samples are characterized by an average (optical) bandgap of 3.8 eV (corresponding to an onset excitation wavelength of 325 nm, details will be presented in *chapter 5*). Accordingly to the band structure, its activity is expected to be maximum using the UVFS filter and consistently diminished using a BK7 window. The activity with the FGUV11S filter should be intermediate between the two as more UV spectrum would be allowed to pass through the filter. Contrarily to the expectations, both BK7 and FGUV11S filters acted similarly, suppressing the catalytic activity (Figure 4-7b), in a very similar fashion as observed for the gallium oxide based catalyst (Figure 4-7a). This finding might imply that the semiconductor model might not be correctly describing the activity observed for tantalum based materials. It is in other words more likely that surface reaction states and TaO_xⁿ⁻ units might be responsible for the actual photocatalytic process (as in Anpo's model for TiO₄ⁿ⁻ units [20]). The band structure, usually considered as the basis of the photocatalytic mechanism, might play a negligible role.

Notably, it is not possible to exclude that also gallium oxide works by the same mechanism. The catalytic process, triggered by highly energetic UV light, might similarly depend on GaO_x surface species rather than band transitions. The high E_g in gallium oxide does not allow to distinguish which pathway is active, by a simple light filtering experiment.

4.3.6 Ga, Ta, Ti OXIDES SERIES UPON Zn DOPING AND Rh/Cr DEPOSITION:

DISCUSSION AND MECHANISTIC REMARKS

Interestingly, oxygen productivity is heavily affected by catalyst tuning in the Zn/Rh-Cr series. Focusing on the Ta₂O₅-based catalysts, oxygen is consumed during the irradiation in absence of Rh/Cr co-catalyst and it is reversely produced in its presence. In other words, the Rh/Cr co-catalyst could be clearly associated with photocatalytic oxygen evolution.

Bare and Zn-doped Ta₂O₅ materials are capable of H₂ evolution but do not appear to bear efficient catalytic sites for complete O²⁻ oxidation. Rather, the reaction appears to be suppressed by competing with O₂ recombination. Oxygen is then possibly converted to (i) hydroxyl surface species (similar to the ones observed in DRIFTS measurements on TiO₂, *chapter 3*) or to (ii) peroxy or radical oxygen species (for example O₂^{•-}, HO[•], HOO[•]) released in the slurry, or simply (iii) back to water, nullifying the splitting activity. Many of these species are often reported in literature and considered active reactants in photocatalytic decomposition of organic compounds, when using these catalysts for water purification or biomass transformation [21-24].

The capture/reaction of oxygen and the oxygen evolution reaction appear to be competitive phenomena occurring at different surface sites. We could hypothesize that the former occurs on the semiconductor catalyst surface, the latter on Rh/Cr particles. This statement would be supported by the fact that oxygen evolution is also clearly stepped up upon Rh/Cr deposition for Ga₂O₃ based catalysts (Figure 4-4). It is striking to observe that upon Zn doping of Ga₂O₃ a fivefold raise in hydrogen evolution is not counterbalanced by equivalent oxygen production (Figure 4-3). On the other hand, as soon as the material is promoted with Rh/Cr, oxygen evolution is triggered. If we compare Ga₂O₃ Rh/Cr with Ga₂O₃, we can notice that the doubling in activity is

counterbalanced by triggering of O_2 production up to even the over-stoichiometric evolution (Table 4-1).

Rh-Cr catalyst is nevertheless reported in literature to be acting as hydrogen evolution site, rather than oxygen one [4, 25], as more characteristic of a noble metal such as rhodium. If this is true, the oxygen evolution boosting effect of this co-catalyst may rely on a double action. It might be working first as a very efficient electron trap and hydrogen evolution site, and at the same time it might be physically or chemically poison the surface oxygen recombination sites. The suppression of the recombination activity may result in promoting the full overall water splitting process (Figure 4-8).

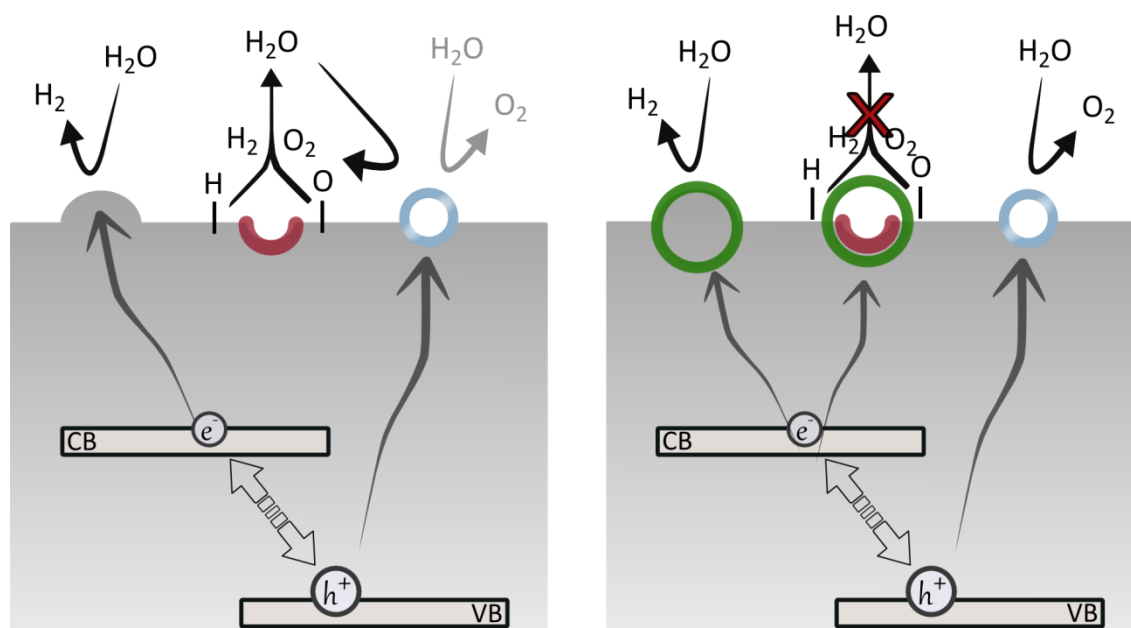


Figure 4-8. Possible mechanistic scheme of Rh-Cr boosting effect. On the left, in absence of Rh-Cr, recombination sites are active (red); oxygen evolution sites (blue) are short circuited. On the right, Rh-Cr co-catalyst (green) inhibits the recombination sites and boosts H_2 and O_2 production at the same time.

TiO_2 -based catalysts display very low activity for H_2 evolution as compared to Ta_2O_5 and Ga_2O_3 -based catalysts. Apart from the already highlighted absence of synergetic effect between Zn/Rh-Cr modifications, oxygen evolution is never observed in this

series. Conversely, consumption of oxygen is observed for TiO_2 Rh/Cr and TiO_2 Zn. Bare TiO_2 is possibly too little active to give detailed comparisons. On the other hand, TiO_2 Zn-Rh/Cr undoubtedly displays a boost in H_2 production and a zero balance for oxygen. This suggests that this catalyst is possibly representative of the crossing limit in which oxygen sequestration and evolution sites buffer each other.

As a matter of fact, Rh/Cr co-catalyst does not seem to bear on TiO_2 the same efficient tuning power for catalytic oxygen evolution observed for Ga and Ta oxides. This might be related to the electronic structure of TiO_2 , characterized by a lower bandgap, ≈ 3 eV as compared to > 3.8 eV wide bandgap of Ga_2O_3 and Ta_2O_5 . More details of how photophysics properties might correlate with photocatalytic activity will be tackled in *chapter 5*.

Despite the high H_2 productivity, CO_2 reduction products were never observed in the gas stream. This indicates that other chemical structure or reaction approaches are to be addressed or coupled in order to exploit the high reductive capability of these catalysts for CO_2 conversion.

4.4 WATER SPLITTING PHOTOCATALYSTS AND MODIFICATION

SERIES WITH Zn AND Rh/Cr: GAS PHASE REACTOR

4.4.1 Ga_2O_3 Zn-Rh/Cr AND Ta_2O_5 Zn-Rh/Cr: gas phase activity

The activity of the Zn-Rh/Cr co-modified catalysts (1+2), described in the section 4.3, was confirmed to be in the range of the most active reported catalyst to date. The resulting activity in continuous flow is in good agreement with the data previously reported in literature for batch slurry reactors [1-3, 14, 15].

This section examines the photocatalytic activity of the Zn-Rh/Cr co-modified Ga₂O₃, Ta₂O₅ and TiO₂ in the continuous flow gaseous w-CO₂ reactor, in an analogous fashion as described for Pt/TiO₂ catalyst in *chapter 3*. Three reaction temperatures of interest, at which the product concentrations were followed by GC calibrated MS, were selected based on our previous experience:

- **323 K**, achieved dissipating and equilibrating the heat delivered the lamp in a water bath
- **373** and **423 K** by heating the reactor by means of PID controlled heating cartridges.

The three temperature set points were consecutively changed from lowest to highest without catalyst change, allowing thermal stabilization in the dark and purging of the products from the previous irradiation period. The same trends were observed for the three photocatalyst, with dramatic activity differences but following the same reactivity pattern as in the slurry case (*vide supra*). MS traces for Ga₂O₃ Zn/Rh-Cr reaction are shown in Figure 4-9 as the most representative example.

As summarized in Table 4-2, Ga₂O₃ Zn-Rh/Cr and Ta₂O₅ Zn-Rh/Cr are sustaining overall water splitting activity in all the reaction temperatures investigated. Hydrogen and oxygen are evolved from water vapour in the gas stream in ratio close to the stoichiometric ratio 2 : 1. Comparable water splitting efficiency is obtained using the gas setup as in the slurry setup. At the best condition, in the gas phase reactor Ga₂O₃ Zn-Rh/Cr reaches over 100 % and Ta₂O₅ Zn-Rh/Cr almost 90 % H₂ productivity registered in the slurry reactor.

Most importantly, increasing reaction temperature was found to have a negative impact on water splitting efficiency. The effect is particularly evident at 423 K with an order of magnitude drop in productivity as compared to 323 K.

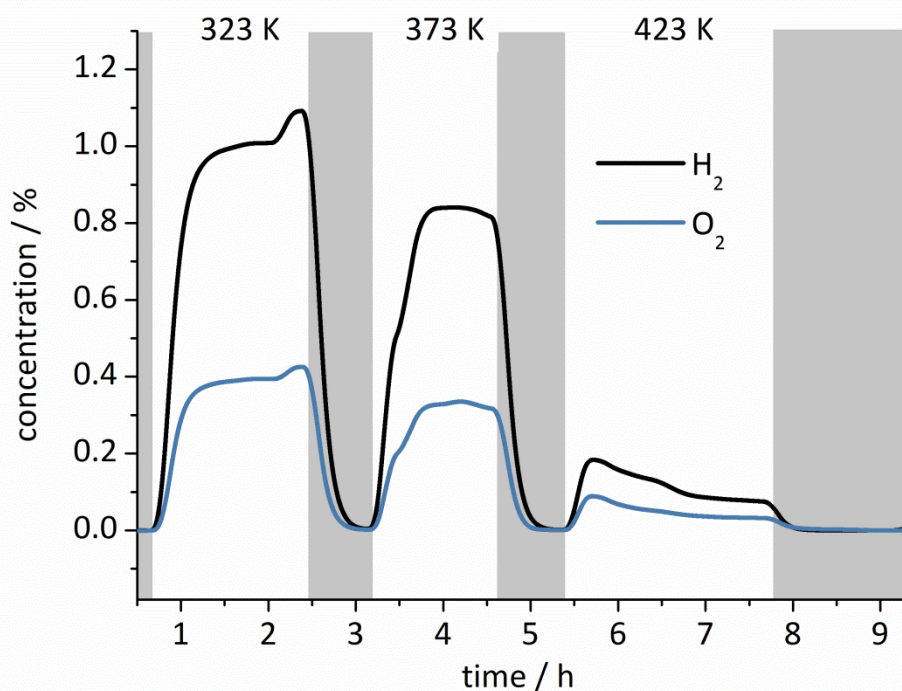


Figure 4-9. H_2 and O_2 concentration profiles for Ga_2O_3 Zn-Rh/Cr catalytic performance in continuous flow gas reactor. The three temperatures used during photocatalytic testing (light on) are highlighted at the top. Shaded rectangles (light off) highlight the temperature stabilization and reactor purging intervals between the tests. Restarting the temperature cycle reproduced the same activity level without an indication of deactivation due to temperature (not shown).

Table 4-2. H_2 and O_2 steady state productivity ($\text{mmol}\cdot\text{g}^{-1}\cdot\text{h}^{-1}$) values for the Ga_2O_3 Zn-Rh/Cr and Ta_2O_5 Zn-Rh/Cr catalysts in continuous gas flow of $w\text{-CO}_2$ at three different temperatures (323, 373, and 423 K).

Catalyst	323 K		373 K		423 K	
	H_2	O_2	H_2	O_2	H_2	O_2
Ga_2O_3 Zn-Rh/Cr	6.39	2.43	5.00	1.90	0.50	0.19
Ta_2O_5 Zn-Rh/Cr	0.58	0.17	0.28	0.13	0.09	0.08

This behaviour is consistent with what described in detail using Pt/TiO₂ (*chapter 3*), and can be explained in terms of water concentration at the surface of the catalyst. Water concentration at the catalyst surface is the highest in the slurry setup, where catalyst particles are surrounded by liquid water. In our gas phase setup, on the contrary, the highest surrounding water concentration can be limited by saturation of its vapour in CO₂ stream. Furthermore, water has to adsorb on the surface and must establish condensation equilibrium at the catalyst surface. The higher the temperature, the more the equilibrium will be shifted to gaseous water vapour and less condensed water will be available for reaction. At > 373 K water condensation is limited and a stronger drop in reactivity is observed.

The activity difference observed between slurry and gas phase setups (at 323 K) is practically negligible. This is remarkable, especially in the light of the much better catalyst-water interaction allowed in the slurry setup, expectedly delivering much higher activity. This fact demonstrates that water splitting could be effectively obtained in a gaseous flow stream and also that productivity as high as in slurry reactor can be achieved by a proper reactor design and reaction condition to allow for better catalyst-water interaction. For example, adjusting a higher H₂O/CO₂ ratio in the feed gas or utilizing a micro plug flow reactor or fluidized bed reactor would be likely improving the performance. The possible limitation at present for the materials investigated is the very short excitation light wavelength, which demands the use of fragile and expensive quartz as optical material.

4.4.2 Ga₂O₃ Zn-Rh/Cr: K PROMOTION

Alkaline promoters such K and Ba have been reported to significantly enhance reaction rate and selectivity to desired products in CO₂ reduction reactions over Cu

based catalysts [26, 27]. The origin of promotion has been attributed to the high affinity of CO₂ to these metals and derived metal oxide/hydroxide, allowing formation of carbonates species on the surface. This carbonates can then effectively react to produce reduced carbon compounds.

In order to investigate whether potassium could promote the desired but missing CO₂ reduction on Ga₂O₃ Zn/Rh-Cr catalyst, we prepared and tested a 5 wt% K impregnated sample of the latter.

Contrarily to our expectations, we could not detect any reduced carbon compound either during gas phase or slurry phase testing. Water splitting activity for the slurry phase reactor appeared unchanged (possibly also due to leaching of K in the suspension). Moreover, in gas phase reactor the activity was reduced to approximately a 25 % comparing the best conditions for the two catalysts (Table 4-3). This fact could be interpreted as potassium partially covering reaction sites, hindering water splitting activity. Most interestingly, the temperature dependence of productivity was reversed. As opposed to what was observed for K-free catalyst the K impregnated one showed higher H₂ and O₂ production at higher temperature (Figure 4-10 and Table 4-3). At the highest temperature (423 K) productivity was more than trebled upon K promotion as compared to the unpromoted sample.

Table 4-3. H₂ and O₂ steady state productivity (mmol·g⁻¹·h⁻¹) values for the Ga₂O₃ Zn-Rh/Cr and the Ga₂O₃ Zn-Rh/Cr 5 wt% K catalysts in continuous gas flow of w-CO₂ at three different temperatures (323, 373, and 423 K).

Catalyst	323 K		373 K		423 K	
	H ₂	O ₂	H ₂	O ₂	H ₂	O ₂
Ga ₂ O ₃ Zn-Rh/Cr	6.39	2.43	5.00	1.90	0.50	0.19
Ga ₂ O ₃ Zn-Rh/Cr 5 wt% K	1.02	0.37	1.39	0.49	1.66	0.64

Even though the overall productivity was negatively affected by K promotion, this test shows that alkaline metal impregnation is a potentially powerful method to tune a catalyst to specific reaction conditions. Under irradiation, high temperatures can be reached and heat dissipation can be a challenge from both technical and economic point of view. Moreover, higher temperature is rather likely to be beneficial to thermodynamically disfavoured reactions like CO₂ reduction. It would be therefore counterintuitive to willingly lower the temperature for the operation of future artificial photosynthesis plants. For these reasons, effectively modifying a catalyst to be more efficient at high temperature would certainly be regarded as an advantage and could give an added value to this promotion strategy.

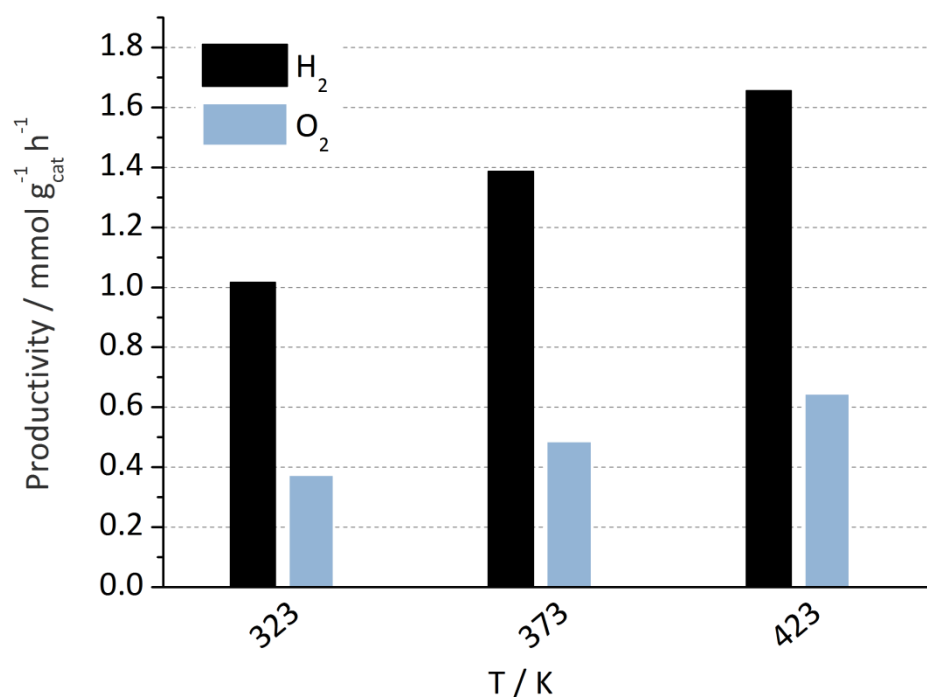


Figure 4-10. Temperature dependence of K promoted Ga₂O₃ Zn-Rh/Cr catalyst productivity

4.5 Zn AND Rh/Cr MODIFICATIONS OVER TANTALATES

4.5.1 TANTALATE CLASS MATERIALS: SYNTHESIS AND PROPERTIES

Tantalate materials of the general formula $MTaO_3$ (M is most commonly a group I alkali metal or group II alkaline earth metal) were reported to display unprecedented overall water splitting activity starting from the decade of the 2000s. The most active and studied is $NaTaO_3$, which was further effectively doped and activated with La ions and with co-catalysts such as Pt, NiO and RuO_2 . This research line, especially developed by Kudo and Kato, culminated with materials capable of over $7 \text{ mmol} \cdot \text{g}_{\text{cat}}^{-1} \cdot \text{h}^{-1}$ hydrogen productivity under UV light by overall water splitting [5-7].

These materials can be synthesized by different approaches, most commonly involving a high temperature treatment of a mixture of Ta_2O_5 as tantalum precursor and an alkaline metal salt or oxide. The final product is a perovskitic material with ilumenite structure and $Ta^V O_6$ corner sharing octahedra and M^+ or M^{2+} as counter ion. This structure is typically formed upon heating the precursor's mixture at temperature over 1273 K for long time (> 10 h) [9]. Alternatively, the materials can be synthesized at lower temperature and shorter time (e.g. 873 K for 4 h) using molten salts flux (such as NaCl/KCl or Na_2SO_4/K_2SO_4) as reaction medium and reactant [9, 28] or using an organic compound (such as urea) that combusts upon heating and locally boosts the temperature driving the phase transformation [8, 29]. It is also possible to achieve the formation of tantalate phases at temperature as low as 773 K by heating a tantalum material precursor synthesised by means of sol-gel techniques (starting from $TaCl_5$ or $Ta(OEt)_5$ as precursors)[30, 31].

Even milder temperature (453 K, 12 h) can be used under hydrothermal conditions in basic aqueous media (NaOH), to effectively transform tantalum oxide in a tantalate [32, 33].

High temperature calcination, molten salt, urea combustion, and hydrothermal synthesis were successfully reproduced along with this thesis work. XRD diffraction patterns of the most significant materials obtained are summarized in Figure 4-11.

Purest tantalate phase materials were obtained using purely thermal (Figure 4-11, b), urea combustion (Figure 4-11, c) and molten salt techniques (Figure 4-11, d). Under these synthesis conditions, tantalum oxide (Figure 4-11, a) fully converts into tantalate. Nevertheless, it is worth mentioning that the thermal method (Figure 4-11, b) requires extreme care in initial mixing of reagents (also assisted by ball milling). Moreover, dividing the calcination process into two steps with intermediate crushing can be beneficial to help phases intermixing. The sample described here was also doped with La ions (2 mol%, adding La_2O_3 to reagents Ta_2O_5 and Na_2CO_3), as it was reported to be beneficial to water splitting activity [5]. On the contrary, urea combustion and molten salt methods do not suffer from the previous drawbacks and proved to be more robust. Giving extra local temperature boost (the former) or ensuring better and constant phase intermixing (the latter), they produce clean tantalate phases with improved reproducibility.

As far as the hydrothermal synthesis is concerned, nitrogen-doped sodium tantalate was produced by 12 h treatment in autoclave in 0.83 M aqueous NaOH at 453 K (Figure 4-11, e); nitrogen incorporation is achieved by adding NH_4OH to the mixture as reported in literature [32]. The tantalate phase is the major crystal structure obtained; nevertheless, relevant traces of unchanged $\beta\text{-Ta}_2\text{O}_5$ phase were detected, indicating that the reaction did not reach completeness.

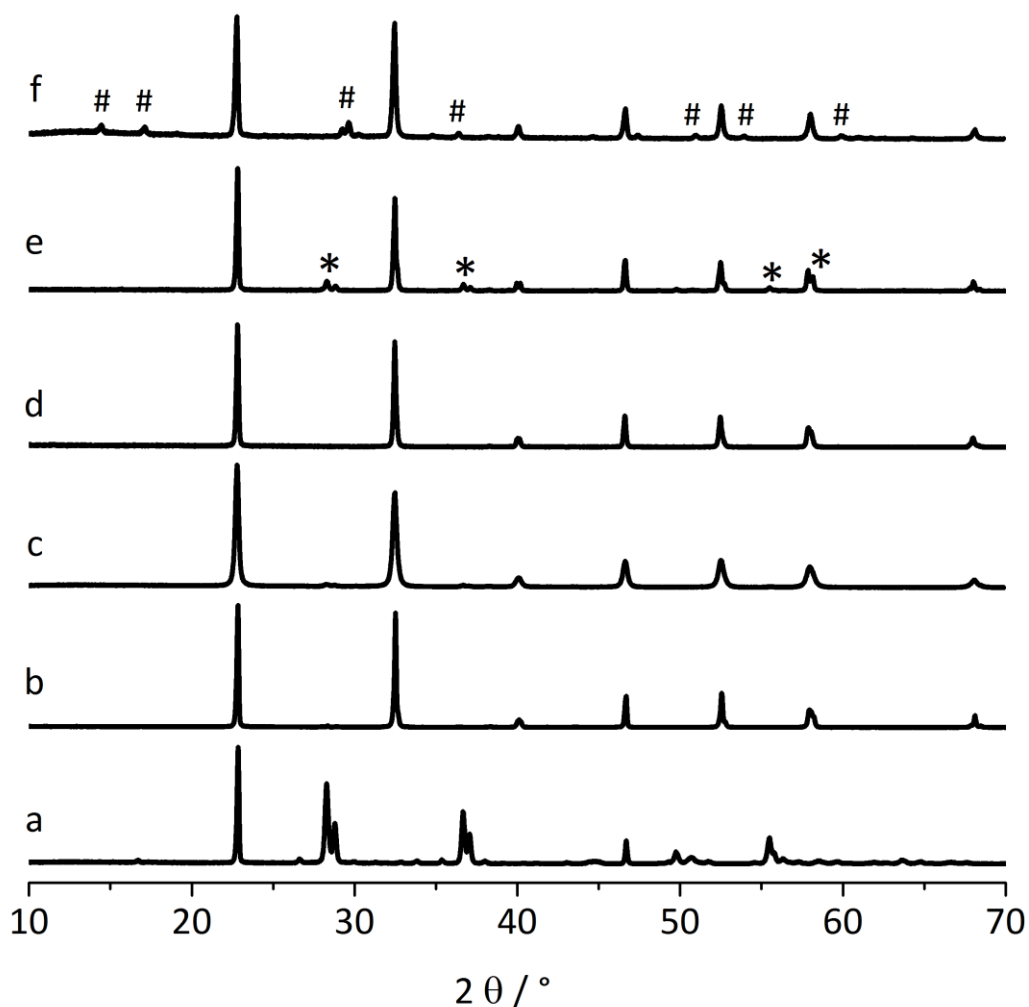


Figure 4-11. XRD diffractograms of a) β - Ta_2O_5 phase starting material, and the most significant MTaO_3 materials synthesized: b) $\text{NaTaO}_3\text{:La}$ (La 2 wt%, loaded as La_2O_3) prepared with simple calcination method at 1373 K for 10 h, c) NaTaO_3 prepared by urea combustion method at 873 K for 4 h, d) $\text{K}_{0.4}\text{Na}_{0.6}\text{TaO}_3$ prepared by eutectic molten salt technique (NaCl/KCl flux) at 1023 K for 2 h, e) $\text{NaTaO}_3\text{-N}$ prepared by hydrothermal method in autoclave at 453 K for 12 h, f) $\text{NaTaO}_3\text{-N Zn/Rh-Cr}$ prepared from “e”) by the two sequential modification steps identical to Ga_2O_3 Zn/Rh-Cr described in section 4.3.2. The symbols * and # respectively highlight the residual unreacted β - Ta_2O_5 phase starting material and natrotantite ($\text{Na}_2\text{Ta}_4\text{O}_{11}$) phase.

Further calcination of this sample at different temperatures between 523 and 1123 K for 1.5 h were performed and the crystal structure was studied by XRD (Figure 4-12).

The material remains substantially unchanged regarding its structural composition up to 923 K. Between 923 and 1123 K the residual Ta_2O_5 undergoes phase transition into natrotantite ($\text{Na}_2\text{Ta}_4\text{O}_{11}$) phase.

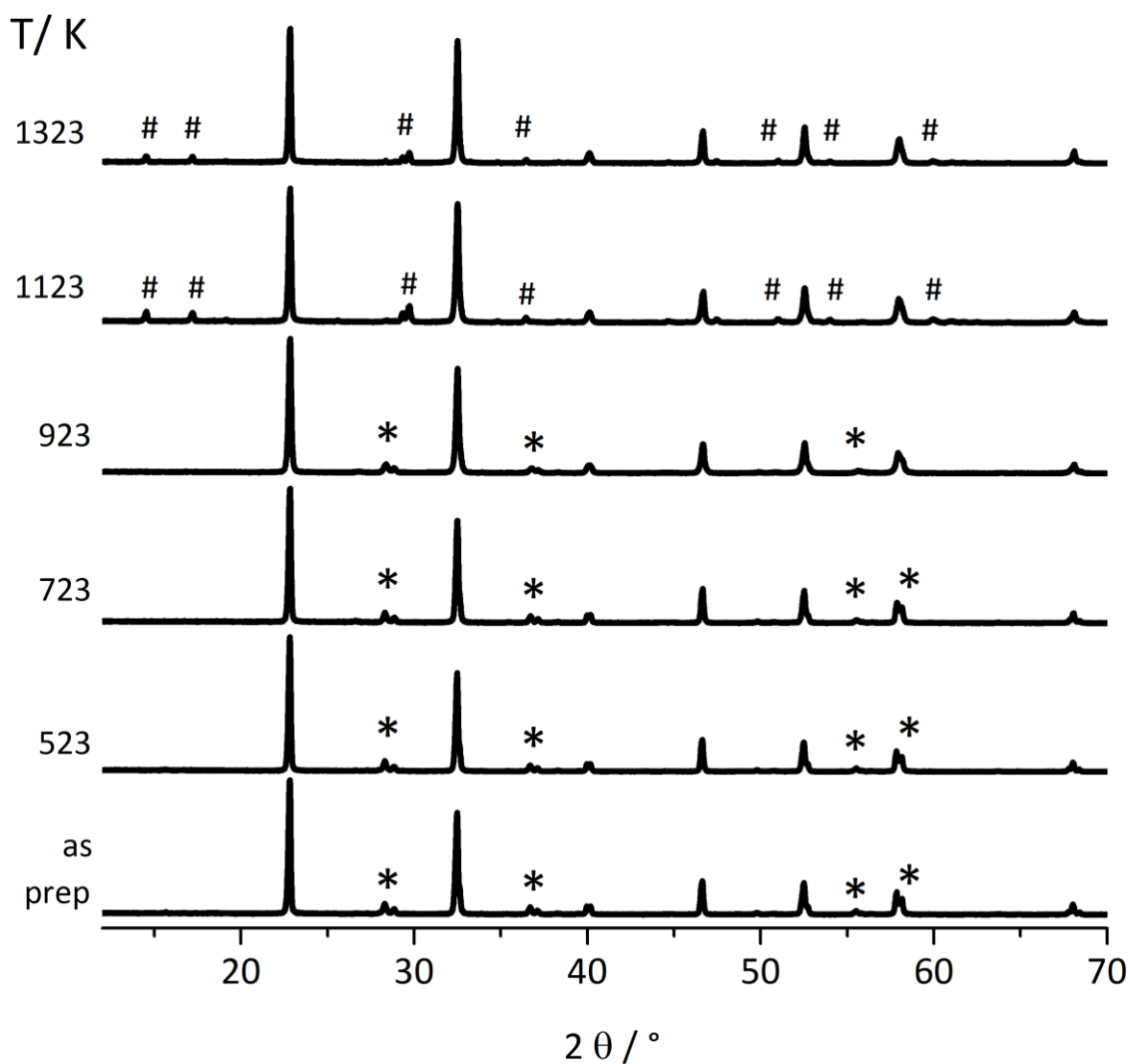


Figure 4-12. XRD diffractograms of $\text{NaTaO}_3\text{-N}$ prepared by hydrothermal method in autoclave at 453 K for 12 h, as prepared and after calcination for 1.5 h at 523, 723, 923, 1123, 1323 K. The symbols * and # respectively highlight the residual unreacted $\beta\text{-Ta}_2\text{O}_5$ phase starting material and natrotantite ($\text{Na}_2\text{Ta}_4\text{O}_{11}$) phase.

Tantalate phase remains apparently unchanged in this temperature range. The formation of natrotantite was also noticed in the case of purely thermal synthesis at >

923 K (not shown), and it could be correlated to insufficient amount of sodium to react with tantalum oxide, due to partial volatilization of the former during the thermal treatment.

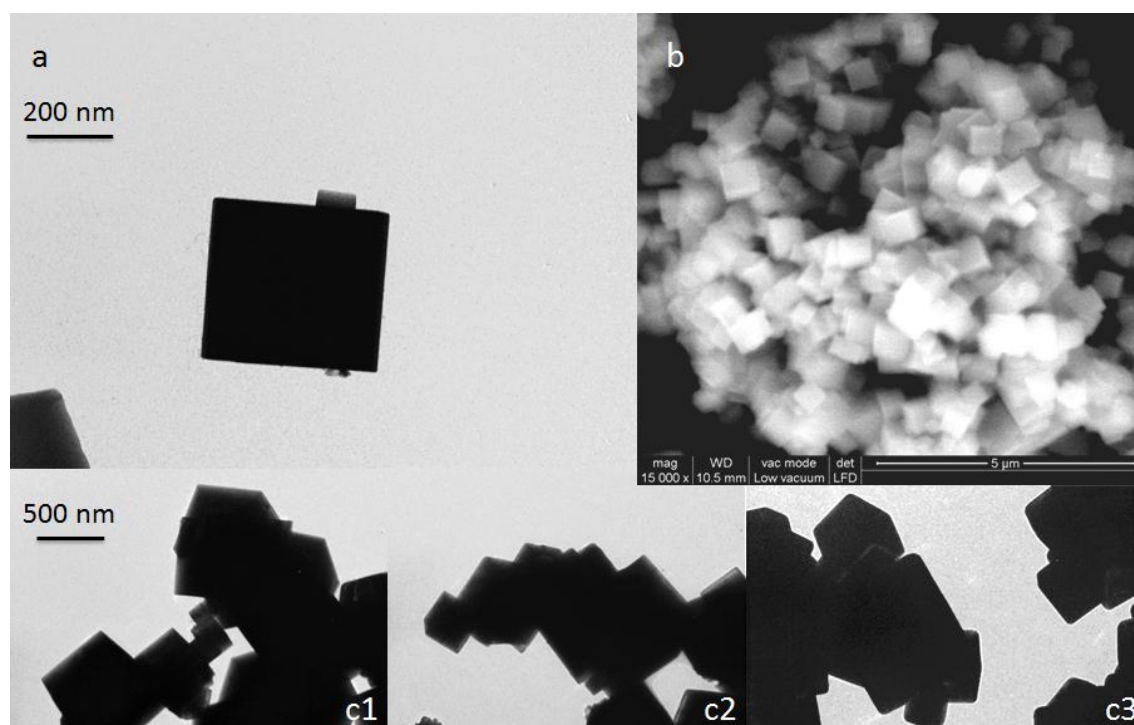


Figure 4-13. Micrographs of $\text{NaTaO}_3\text{-N}$ material: a) TEM image of as prepared material, b) ESEM image of as prepared material and TEM images of the material after thermal treatment for 1.5 h at c1) 523, c2) 723, and c3) 1323 K.

Sharp hedges and cavities have been reported to be highly beneficial for specific redox activity of tantalates. Their presence and stability are good morphological features we aim to achieve for this class of material [5]. Despite the marginal differences in crystal structure composition, the hydrothermal synthesized material displays excellent and stable morphological properties.

The TEM and ESEM images (Figure 4-13) show that the materials has a well-defined nanostructure consisting of sharp nanocubes with typical dimension of 500 nm (edge); also a minor amount of smaller nanocubes is present (Figure 4-13c), down to

approximately 50 nm edge. This structure is stable at all the calcination temperatures investigated. Even though at 1323 K hints of smoothing and possible sintering of the cubes may be detected (Figure 4-13, c3), the overall stability of this nanostructure under the harsh thermal condition is remarkable.

Due to these interesting morphological properties the hydrothermally synthesised material (as prepared) has been further subjected to (1+2) modifications (described in *section 4.1.3*) to obtain NaTaO₃-N Zn/RhCr. The XRD diffraction pattern of this material (Figure 4-11 f) showed no relevant differences compared to the non Zn/Rh-Cr doped material calcined at T = 1123 K (Figure 4-12). This is coherent with the calcination step performed for Zn doping, also performed at 1123 K. This data also suggests that zinc, even if efficiently incorporated, does not cause modifications of the tantalate crystal structure.

Also NaTaO₃ prepared by urea combustion has been further modified, by applying only the step 2 in the method describes in *section 4.1.3* to give NaTaO₃ Rh-Cr.

4.5.2 TANTALATE CLASS MATERIALS REACTIVITY FOR WATER SPLITTING

During the course of our investigations, many tantalum based materials have been synthesized as promising candidates for overall water splitting. As further variety to the different materials described in the previous section, different doping and co-catalyst impregnation have been attempted. Apart from the already mentioned La and N doping, Cu, Fe, and Ti doping were attempted with the hydrothermal approach. Ni, Pt, and Ru based co-catalyst impregnation on different tantalate substrate were also performed and these materials were tested for water splitting activity.

Contrarily to our expectation, no one of these materials was capable of overall water splitting activity or oxygen production in either slurry or gas phase. Hydrogen

evolution productivity was in most case present, but at level in the range of bare Ta_2O_5 (*section 4.3.4*): more than one order of magnitude inferior to data reported in literature for tantalate materials.

Remarkably different behaviour was observed for NaTaO_3 -N Zn/Rh-Cr and NaTaO_3 Rh-Cr loaded catalysts. They exhibited excellent quasi-stoichiometric H_2 and O_2 evolution in slurry under UV irradiation (Figure 4-14, Table 4-4).

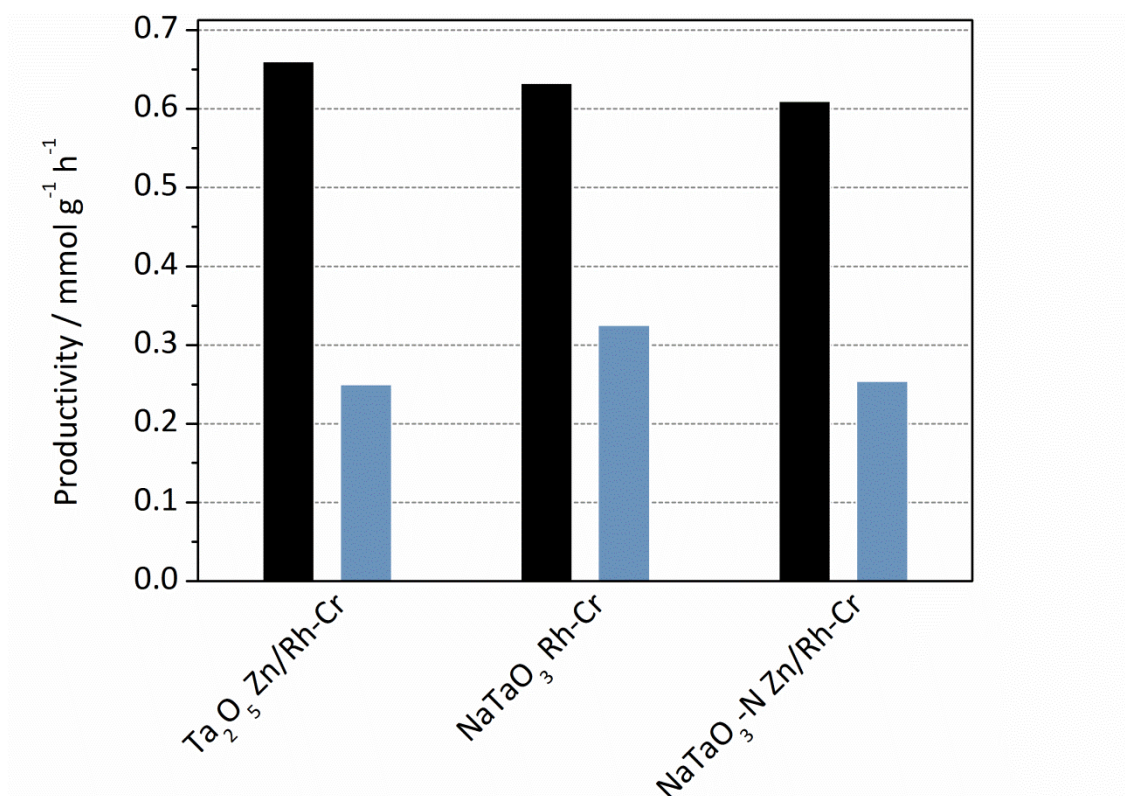


Figure 4-14. Comparison of H_2 and O_2 steady state productivity of Ta_2O_5 Zn/Rh-Cr, NaTaO_3 Rh-Cr and NaTaO_3 -N Zn/Rh-Cr catalysts.

Table 4-4. H₂ and O₂ productivity (mmol·g⁻¹·h⁻¹) values for Ta₂O₅ Zn/Rh-Cr, NaTaO₃ Rh-Cr and NaTaO₃-N Zn/RhCr catalysts in slurry.

Catalyst	H ₂	O ₂
Ta ₂ O ₅ Zn-Rh/Cr	0.66	0.25
NaTaO ₃ Rh-Cr	0.63	0.32
NaTaO ₃ -N Zn/RhCr	0.61	0.27

As evident from Figure 4-14 and Table 4-4, the two Rh-Cr modified tantalum oxide display very similar catalytic activity. Especially, Zn doping does not seem to have any relevant (or even slightly negative) effect on the productivity. Even more importantly, the productivity is equivalent to what observed for Ta₂O₅ Zn/Rh-Cr, with a possible slight improvement in oxygen evolution (which gets closer to the desired stoichiometry).

These findings showed that crystal structure only played a marginal role in determining the activity of Rh-Cr impregnated tantalum based materials, supporting the previously suggested non-semiconductor-based mechanism. Other parameters, such as the presence of specific Ta-O surface active units, and their interaction with the Rh-Cr co-catalyst, could be better explaining the similar catalytic activity observed for the Ta₂O₅ and MTaO₄ materials.

4.6 CONCLUSIONS

Zn, Rh-Cr, and Zn/Rh-Cr modified gallium, titanium, and tantalum oxides were successfully prepared and tested in slurry and in gas phase reactor for overall water splitting reaction. Common productivity trends were found in the material investigated and, despite starting from different intrinsic activity for the bare oxides, the

productivity order: bare oxide < Zn < Rh-Cr < Zn/Rh-Cr was consistently reproduced. The intrinsic activity of the metal oxides was also found to be extremely important, as the photocatalytic activity in terms of H₂/O₂ productivity can vary up to three orders of magnitude. Productivity values comparable level to state-of-the-art (6.3 mmol·g⁻¹·h⁻¹ for our Ga₂O₃ Zn/Rh-Cr vs. ca. 20 mmol·g⁻¹·h⁻¹ of H₂ reported in batch [1]) were reached testing Ga₂O₃ materials. Tantalum based oxides also displayed excellent activity but an order of magnitude below promoted Ga₂O₃ materials. TiO₂ based materials, despite the fact that they are the most reported photocatalytic material, were more than 100 times less active than gallium oxide based materials.

Investigating in more detail the effect of doping and co-catalyst modifications, it appeared evident that the role of Rh_{0.5}Cr_{0.75}O₃ is essential to consistently drive high rate overall water splitting. Oxygen production was only observed in presence of co-catalyst; hydrogen production was although equally boosted. This led to the hypothesis that Rh_{0.5}Cr_{0.75}O₃ boosting mechanism relies on a dual action: enhancing on the one hand hydrogen evolution (working with the classical electron trapping mechanism) and from the other suppressing oxygen recombination sites, possibly by their simple coverage.

Zinc doping is certainly relevant for photocatalytic activity but in a totally different and less specific way. Zinc doping alone does not trigger consistent oxygen evolution, and only marginally affects hydrogen one. However, its synergetic combination with Rh_{0.5}Cr_{0.75}O₃ gives rise to the best catalytic activity in all catalyst modification series. This suggests that zinc might not be an active element of the HER or OER sites. Nevertheless, it might be actively involved in the process of formation of stable states of charge separation after light excitation. Long living charges would then only fruitful acting in the catalysis in presence of an efficient surface charge trapping agent, namely Rh_{0.5}Cr_{0.75}O₃.

Wavelength dependant catalytic tests showed that only highly energetic $\lambda_{\text{exc}} < 275$ nm UVC radiation can drive the photocatalytic process for both Ga and Ta oxides. This was expected for Ga_2O_3 -based materials but not for Ta_2O_5 -based materials whose bandgap should allow for a less energetic light activation. Together with the fact that very similar catalytic results were obtained for either tantalum oxide or tantalate materials, these data might suggests that photocatalytic activity does not necessarily follow Bard's semiconductor mechanism, but possibly Anpo's isolated surface metal oxide catalytic unit mechanism.

BIBLIOGRAPHY

1. Y. Sakata, Y. Matsuda, T. Nakagawa, R. Yasunaga, H. Imamura, K. Teramura, *ChemSusChem* **4**, 181, **2011**.
2. Y. Sakata, Y. Matsuda, T. Yanagida, K. Hirata, H. Imamura, K. Teramura, *Catalysis Letters* **125**, 22, **2008**.
3. Y. Sakata, T. Nakagawa, Y. Nagamatsu, Y. Matsuda, R. Yasunaga, E. Nakao, H. Imamura, *Journal of Catalysis* **310**, 45, **2014**.
4. K. Maeda, K. Teramura, H. Masuda, T. Takata, N. Saito, Y. Inoue, K. Domen, *The Journal of Physical Chemistry B* **110**, 13107, **2006**.
5. H. Kato, K. Asakura, A. Kudo, *Journal of the American Chemical Society* **125**, 3082, **2003**.
6. H. Kato, A. Kudo, *The Journal of Physical Chemistry B* **105**, 4285, **2001**.
7. A. Kudo, H. Kato, *Chemical Physics Letters* **331**, 373, **2000**.
8. J. Xu, Y. He, J. Zhang, J. Qian, D. Xu, X. He, D. Yang, *Micro & Nano Letters* **7**, 72, **2012**.
9. J. Sun, G. Chen, Y. Li, R. Jin, Q. Wang, J. Pei, *Energy & Environmental Science* **4**, 4052, **2011**.
10. H. Fu, S. Zhang, L. Zhang, Y. Zhu, *Materials Research Bulletin* **43**, 864, **2008**.
11. J. B. Varley, J. R. Weber, A. Janotti, C. G. Van de Walle, *Applied Physics Letters* **97**, **2010**.
12. A. J. Bard, *Journal of Photochemistry* **10**, 59, **1979**.
13. A. C. Taş, P. J. Majewski, F. Aldinger, *Journal of the American Ceramic Society* **85**, 1421, **2002**.
14. Y. Noda, B. Lee, K. Domen, J. N. Kondo, *Chemistry of Materials* **20**, 5361, **2008**.
15. K. Sayama, H. Arakawa, *Journal of Photochemistry and Photobiology A: Chemistry* **77**, 243, **1994**.
16. Y. Takahara, J. N. Kondo, T. Takata, D. Lu, K. Domen, *Chemistry of Materials* **13**, 1194, **2001**.
17. J. N. Kondo, Y. Takahara, D. Lu, K. Domen, *Chemistry of Materials* **13**, 1200, **2001**.
18. Z. Tepehan F, E. Ghodsi F, N. Ozer, G. Tepehan G, *Solar Energy Materials and Solar Cells* **59**, 265, **1999**.
19. J. Robertson, C. W. Chen, *Applied Physics Letters* **74**, 1168, **1999**.
20. M. Anpo, H. Yamashita, K. Ikeue, Y. Fujii, S. G. Zhang, Y. Ichihashi, D. R. Park, Y. Suzuki, K. Koyano, T. Tatsumi, *Catalysis Today* **44**, 327, **1998**.

21. M. R. Hoffmann, S. T. Martin, W. Choi, D. W. Bahnemann, *Chemical Reviews* **95**, 69, **1995**.
22. V. M. Daskalaki, P. Panagiotopoulou, D. I. Kondarides, *Chemical Engineering Journal* **170**, 433, **2011**.
23. N. M. Dimitrijevic, B. K. Vijayan, O. G. Poluektov, T. Rajh, K. A. Gray, H. He, P. Zapol, *Journal of the American Chemical Society* **133**, 3964, **2011**.
24. J. C. Colmenares, R. Luque, *Chemical Society Reviews* **43**, 765, **2014**.
25. K. Maeda, K. Teramura, D. Lu, N. Saito, Y. Inoue, K. Domen, *Angewandte Chemie* **118**, 7970, **2006**.
26. A. Bansode, B. Tidona, P. R. von Rohr, A. Urakawa, *Catalysis Science & Technology* **3**, 767, **2013**.
27. C.-S. Chen, W.-H. Cheng, S.-S. Lin, *Applied Catalysis A: General* **238**, 55, **2003**.
28. D. G. Porob, P. a. Maggard, *Journal of Solid State Chemistry* **179**, 1727, **2006**.
29. J. Xu, D. Xue, C. Yan, *Materials Letters* **59**, 2920, **2005**.
30. C.-C. Hu, Y.-L. Lee, H. Teng, *Journal of Materials Chemistry* **21**, 3824, **2011**.
31. C.-C. Hu, H. Teng, *Applied Catalysis A: General* **331**, 44, **2007**.
32. Y.-X. Zhao, D.-R. Liu, F.-F. Li, D.-F. Yang, Y.-S. Jiang, *Powder Technology* **214**, 155, **2011**.
33. X. Li, J. Zang, *Catalysis Communications* **12**, 1380, **2011**.

CHAPTER 5

PHOTOPHYSIC CHARACTERISATION OF PHOTOCATALYTIC MATERIALS

5.1 INTRODUCTION

In this chapter, the photophysics characterizations performed on the catalysts of interest are presented.

Information on light absorption properties of the materials was gained by means of UV-Vis diffuse reflectance spectroscopy. Insights on the transduction of this accumulated energy into emission of less energetic electromagnetic radiation, as well as the time dependence of this phenomenon, were obtained by photoluminescence spectroscopy and time-resolved photoluminescence measurements. Comparing the data obtained with these different techniques, along catalyst of the same family (i.e. subjected to different doping or co-catalyst modification on the same metal oxide), a model was derived unifying photophysical and catalytic mechanisms.

5.2 EXPERIMENTAL SECTION

5.2.1 UV-VIS DIFFUSE REFLECTANCE MEASUREMENTS

UV-Vis diffuse reflectance measurements were carried out on a *Shimadzu* UV-2401PC spectrophotometer equipped with a PMT detector, double beam optics, D₂ and W light sources, and an ISR 240 A BaSO₄ 60 mm integrating sphere.

Powder samples were loaded in a screw mount 25 mm diameter round window (fused silica) holder, allowing ca. 1 mm material thickness. Spectra were collected in 200-800 nm range using BaSO₄ as reflectance standard.

E_g values were estimated by fitting the linear range of the slope change in KM(λ) function (arbitrarily normalized) and intersecting it at KM(λ) = 0.

5.2.2 PHOTOLUMINESCENCE MEASUREMENTS

PL measurements were carried out on a Aminco-Bowman Series 2 Luminescence spectrofluorimeter equipped with a high voltage PMT detector and continuum 150 W Xe light source (spectral PL) as well as a pulsed 7 W Xe lamp allowing PL decay lifetime measurements in the $t > 90 \mu\text{s}$ range. Solid powder samples were loaded in a two components fused silica cuvette bearing a sample pocket (100 μm deep); this was mounted on a variable angle solid support accessory allowing light sampling at + 22° from specular reflection. Emitted light was filtered with a BK7 borosilicate window to avoid the intense visible range harmonic, originating from the UV excitation reflection. All the measurements were performed at RT in air.

PL decay traces vs. time were fitted with double exponential equation in the form

$$\text{Equation 5-1. } y(t) = y_0 + A_1 e^{-t/\tau_1} + A_2 e^{-t/\tau_2}.$$

5.3 UV-VIS DIFFUSE REFLECTANCE MEASUREMENTS: RESULTS

Figures 5-1, 5-2 and 5-3 and Table 5-1 summarize the band gap determination analysis on different Ti, Ga and Ta oxides materials, based on KM plots.

A catalyst family comparison allows us to first order the bandgap values in an ascending scale as follows: titanium oxide (2.87 - 3.25 eV), tantalum oxide (3.71 - 3.86 eV), sodium tantalate (3.79 - 4.01 eV), gallium oxide (4.28 - 4.59 eV).

As expected, it is possible to see that, within the single families, the pure oxides of Ti, Ta, and Ga display the widest bandgap. These values are in good agreement with literature data [1-5]. Interestingly, modification with Rh-Cr always resulted in slight red-shifting of the λ_{onset} value. This is the most evident on titania, resulting in a +27 nm shift of the onset (-0.22 eV). Titania is even more affected by Zn doping, resulting in a

combined + 50 nm shift (- 0.38 eV). Surprisingly also Pt modification on titania could contribute to a onset shift up to + 19 nm (- 0.16 eV).

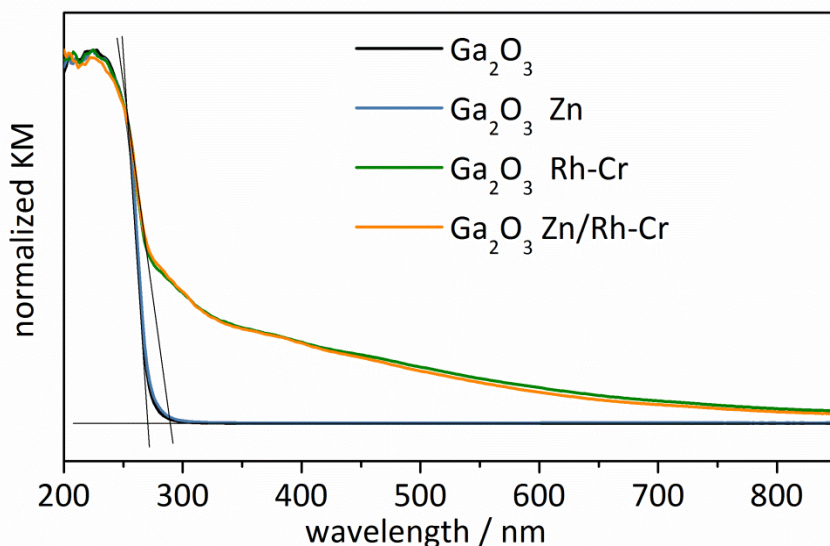


Figure 5-1. Diffuse reflectance KM plots of Ga_2O_3 -based materials (Zn/Rh-Cr modification series). Tauc plots intersecting lines are visualized in black.

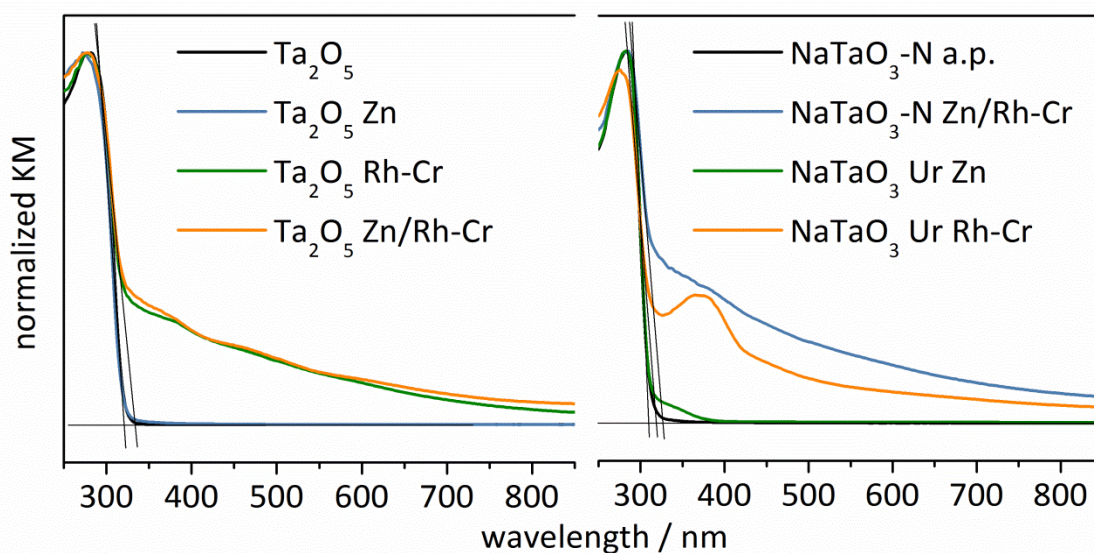


Figure 5-2. Diffuse reflectance KM plots of Ta-based materials. Tauc plots intersecting lines are visualized in black. On the left side tantalum oxide Zn/Rh-Cr series is collected. On the right side selected examples of tantalates material are shown: hydrothermal NaTaO_3 -N, as prepared and Zn/Rh-Cr modified; urea combustion NaTaO_3 as prepared and Rh-Cr modified.

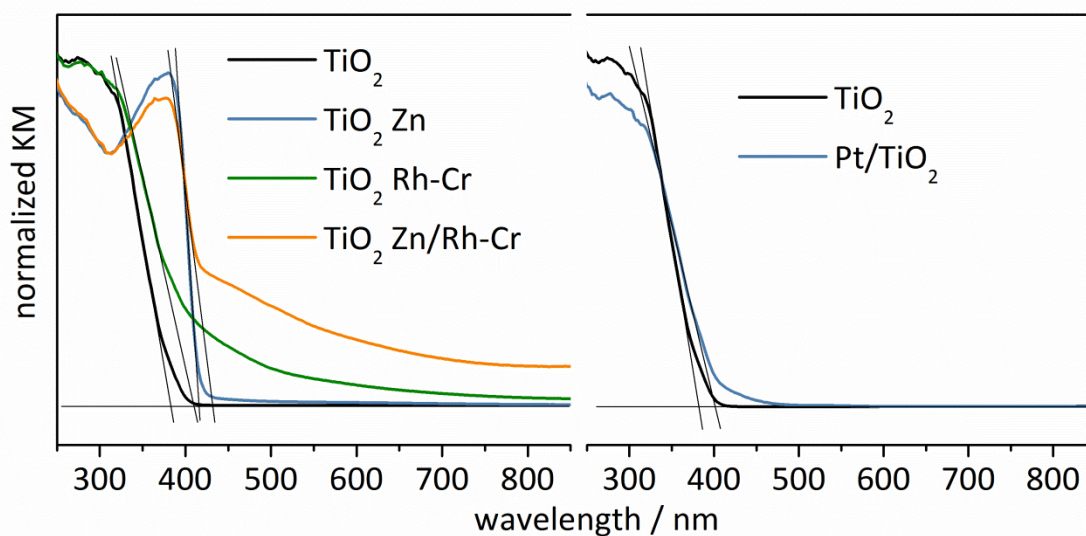


Figure 5-3. Diffuse reflectance KM plots of TiO₂-based materials. Tauc plots intersecting lines are visualized in black. On the left side the Zn/Rh-Cr modification series, on the right side Pt doping effect are shown

Table 5-1. KM plot derived λ_{onset} (from the plots in Figures 5-1, 5-2, and 5-3) and corresponding E_g values (by the formula $E_g = 1240/\lambda_{\text{onset}}$).

Material	λ_{onset} /nm	E_g / eV	Material	λ_{onset} / nm	E_g / eV
TiO ₂	382	3.25	Ta ₂ O ₅	321	3.86
TiO ₂ Zn	416	2.98	Ta ₂ O ₅ Zn	321	3.86
TiO ₂ Rh-Cr	409	3.03	Ta ₂ O ₅ Rh-Cr	334	3.71
TiO ₂ Zn/Rh-Cr	432	2.87	Ta ₂ O ₅ Zn/Rh-Cr	334	3.71
TiO ₂ Pt	401	3.09	NaTaO ₃ -N a.p.	310	4.01
Ga ₂ O ₃	270	4.59	NaTaO ₃ -N Zn/Rh-Cr	327	3.79
Ga ₂ O ₃ Zn	270	4.59	NaTaO ₃ Ur Zn	310	4.01
Ga ₂ O ₃ Rh-Cr	290	4.28	NaTaO ₃ Ur Rh-Cr	319	3.89
Ga ₂ O ₃ Zn/Rh-Cr	290	4.28			

On the contrary, the bandgap of Ga and Ta oxides does not appear to shift upon zinc doping. Only noticeable differences arise after Rh-Cr deposition (+ 13 and +20 nm for Ti and Ga oxide respectively).

Aside from the effect on the bandgap, $\text{Rh}_{0.5}\text{Cr}_{1.5}\text{O}_3$ particles add an extra, wide absorption feature to the spectra, overlapping to the semiconductor band-to-band transition in the UV (where it most likely meets its maximum) but slowly diminishing its intensity towards the visible range and reaching up to the NIR region. It is this absorption feature responsible for the brownish colour of the material.

Sodium tantalate samples shown in Figure 5-2 suggest a similar behaviour as the other samples upon Rh-Cr modification. A new absorption feature seems to present for only urea combustion prepared NaTaO_3 Rh-Cr sample, i.e. the extra absorption band with peak at 375 nm.

This dataset collectively shows that Rh-Cr can actively modify the bandgap of the investigated materials, whereas zinc only appeared to have an effect on titania. Nevertheless, the absolute shift in the bandgap values does not appear to be sufficiently relevant to justify the drastic changes in catalytic activity shown in *chapter 4*. It is also remarkable how the activity of the different catalyst family appears to be reversely proportional to their spectral light harvesting capabilities. Indeed, the wider the bandgap and the lower the portion of absorbable energy frequencies from the light source, the higher the water splitting activity found in this work. Gallium oxide appears to be ten times more efficient than tantalum based materials, despite the latter material being able to absorb up to about 60 nm extended wavelength range. Titania does not reach 0.4 % the activity of the gallium based materials, although it has an even more than 100 nm extra range of light absorption as compared to gallium oxide.

5.4 PHOTOLUMINESCENCE MEASUREMENTS: RESULTS

5.4.1 PHOTOLUMINESCENCE SPECTRA

Photoluminescence spectra ($\lambda_{\text{exc}} = 265$ nm) collected for Ti, Ga, and Ta oxides family are shown in Figures 5-4, 5-5 and 5-6. For each group of materials, the optical parameters for the measurements (e.g. bandpass slit opening, and detector gain voltage values) were fixed, allowing comparison and semi-quantitative analysis.

The dynamic range of the instrument did not allow the use of identical optical parameters along different groups. Nevertheless, it was possible to verify that all materials were photoluminescent at RT in air. Their average absolute photoluminescence intensity followed the trend of Ga- > Ta- > Ti-oxides.

We mostly focus here on relatively high stoke shift long wavelength emissions, as they are most often related to surface state radiative recombination pathways, shared with photocatalytic mechanisms [6, 7].

At a first glance the emission observed from titania samples (Figure 5-4) can be ascribed to the overlap of band to band and exciton emission, one centred at $\lambda = 410$ nm, the other appearing as the multiple bands at $\lambda > 445$ nm [8]. Also it can be noticed that upon zinc doping, the short wavelength tail ($\lambda < 410$ nm) is substantially diminished. This might imply that Zn suppresses considerably the most energetic band-to-band recombination, consequently boosting the exciton emission component. Therefore we assigned the emission $\lambda < 410$ nm to the former origin. The latter can then be assigned, according to Liu et al. [6] to surface defects recombination and to bulk phonon coupled recombination in correspondence of the sharp peaks ($450 < \lambda < 500$ nm).

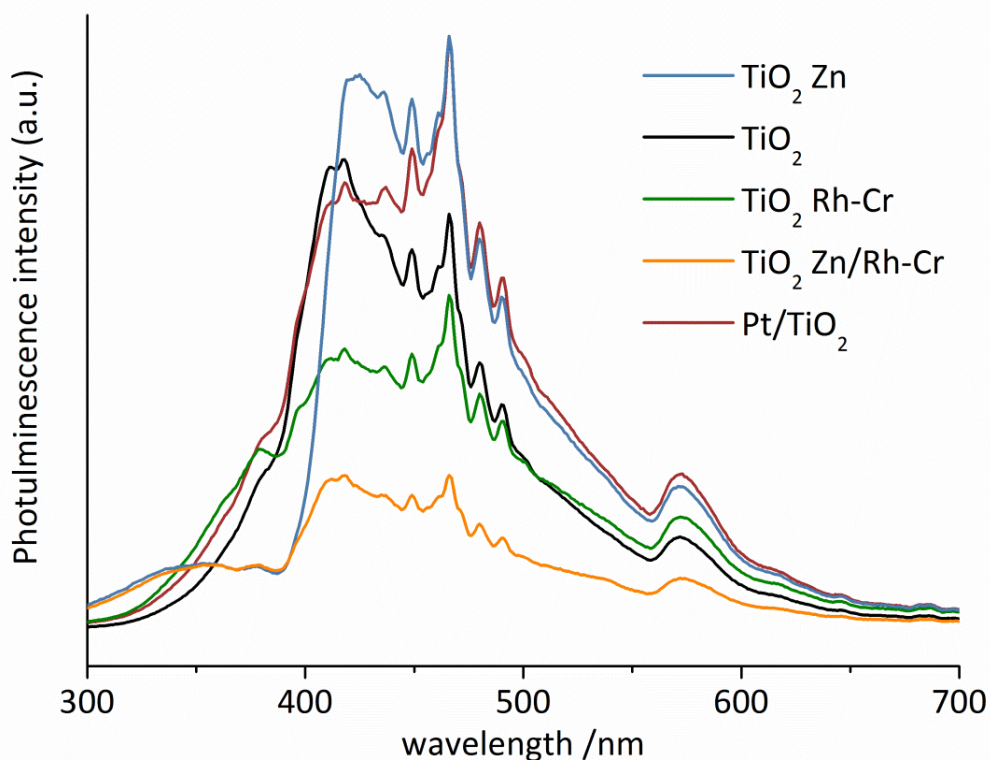


Figure 5-4. Photoluminescence spectrum of TiO₂-based materials. λ_{exc} = 265 nm.

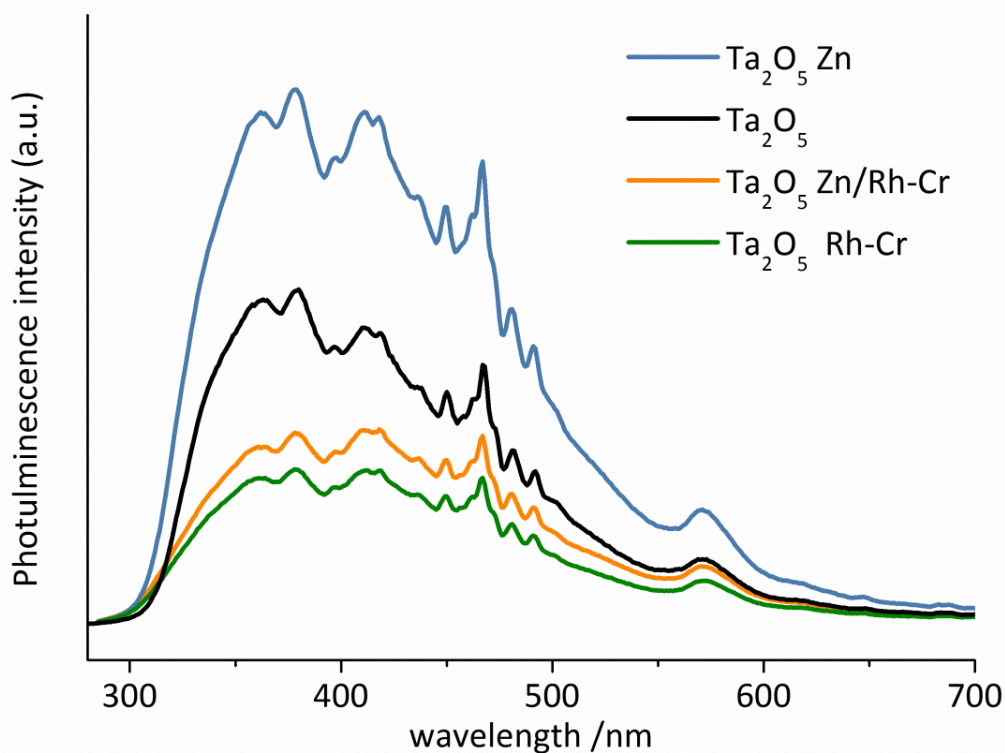


Figure 5-5. Photoluminescence spectrum of Ta₂O₅-based materials. λ_{exc} = 265 nm.

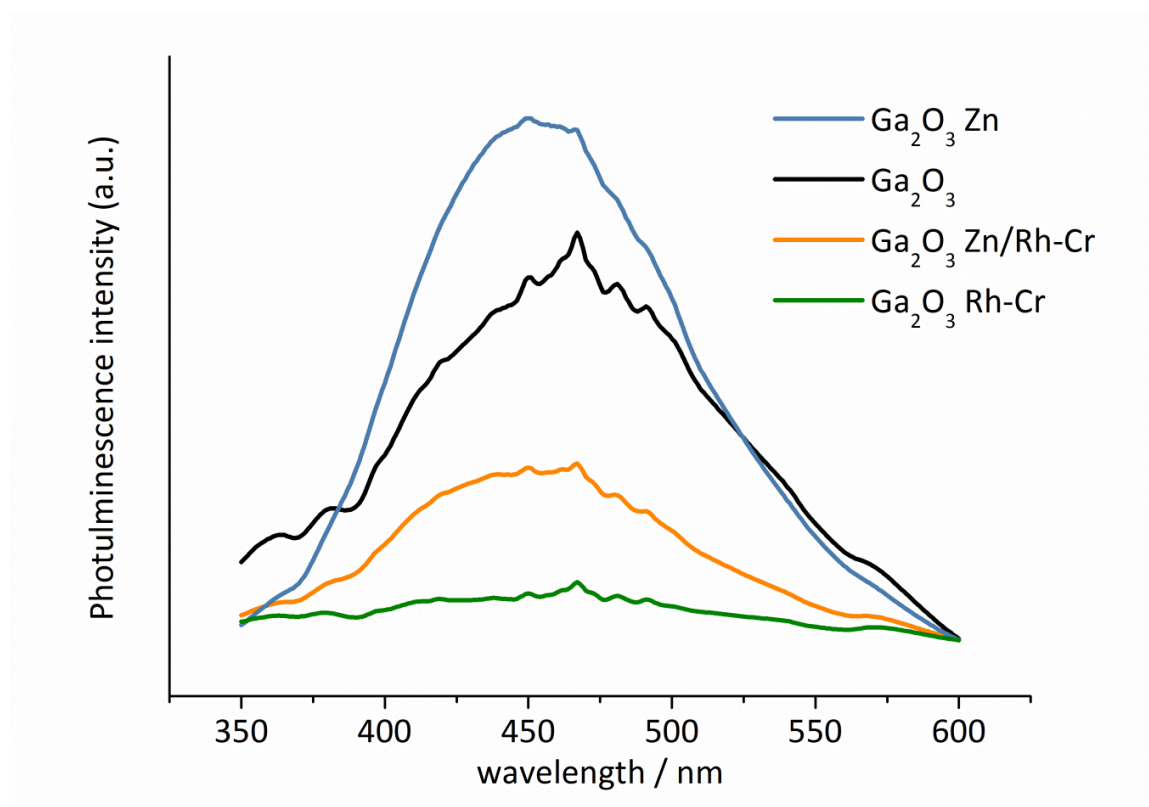


Figure 5-6. Photoluminescence spectrum of Ga_2O_3 -based materials. $\lambda_{\text{exc}} = 265 \text{ nm}$.

Gallium oxide samples (Figure 5-6) display a single emission feature centred at $\lambda = 455 \text{ nm}$, with weak phonon coupling. Stoke shift is large ($\approx 180 \text{ nm}$) and we can exclude the band-to-band nature of this emission. Similar simple emission features were reported in literature and assigned to electron hole recombination mediated by gallium or oxygen defects or vacancies [9, 10].

For tantalum oxide samples (Figure 5-5), features very similar to titania appear to be present but detailed description seems at this stage too speculative due to very limited literature data available.

When we analyse the relative intensity of the emission spectra of each family of catalyst, clear trends can be found. Within each group, a clear decrease in PL intensity was observed upon addition of Rh-Cr co-catalyst. Nevertheless, it must be noted that this effect might not be only due to modified PL features of the supporting

semiconductors. Possibly, self-absorption phenomena might be also involved, since Rh-Cr absorption features consistently overlap with the emission of their support as shown in *section 5.3*.

The most important feature emerging from this analysis is the clear boosting of PL intensity driven by zinc doping. Moreover the enhanced PL emission cannot be correlated with modification of absorption features for Ga and Ta oxides because the absorption characteristics do not sensibly change upon doping (*section 5.3*). This finding could be an important indication of improved stability of charge separation states, promoted by light excitation on Zn doped materials. From another point of view, Zn doping could be preventing electron-hole recombination pathways, which is certainly a desirable property for a photocatalyst. The combined effects of Zn and Rh-Cr for the photoluminescence intensity are consistent for the Ga and Ta oxides samples, in the following order: Zn > bare > Zn/Rh-Cr > Rh-Cr.

The PL results appear to be more complex for TiO₂ materials. Even though Rh-Cr PL-damping effect and Zn PL-boosting effect seems to be similarly present, Zn/Rh-Cr displays the lowest intensity bands in contrast to what was observed for Ga and Ta oxides.

Pt and Zn both similarly boost emission at longer wavelength. In this case this difference could be more simply correlated with their improving effect on absorption (*section 5.3*) rather than their effect on recombination dynamics.

5.4.2 PHOTOLUMINESCENCE DECAYS

Figures 5-7 and 5-8 show photoluminescence decay curves for gallium oxides as it is and promoted with Zn/Rh-Cr ($\lambda_{\text{exc}} = 265 \text{ nm}$; $\lambda_{\text{emi}} = 440 \text{ nm}$). The best fit to the curves was given using double exponential decay functions with millisecond scale decay τ constants. Other Ta and Ti oxides materials were tested in the analogous way, but no decaying signal was detected, probably due to faster decay in the microsecond range (the equipment only allowed sampling at $t > 90 \mu\text{s}$).

Once again, zinc clearly makes a difference in terms of emission decay properties. An order of magnitude increase in the lifetime (both τ_1 and τ_2) is observed upon zinc doping with an impressively long $\tau_2 = 21.7 \text{ ms}$ for $\text{Ga}_2\text{O}_3\text{Zn}$ material as compared to $\tau_2 = 1.78 \text{ ms}$ observed for bare Ga_2O_3 .

Accordingly to what stated in *section 5.4.1*, zinc doping seems to be highly beneficial to the emission properties of gallium oxide material, actively boosting radiative recombination and avoiding faster non-radiative pathways. On the contrary, Rh-Cr addition appears to have a negative effect on lifetime ($\tau_2 = 1.36 \text{ ms}$ on $\text{Ga}_2\text{O}_3\text{Rh-Cr}$) as well as previously shown on luminescence intensity. This effect is highly noticeable in $\text{Ga}_2\text{O}_3\text{Zn/Rh-Cr}$ material ($\tau_2 = 12.4 \text{ ms}$), suffering a 40 % luminescence lifetime shortening as compared to the Rh-Cr free material.

It is also worth mentioning that the overall decay times observed were surprisingly long. Analogous materials were reported in literature to display longest decay constants in the order of magnitude of a hundred μs at 77 K [9].

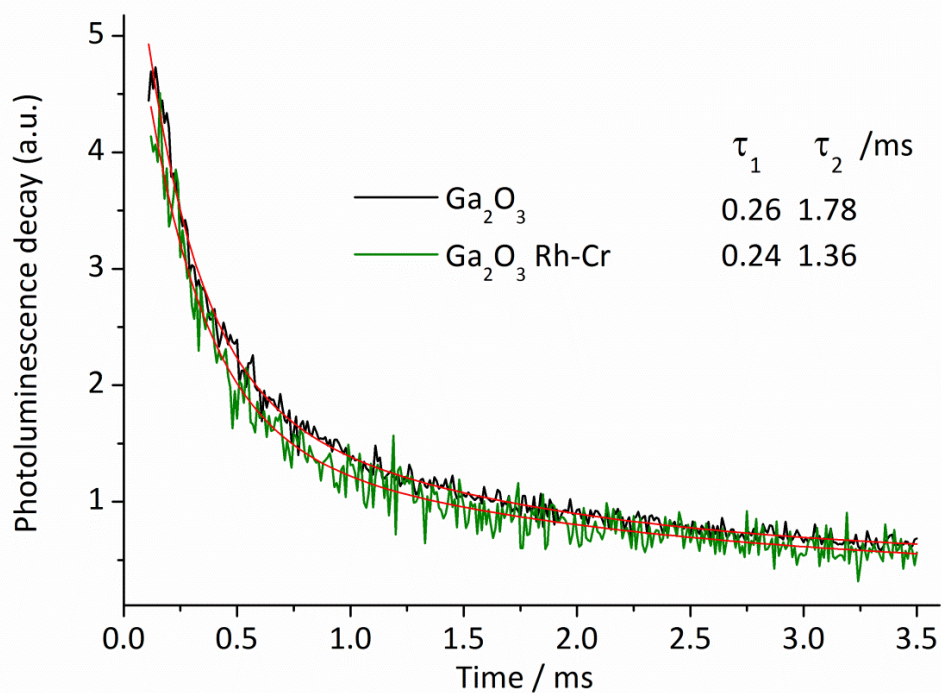


Figure 5-7. Photoluminescence decay of non-zinc-doped Ga_2O_3 -based materials

($\lambda_{\text{exc}} = 265 \text{ nm}$; $\lambda_{\text{emi}} = 440 \text{ nm}$).

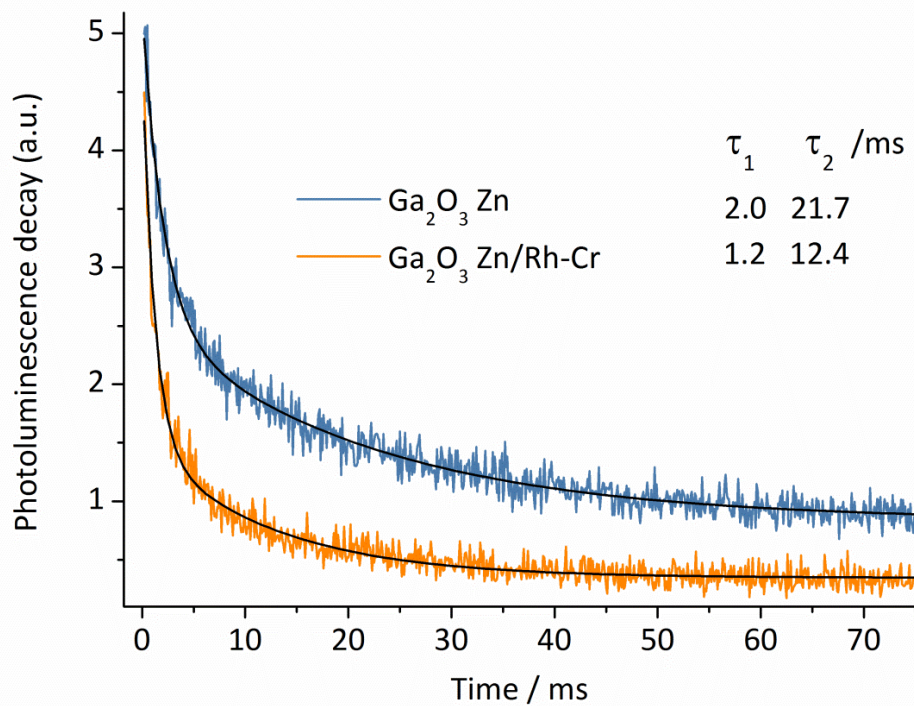


Figure 5-8. Photoluminescence decay of zinc-doped Ga_2O_3 -based materials

($\lambda_{\text{exc}} = 265 \text{ nm}$; $\lambda_{\text{emi}} = 440 \text{ nm}$).

5.5 THE ROLE OF Zn AND Rh-Cr PROMOTERS

According to what collectively observed comparing the photophysical properties upon Zn and Rh-Cr modification, a mechanistic model for PL can be outlined. Clearly Zn doping accounts for both enhancement of PL intensity and decay time. Rh-Cr modification seems to be working in the opposite direction, reducing bare catalysts emission and also counteracting the Zn effect.

A rationalization of the promoter effects is illustrated in Figure 5-9. On the bare catalyst, (Figure 5-9a) photoexcitation produces separated electron-hole couples. A fraction of these can independently migrate and get trapped in different localized states. Ultimately they will recombine either in a non-radiative (red circles) or radiative (yellow circles) way. Upon structural modification by zinc doping (Figure 5-9b) the pathway of charge migration and confinement might be changed and different trapping states could be created. In this model, zinc promoted structures are hypothesized to act blocking non-radiative recombination routes and reversely favours others, populating alternative trap states finally leading to radiative recombination. Instead, Rh-Cr particles are efficient photoexcited electron traps [11]. After Rh-Cr modification (Figure 5-9c), electrons from the conduction band efficiently separates by hopping onto the surface particles rather than on long living emitting trap states. This could account for the observed PL decrease in presence of Rh-Cr particles.

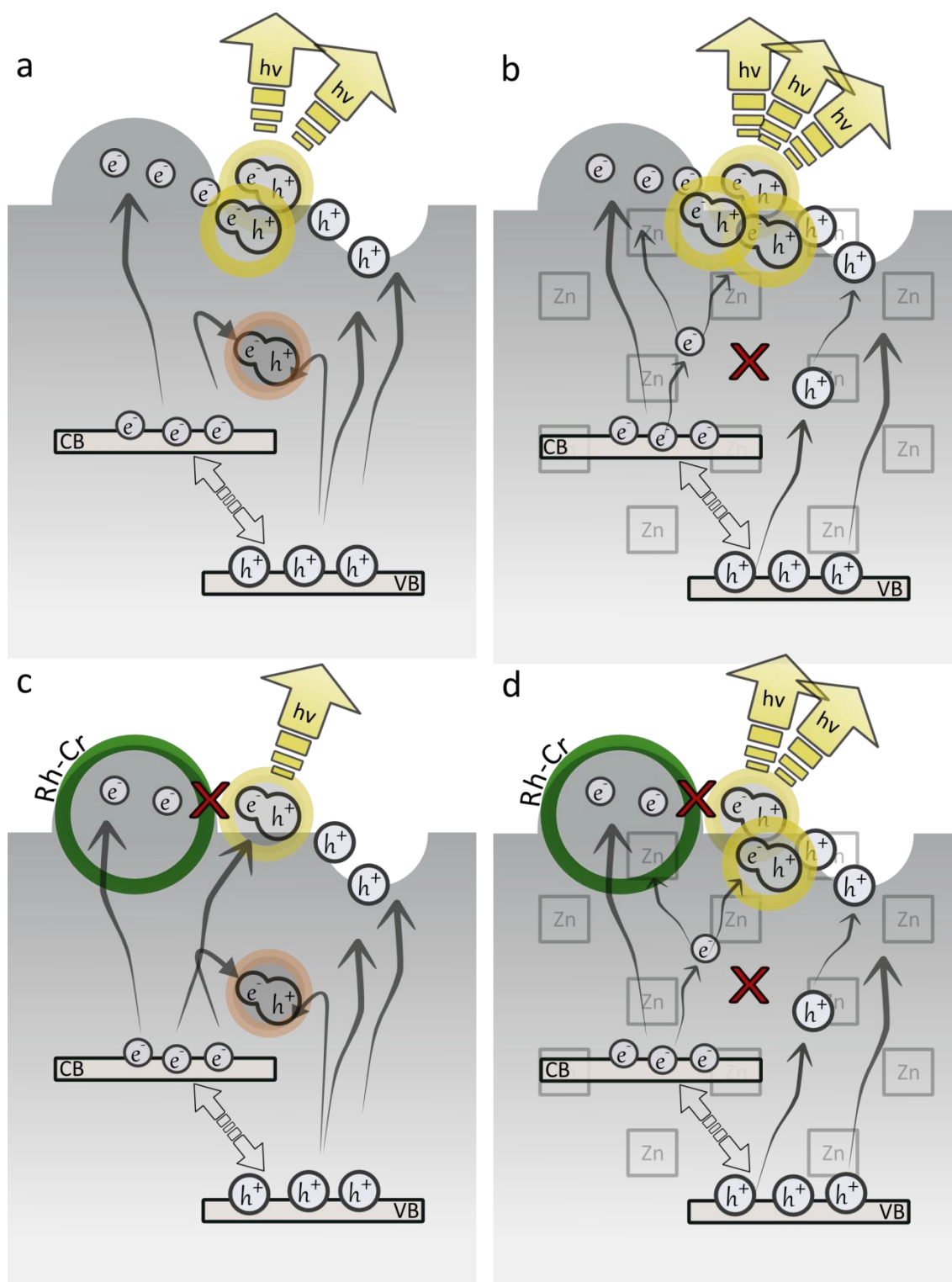


Figure 5-9. Possible PL mechanism on Ga_2O_3 . Difference in hypothesized electron-hole recombination pathways are shown on a) bare Ga_2O_3 , b) $\text{Ga}_2\text{O}_3/\text{Zn}$, c) $\text{Ga}_2\text{O}_3/\text{Rh-Cr}$, d) $\text{Ga}_2\text{O}_3/\text{Zn/Rh-Cr}$. Yellow circles symbolize radiative recombination, red circles the non-radiative ones. The red crosses highlight the impeded recombination pathways after catalyst modification.

By co-modifying the catalyst with both Zn and Rh-Cr the combination of the two effects could be expected (Figure 5-10d). Zn prevents charge recombination and Rh-Cr acts as an electron sink so that PL intensity and lifetime are only partially increased.

By integrating the catalytic results reported in *chapter 4* into this model, we can assign specific roles to Zn and Rh-Cr. Both components contribute in boosting productivity by distinct functions. Indeed, zinc might act as a photoinduced charge recombination buffer, increasing lifetime of charges and also their surface concentration on defect trap states. Rh-Cr most likely acts on a longer timescale in the mechanism and in competition with radiative recombination. More specifically it traps and protects photoexcited electrons from recombination, making them available exclusively for proton reduction. In a nutshell, zinc would be acting as a charge booster, while Rh-Cr would be harvesting electrons and effectively using them for catalysis.

5.6 CONCLUSIONS

In this chapter, the optical photophysical characterization of the three family of materials (Ti, Ta, and Ga oxides) previously used for catalytic testing in *chapter 3* and *4* were presented.

UV-Vis diffuse reflectance spectroscopy was used to determine the bandgap of these materials, which is commonly believed to be a critical parameter for semiconductor based photocatalysis. Values centred at 3.04, 3.78, 3.92, 4.43 eV were obtained for titania, tantalum oxide, sodium tantalate and gallium oxide, respectively. In each family, only relatively little variation to these values was observed upon doping and modification with Zn and Rh-Cr. This infers that bandgap modification is certainly

not a, or at least not only, parameter justifying the high catalytic variability observed for each material family. It is striking how photocatalytic activity seemed to be inversely proportional to the wavelength range the catalyst is capable to harvest. The wider the bandgap, the more efficient appeared to be the catalyst.

Photoluminescence spectroscopy and time resolved photoluminescence decay measurements appeared to be more informative technique. PL intensity of Ta and Ga oxides family could be correlated to catalytic activity. Zn doping was found to have a relevant PL boost effect whereas Rh-Cr had a damping effect. These findings were associated with the possible charge recombination buffering by Zn and to electron trapping by Rh-Cr. The combination of these two effects would beautifully account for the synergetic catalytic activity boost observed for Zn/Rh-Cr modified catalysts.

PL spectroscopic data were further supported by PL decay measurements on Ga_2O_3 family. In agreement with an enhanced excited state lifetime promoted by Zn and a charge sequestration induced by Rh-Cr, the former produced longer PL decay constants, whereas the latter shortened the lifetime of charges.

We demonstrated that PL techniques can be used as tool to rationalize photocatalytic activity. This is of particular relevance since the charge recombination dynamics is possibly the most important factor determining low catalytic rates [12]. It is shown that proper evaluation of PL data and differentiating between doping and co-catalyst effect may become an effective tool to predict catalyst efficiency.

BIBLIOGRAPHY

1. J. B. Varley, J. R. Weber, A. Janotti, C. G. Van de Walle, *Applied Physics Letters* **97**, **2010**.
2. J. N. Kondo, Y. Takahara, D. Lu, K. Domen, *Chemistry of Materials* **13**, 1200, **2001**.
3. J. Robertson, C. W. Chen, *Applied Physics Letters* **74**, 1168, **1999**.
4. Y. Matsumoto, *Journal of Solid State Chemistry* **126**, 227, **1996**.
5. R. López, R. Gómez, *Journal of Sol-Gel Science and Technology* **61**, 1, **2012**.
6. B. Liu, L. Wen, X. Zhao, *Materials Chemistry and Physics* **106**, 350, **2007**.
7. K. Y. Jung, S. B. Park, M. Anpo, *Journal of Photochemistry and Photobiology A: Chemistry* **170**, 247, **2005**.
8. J. Liqiang, Q. Yichun, W. Baiqi, L. Shudan, J. Baojiang, Y. Libin, F. Wei, F. Honggang, S. Jiazhong, *Solar Energy Materials and Solar Cells* **90**, 1773, **2006**.
9. Y. Hou, L. Wu, X. Wang, Z. Ding, Z. Li, X. Fu, *Journal of Catalysis* **250**, 12, **2007**.
10. T. Harwig, F. Kellendonk, *Journal of Solid State Chemistry* **24**, 255, **1978**.
11. K. Maeda, K. Teramura, H. Masuda, T. Takata, N. Saito, Y. Inoue, K. Domen, *The Journal of Physical Chemistry B* **110**, 13107, **2006**.
12. T. Hisatomi, K. Miyazaki, K. Takanabe, K. Maeda, J. Kubota, Y. Sakata, K. Domen, *Chemical Physics Letters* **486**, 144, **2010**.

CHAPTER 6

SUMMARY AND OUTLOOK

6.1 SUMMARY

A continuous flow photoreactor setup was designed and constructed for the investigation of CO₂ photoreduction with H₂O and photocatalytic water splitting, being collectively referred here as *artificial photosynthesis*. In the last decades a considerable amount of research was reported in literature for this class of reactions, as they are holding the promise to produce clean fuel (in form of hydrogen and light hydrocarbons) from abundant and ubiquitous energy resource (sunlight) and reactants (CO₂ and H₂O).

Despite the tremendous amount of knowledge accumulated [1-4], most of the reported catalytic data still rely on a slurry batch reactor approach. Also very common is the use of sacrificial agents to drive the reaction. In order to move towards the direction with actual production configuration in mind, a continuous flow approach was adopted throughout the project. Moreover, use of sacrificial agents was avoided, as it would hardly be compatible with the sustainability of the process we wish to design.

Two kinds of in-house-designed reactors were employed, namely a more conventional dip-pipe stirred slurry reactor and a gas phase reactor. The second kind has been seldom reported in literature. This reactor configuration is of high practical relevance in terms of easier dosing of the reactants and separation of products. For similar reasons, only heterogeneous catalysts and particularly metal oxide powders were investigated. Their photoactivity is believed to arise mostly from the semiconductor band structure, absorbing light at energy equal or higher than the bandgap and promoting electron-hole separation to perform redox reactions at the surface. To date, high overpotentials and charge recombination rates typically restrict high power UV lamps as useful light sources, exciting wide-bandgap semiconductor

materials. Coherently, in our setup we used high pressure Hg discharge lamps (100 to 400 W), as they are the most commonly used UV light sources. Regarding the analytical system, it was designed to quantify the concentrations of products in the effluent gas stream, down to ppm level, and their temporal evolution on the seconds timescale. This task was accomplished by quadrupole mass spectrometry (MS), for which an in-house-designed gas injection system for calibration was installed. Quantification was also verified by micro GC in parallel to MS. This approach allowed accessing the dynamic evolution of gaseous products on a detailed level not obtainable by the classic batch-GC coupled reactor system. Detailed reactor design and development were described in *chapter 2*.

The project was initiated by investigating gas phase photoreduction of CO₂ with H₂O over TiO₂ and Pt/TiO₂ (*chapter 3*). Titania is the most reported photocatalyst in literature since the pioneering work of Honda and Fusishima on photoelectro artificial photosynthesis [5, 6] and represented a good model catalyst for reactor commissioning and detailed mechanistic work. Ppm level hydrogen and methane production was observed under irradiation in continuous flow of water saturated CO₂ at different temperatures (up to 423 K). Detailed study of product concentration profiles with high time resolution allowed observing two distinct catalytic activities: (i) a rapidly deactivating transient activity (few hundreds ppm at $t_{\max} \approx 15$ min) and (ii) a smaller steady state activity (ppm level, only observed for H₂ below 373 K). D₂O isotopic tracing verified that the water vapour fed to the system is the source of the evolved hydrogen (or deuterium). Evidence was collected for D atoms incorporation into methane molecules as well, but no definite picture could be drawn as slow H-D exchange seemed to dominate for this reaction pathway. We also observed that H₂ and CH₄ transient production could be reactivated after long treatment (hours) in the reaction mixture in the dark. Performing programmed dark-light cycles, it was possible

to prove that long dark times (> 15 h) at high temperature (423 K) could restore and even improve the fresh catalyst transient activity. This recovery effect was moreover correlated to carbonate and bicarbonate species accumulation on the surface during the dark time and was clarified by *in situ* DRIFTS. By the same technique, it was possible to identify radical titanol groups ($\text{Ti}^{\text{IV}}\text{OH}^{\bullet}$) as possible intermediates in the hydrogen evolution reaction. Mass spectrometry also elucidated that oxygen was never produced under these conditions. O_2 residual concentration was even observed to drop in the flow stream even on other catalysts (Ta_2O_5), highlighting the presence of recombination reactions.

The scope of catalyst materials were extended to chase the missing oxygen evolution and to achieve better activity in artificial photosynthesis. Ga_2O_3 based materials were finally selected, due to their high overall water splitting activity reported especially upon Zn doping and Rh-Cr promotion [7-9] (*chapter 4*). Quasi-stoichiometric H_2 and O_2 evolution was observed in continuous flow of CO_2 in slurry (up to over 1 % H_2 concentration in the gas stream, $6.3 \text{ mmol}\cdot\text{g}_{\text{cat}}^{-1}\cdot\text{h}^{-1}$) in good agreement with literature batch data. Continuous flow gas phase testing in H_2O saturated CO_2 showed that the water splitting activity is substantially unchanged at 323 K but rapidly degrades at higher temperature. This was interpreted in relation to the fact that the reaction is limited by the surface water concentration (condensation) in response to temperature increase, similarly to what we also reported for titania. We also observed that this temperature dependency can be reversed by K promotion (5 wt% K impregnation on Ga_2O_3 Zn/Rh-Cr), although at the cost of a diminished average productivity.

The effects of Zn doping, Rh-Cr deposition, and Zn/Rh-Cr co-modification to Ga_2O_3 were independently studied using the slurry reactor. The activity was found to be enhanced at each modification step, according to the given sequence. Remarkable

activity boosts were found after Rh-Cr deposition and after Zn/Rh-Cr co-modification. Especially the latter combined modification produced a synergetic activity boost not explainable as a simple sum of Zn and Rh-Cr independent effects. The same modification was applied to other catalysts such as Ta₂O₅ and TiO₂ which we previously proved to be capable of H₂ evolution but could not generate O₂. Even though Ta₂O₅ and TiO₂ reached only 10 % and 0.4 %, respectively, of the maximum activity of Ga₂O₃ based materials, very similar improving trends upon the promotion were observed along the series. Quasi-stoichiometric oxygen evolution was observed upon Rh-Cr and Zn/Rh-Cr modification on Ta₂O₅. Similar improving effects of Zn/Rh-Cr modification to very different materials suggested an underlying similar working and promotion mechanisms. Contrarily to our expectations, no hydrocarbon evolution was observed along with the efficient water splitting under the conditions we investigated.

By means of UV-Vis diffuse reflectance spectroscopy and photoluminescence (PL) spectroscopy, correlations were found between the photophysical property of the catalyst materials and catalytic activity (*chapter 5*). PL intensity and lifetime boosting effect upon Zn doping was hypothesised to be associated to its non-radiative recombination buffer action. On the other hand, Rh-Cr PL damping effect was interpreted by the efficient surface electron trapping properties. Moreover, bandgap determination (based on diffuse reflectance spectra) allowed pointing out the absence of correlation between this parameter and the boosting in catalytic activity by Zn and Rh-Cr promotion. The actual validity of such a widely reported parameter and its influence on effective light harvesting mechanism was questioned.

In conclusion, the continuous flow system designed and improved through this project allowed the discovery of new mechanistic insight even on a well-known photocatalyst as titania. This catalyst was proven to be capable, even though mostly

working in an intermittent fashion relying on dark-light cycles, to produce hydrogen and methane using only CO_2 and H_2O in continuous flow and under UV irradiation. Moreover, the need to verify the closed catalytic cycle by showing H_2O oxidation to produce O_2 led us to explore the state-of-the-art water splitting catalysts based on Ga and Ta oxides. Having succeeded in this last task, we could not at the same time progress the parallel CO_2 reduction as hoped. Based on this experimental evidence it is likely that the presence of good hydrogen evolution centres does not necessarily correlate with an improvement in carbon dioxide reduction pathways.

6.2 OUTLOOK

6.2.1 OPEN CHALLENGES

In artificial photosynthesis, many challenges are still open and many have to be overcome before the technology becomes competitive in the energy market. Focusing on the water splitting, considerable forward steps were undoubtedly made in the last decade. From only sacrificial agent driven reactions to overall stoichiometric H_2 and O_2 from pure water, productivity climbed up four orders of magnitude in the last ten years. A further increase of less than two orders of magnitude would be sufficient to render this energy production approach competitive.

However major drawbacks of active catalysts still exist, drawing great attention of the research community. Firstly, extension of active light wavelength range is necessary, as harvesting and converting visible and NIR light would tremendously improve the surface energy density collected from the sun. Secondly, oxygen separation represents an important limitation to overcome. In order to separate solar fuel from oxygen, two major strategies can be advised. In one, catalysts efficiently

produce H_2 and O_2 from water and a gas-separation device (involving selective membranes or chemical traps for either component) is used to separate the two reactive gases. In the other, an alternative reactor design is used to allow the production of H_2 and O_2 at geometrically different sites. The latter mode would require physically separate oxidation and reduction sites, as well as a unidirectional charge transport system. This can be achieved by applying chemical potential on physically separated catalysts in a photoelectrochemical device (PEC). Another approach is to employ two different photocatalysts to separate oxidation and reduction reactions, and mediate charge transfer between the two by chemical redox couples in solution (Z-scheme design [1]). The added cost and thus feasibility of such processes would vary depending on the separation device for the first case and the complexity of reactor systems for the second case.

Direct water- CO_2 photocatalytic reduction technology seems to be improving more slowly as compared to water splitting technology. The reaction pathway being certainly more complex and thermodynamically also unfavoured, only relatively small improvements have been made during 40 years of investigation. New solution might be arising from novel reactor designs (PEC design as the best example) [10-12]. Another effective approach could be performing the photocatalytic CO_2 reduction as separate steps (e.g. first hydrogen production, then CO_2 hydrogenation). As photocatalytic water splitting (or photoelectrolysis) is getting more efficient day by day, the solar-produced hydrogen could be used in a separate catalytic step to drive CO_2 reduction over a different catalyst specifically designed for the task.

Dealing with the above challenges, an overview of the current investigation front in development in our lab will be given in the next sections.

6.2.2 GaN:ZnO Rh-Cr CATALYST FOR VISIBLE LIGHT HARVESTING

One of the most impacting breakthrough in visible light driven photocatalytic water splitting was certainly Maeda-Domen's Rh-Cr modified GaN:ZnO solid solution catalyst [10-12]. Synthesized by nitridating a mixture of Ga₂O₃ and ZnO for 15 h in NH₃ flow, it performs overall water splitting at a high rate (up to 320 μmol·g_{cat}⁻¹·h⁻¹, H₂ based) under λ > 400 nm visible light irradiation. Although its activity is an order of magnitude below the best reported wide-bandgap photocatalysts, the extended useful solar spectrum absorbed by such materials made the discovery an important step forward.

In our lab, we also attempted the synthesis of this material and tested it in the continuous flow slurry reactor. Figure 6-1 shows the wavelength dependence on H₂ productivity, obtained by an analogous test as described in *section 4.3.5*.

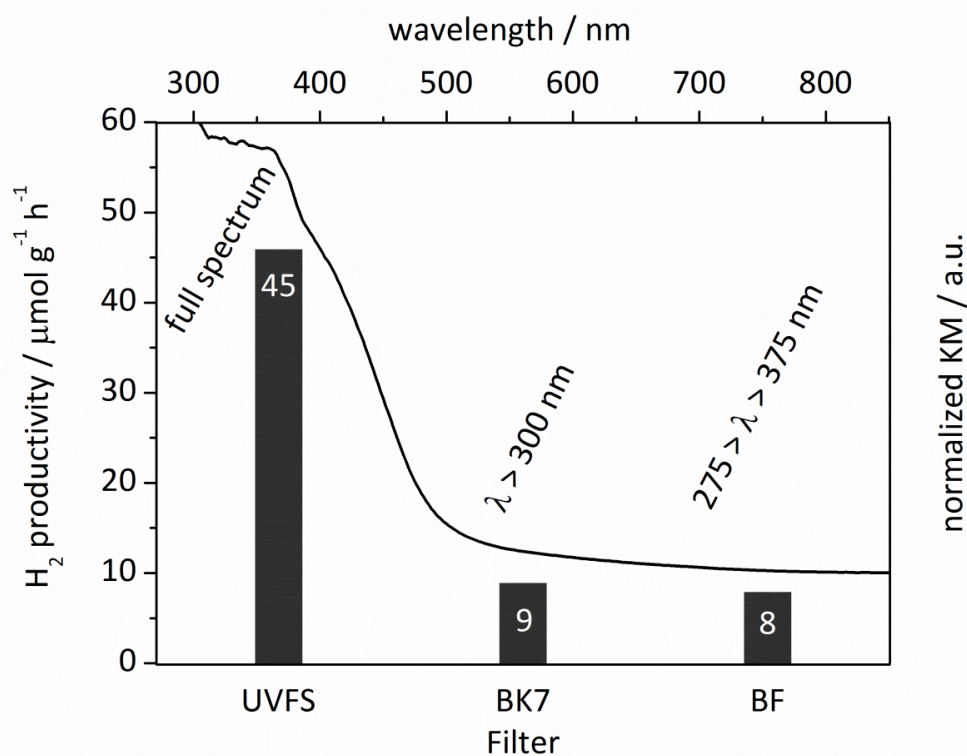


Figure 6-1. H₂ productivity dependence on light filtering (left and bottom axes) for GaN:ZnO Rh-Cr tested in slurry. The diffuse reflectance spectrum of the material is superimposed (top and right axes).

Hydrogen and oxygen evolution was observed but the activity, even under UV-to-visible range excitation, was much lower than those observed for Zn/Rh-Cr Ta and Ga oxides (max $45 \mu\text{mol}\cdot\text{g}_{\text{cat}}^{-1}\cdot\text{h}^{-1}$ vs. $\text{mmol}\cdot\text{g}_{\text{cat}}^{-1}\cdot\text{h}^{-1}$ range, *chapter 4*). This is possibly due to a poor reproduction of the material synthesis reported in literature. Nevertheless, as shown in Figure 6-1 and consistently with literature [12], the bandgap shifts (2.4 eV, evaluated by Tauc method). However, the enhanced absorption features of this material did not match the wavelength dependency of the catalytic activity, which looked to be once again mainly UVC driven. This can be deduced from the fact that activity was maximum ($45 \mu\text{mol}\cdot\text{g}_{\text{cat}}^{-1}\cdot\text{h}^{-1}$) and was equally reduced to 20 % in both $\lambda > 300$ and $275 < \lambda < 375$ nm ranges.

These preliminary results indicate that visible light excitation could have just a marginal effect on the activity and likely also on the reaction mechanism. Further mechanistic insights are needed in order to design better visible light photocatalyst and to understand critical elements of catalytic activity, which are likely different from bandgap of catalyst materials.

6.2.3 PEC CELL

A PEC cell has been designed and built with the goal to explore the possibility of separate evolution of oxygen and hydrogen, as well as simultaneous cathodic CO_2 reduction in continuous flow.

The cell, shown in Figure 6-2, adapts a water electrolyser based design to photocatalytic application, by opening a fused silica port on the cathodic side. The core of the electrolyser is composed by a pair of steel round electrodes sandwiching a 175 μm thick *Nafion*[®] 117 proton exchange membrane (PEM) on top of which (photo-) cathodic and anodic catalyst are spray-deposited. *Teflon* sealing elements join the electrodes to the outer cell body compartments (anodized aluminium) bearing

connection for flow of either liquid water (anode) or CO₂ gas (cathode). Channels are present on these body compartments to insert heating cartridges for cell heating. Operation temperature was set at 353 K, optimum for *Nafion*[®] 117 polymer for good proton conductivity.



Figure 6-2. PEC cell design project (bottom) and assembled cell ready for testing (top)

Such a configuration gives a number of theoretical advantages as compared to the purely photocatalytic one. Oxygen could be selectively produced on the anodic side, with obvious separation and recombination reaction prevention advantages. Hydrogen production could be boosted on the cathodic side (as compared to the *only photo* approach) by increasing the reductive potential of the photocatalyst. CO₂ reduction in high hydrogen concentration could be triggered in presence of multiple catalytic, photo and electro stimuli.

Preliminary testing was performed using N₂ or CO₂ as carrier and reacting gas respectively (4.5 ml/min) flowing on the cathodic side of the cell (Figure 6-3). 200 W mercury lamp was used as light source (*photo* contribution) and a potentiostat was used as electrical power supply (*electro* contribution, potential fixed at 2.5 V). Catalysts were deposited on a *Nafion*[®] 117 membrane: anode side IrO₂, cathode side Ga₂O₃ Zn/Rh-Cr (loading 2 mg/cm²).

Analysing the results shown in Figure 6-3, a similar behaviour could be seen for H₂ production in either N₂ or CO₂ flow when applying only *photo*, *electro* or both *photo* and *electro* stimuli. In the *photoelectro* case activity appears as the mere sum of the contribution of the two separated stimuli considered (no synergetic *photoelectro* effect is present). Relatively high *photo* activity could be accounted by the fact that *Nafion*[®] 117 membranes are easily wettable and water could be transported through it from the anode side. Evidence of trace level but stable CH₄ production (ca. 5 ppm) is visible under *photo* and *photoelectron* stimulation in CO₂, and this is not observed using N₂ flow. This suggests that, although very limited, CO₂ reduction activity is present under irradiation in the PEC configuration. The data does not allow to determine whether the *photoelectro* approach gave any increased CO₂ conversion as compared to the *photo* one. It is however clear that *electro* stimulus alone does not drive the reaction.

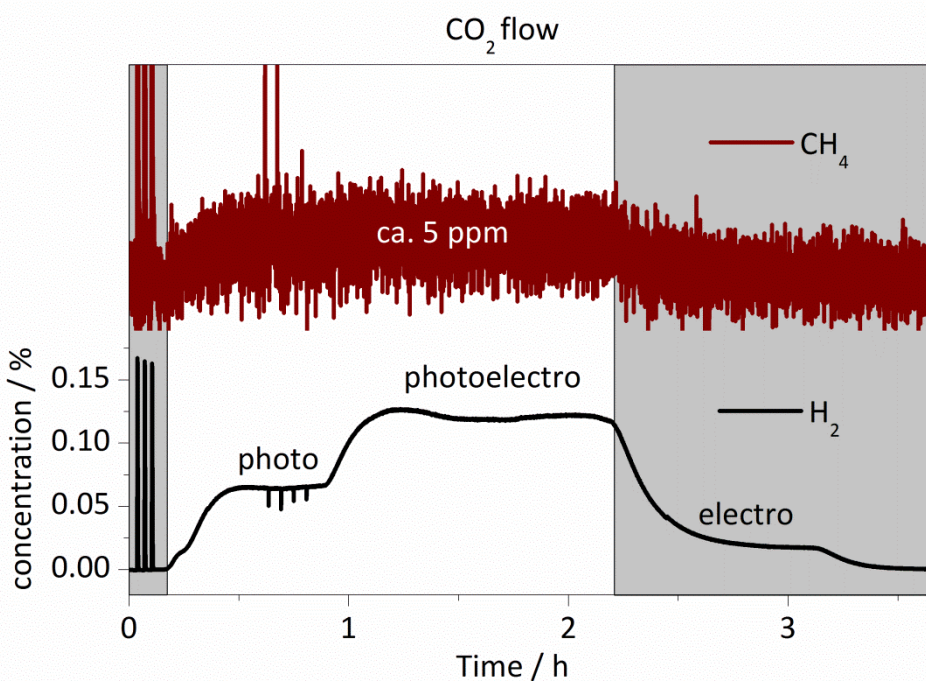
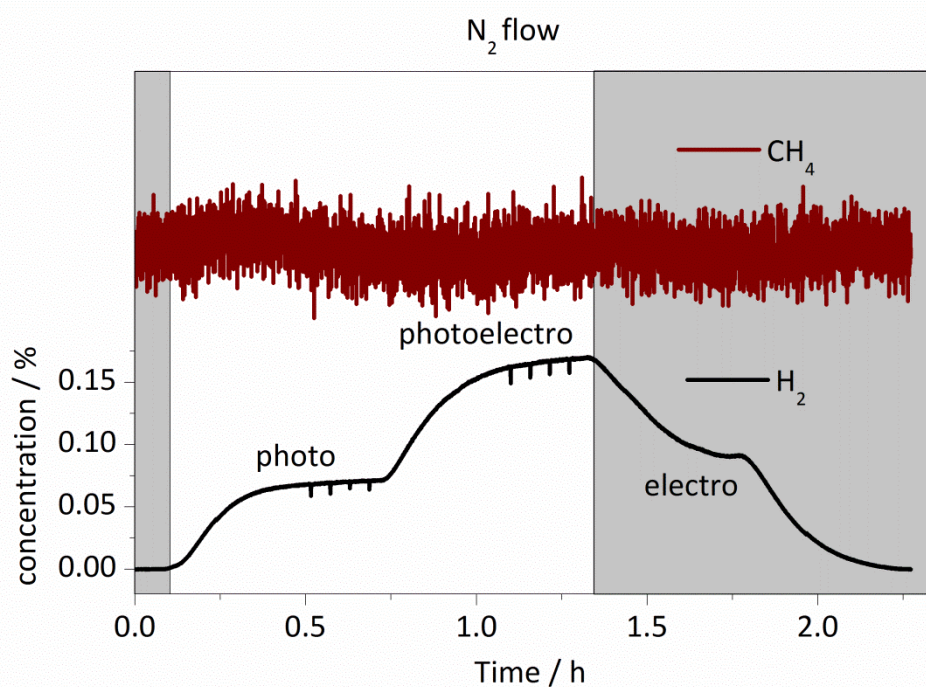


Figure 6-3. H₂ (black) and CH₄ (red) concentration profiles during activity test by passing different gases over the cathode catalyst in the PEC cell: N₂ flow (top) or CO₂ flow (bottom). Shaded regions highlight the part of the experiment without irradiation. For clarity, photo-, electro- and combined photoelectro-contributions are noted.

6.2.4 METAL OXIDE NANOPOROUS MEMBRANES

Perfluorinated polymer membranes like *Nafion*[®] used in the previous section are the most tested and widespread as PEM. They could be conveniently employed in cell electrolyzers for small bench size hydrogen producing units. However, such materials suffer from important drawbacks that limit their utilisation to special small-scale applications. Especially their rather low thermal stability important for high proton conductivity limits their use at temperatures typically below 400 K.

Metal oxide materials possessing a nanosized porous structure have hypothesized to be the candidates to meet both the requirement of products separation (working as selective membranes) and photocatalytic properties [13-15]. The inorganic nature would furthermore offer a better thermal stability. Titania nanotubes are certainly among the most studied materials that could be applied for this aim [16].

Formation of vertically oriented hollow structures with typical diameter in the range of 100 nm and length up to hundreds of μm can be prepared by electrochemical methods. Typically, a clean titanium metal foil is anodized in a viscous organic medium, such as ethylene glycol (EG), in presence of water and fluoride ions as metal scavenging agents, driving oxidation and the channel formation. High voltage (12-90 V) is necessary to produce nanotube formation and control their formation rate and nanostructure. Careful control over concentration of water and fluoride is important and determines the final structure.

Figure 6-4 summarizes one of the results we obtained by applying these techniques to a titanium plate. Previous to anodizing the plate was selectively etched in the middle square section with 5 % NH_4F solution on concentrated phosphoric acid in order to reduce the thickness of its central part. This titanium foil was anodized in EG solution (containing 0.3 % NH_4F and 2 % water) for 24 h with the outer frame portion

protected by a tape. Both faces of the foil were subjected to the treatment at the same time, placing the Ti anode in between two distinct Ti wires acting as cathodes. The final result of the anodising process is a self-standing semi-transparent TiO_2 material (confirmed by EDX analysis) framed by metallic Ti. Nanotube array formation with average diameter of 75 nm was confirmed by SEM.

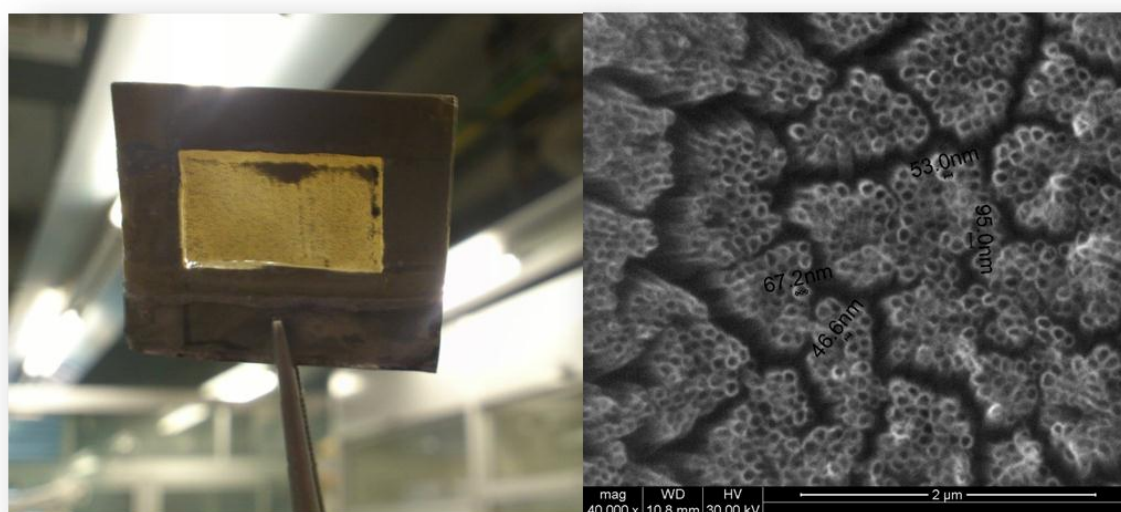
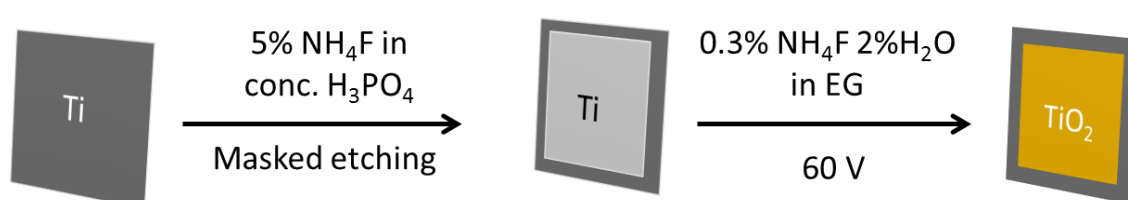


Figure 6-4. Titania nanotube structure prepared with masking technique. Preparation steps are shown at the top. Resulting Ti-framed TiO_2 membrane (bottom left) and SEM image of the nanotube array (bottom right) are shown.

The largest drawback of these structures at present is their fragility. When this structure are prepared anodising a single face of metal support (as mostly reported in literature), delicate water swelling and sonication procedures have first to be applied

to detach the oxidized layer from the bulk unoxidized metal. Moreover the subsequent drying procedure can seriously damage the material leading to breakage and crumbling. Supercritical CO₂ drying can improve the stability of the structure, but the general mechanical properties of such materials needs to be improved.

Another family of similar materials which can in the future better meet these demands are non-thickness limited (NTL) anodised thin metal foils [17-19]. As titania nanotubes, these structures can be formed by high voltage anodising but using viscous glycerol/phosphate solution as electrolyte. This technique suits a larger variety of metals besides Ti (e.g. Nb, Ta, Fe, Zr), and can be finely tuned to obtain much more mechanically resistant (also bendable) oxide structures with defined porosity. By varying the applied potential, different kinds of porous structures can be prepared (e.g. disordered mesopores or aligned channels) with great hopes for new types of photo and electrocatalytic materials.

BIBLIOGRAPHY

1. R. Abe, *Journal of Photochemistry and Photobiology C: Photochemistry Reviews* **11**, 179, **2010**.
2. A. Dhakshinamoorthy, S. Navalon, A. Corma, H. Garcia, *Energy & Environmental Science* **5**, 9217, **2012**.
3. S. N. Habisreutinger, L. Schmidt-Mende, J. K. Stolarczyk, *Angewandte Chemie International Edition* **52**, 7372, **2013**.
4. Y. Izumi, *Coordination Chemistry Reviews* **257**, 171, **2013**.
5. A. Fujishima, K. Honda, *Bulletin of the Chemical Society of Japan* **44**, 1148, **1971**.
6. A. Fusishima, K. Honda, *Nature* **238**, 37, **1972**.
7. Y. Sakata, Y. Matsuda, T. Nakagawa, R. Yasunaga, H. Imamura, K. Teramura, *ChemSusChem* **4**, 181, **2011**.
8. Y. Sakata, Y. Matsuda, T. Yanagida, K. Hirata, H. Imamura, K. Teramura, *Catalysis Letters* **125**, 22, **2008**.
9. Y. Sakata, T. Nakagawa, Y. Nagamatsu, Y. Matsuda, R. Yasunaga, E. Nakao, H. Imamura, *Journal of Catalysis* **310**, 45, **2014**.
10. K. Maeda, K. Domen, *Chemistry of Materials* **22**, 612, **2010**.
11. K. Maeda, T. Takata, M. Hara, N. Saito, Y. Inoue, H. Kobayashi, K. Domen, *Journal of the American Chemical Society* **127**, 8286, **2005**.
12. K. Maeda, K. Teramura, D. Lu, T. Takata, N. Saito, Y. Inoue, K. Domen, *Nature* **440**, 295, **2006**.
13. G. K. Mor, K. Shankar, M. Paulose, O. K. Varghese, C. a. Grimes, *Nano letters* **5**, 191, **2005**.
14. S. C. Roy, O. K. Varghese, M. Paulose, C. A. Grimes, *ACS Nano* **4**, 1259, **2010**.
15. O. K. Varghese, M. Paulose, T. J. Latempa, C. a. Grimes, *Nano letters* **9**, 731, **2009**.
16. G. K. Mor, O. K. Varghese, M. Paulose, K. Shankar, C. a. Grimes, *Solar Energy Materials and Solar Cells* **90**, 2011, **2006**.
17. D. Kowalski, D. Kim, P. Schmuki, *Nano Today* **8**, 235, **2013**.
18. D. Kim, K. Lee, P. Roy, B. I. Birajdar, E. Spiecker, P. Schmuki, *Angewandte Chemie International Edition* **48**, 9326, **2009**.
19. K. Lee, P. Schmuki, *Electrochemistry Communications* **13**, 542, **2011**.

SHORTHANDS AND GLOSSARY

AM 1.5: air mass coefficient 1.5, standard used in relation to the average sunlight energy reaching the Earth's crust after crossing the atmosphere. AM 1 corresponds to the zenith optical path of sunlight to Earth (limited to tropical regions). AM 1.5 is representative of a 1.5 times thicker atmospheric layer path: it better describes light intensity at mid latitudes (ca. 45°) and it is the standard adopted in solar simulators.

CB: conduction electronic band.

COP16: 16th edition of Conference of the Parties of the United Nations Framework Convention on Climate Change, Cancun, Mexico, 2010.

Dark time: period during a catalytic test, when no irradiation is applied to the catalyst; applied to investigate the recovery of catalytic activity.

DRIFTS: diffuse reflectance infrared Fourier transform spectroscopy.

dw-CO₂: deuterated-water saturated carbon dioxide (gas).

E_g: bandgap of a material i.e. the energy difference between VB and CB, usually expressed in electronvolt (eV).

EPR: electron paramagnetic resonance.

GC: gas chromatography (or chromatographer).

GHG: greenhouse gas.

HER: hydrogen evolution reaction.

HPLC: high pressure liquid chromatography (or chromatographer).

IR: infrared light radiation with wavelength ca. $\lambda > 800$ nm.

MCT: mercury-cadmium-telluride high sensitivity liquid N₂ cooled detector for IR spectroscopy.

MFC: mass flow controller, device used to deliver an adjustable and precise gas flow rate as feed of a reactor component.

MID: multiple ion detection mode, an MS operating mode allowing for fast close-to-simultaneous tracking of a number of charged atomic or molecular fragments of different m/e ratio.

MS: mass spectrometry (or spectrometer).

NIR: near-infrared light radiation with wavelength ca. $800 > \lambda > 1400$ nm.

OER: oxygen evolution reaction.

PEC cell: photoelectrochemical cell.

PID: proportional-integral-derivative controller, used in thermal control devices.

PL: photoluminescence.

PMT: photomultiplier tubes (detector).

UNFCCC: United Nations Framework Convention on Climate Change.

UV: ultraviolet light radiation with wavelength ca. $\lambda < 400$ nm.

UVC: high energetic ultraviolet light radiation with wavelength ca. $280 < \lambda < 100$ nm.

VB: valence electronic band.

Vis: visible light radiation with wavelength $400 > \lambda > 800$ nm.

w-CO₂: water saturated carbon dioxide (gas).

LIST OF PUBLICATIONS

Journal publications

“Origin of Photocatalytic Activity in Continuous Gas Phase CO₂ Reduction over Pt/TiO₂”

Antonio Bazzo and Atsushi Urakawa, *ChemSusChem*, **2013**, 6, 2095

“Effect of Zn and Rh-Cr promoters over wide-bandgap semiconductor oxides of Ga, Ta and Ti for continuous flow water splitting reaction”

Antonio Bazzo and Atsushi Urakawa, manuscript in preparation

Conference contributions

“Impact of high pressure and K and Ba promoters on CO₂ hydrogenation over Cu/Al₂O₃ catalysts”

Atul Bansode, Antonio Bazzo and Atsushi Urakawa, 15th International Congress on Catalysis (15th ICC), Munich (Germany), *Jul-2012*. Poster contribution.

“Steady and Transient Activities in Continuous Gas Phase Photocatalytic Reduction of CO₂ over Pt/TiO₂”

Antonio Bazzo and Atsushi Urakawa, 11th European Congress on Catalysis (EuropaCat-XI), Lyon (France), *Sep-2013*. Poster contribution.

“Steady and Transient Activities in Continuous Gas Phase Photocatalytic Reduction of CO₂ over Pt/TiO₂”

Antonio Bazzo and Atsushi Urakawa, 6th Asia-Pacific Congress on Catalysis (APCAT-6), Taipei (Taiwan), *Oct-2013*. Oral presentation contribution.

CURRICULUM VITAE

Tarragona (Spain), 20th May 2014

Name: ANTONIO BAZZO

Date of birth: 07/07/1985

Place of birth: TREVISO, ITALY

Nationality: ITALIAN

1- Education and position

19th July 2007

B.Sc. in **Chemistry** (180 ECTS) at Università degli Studi di Padova (Unipd), Italy.

Final evaluation 110/110 cum laude.

25th March 2010

Master (M.Sc.) in **Chemistry** (*Molecular Sciences*, 120 ECTS) at Università degli Studi di Padova (Unipd), Italy.

Final evaluation 110/110 cum laude.

25th May 2010 – now

Currently working as a PhD student in the Institute of Chemical Research of Catalonia (ICIQ), Tarragona, Spain under the supervision of Dr. Atsushi Urakawa.

The main research focus is heterogeneous photocatalytic conversion of CO₂ into valuable chemical compounds.

2 - Participation to Research Projects

April-July 2007: first level degree laboratory project

Study title: *“Synthesis and optical properties of siliceous films embedding a complex of Ir(III) with Bis-(4,5-biphenyl-2methyl-thiazole)and 5-methyl-1,10-phenantroline.”*

Chemical Science Department, Unipd, Italy.

Supervisor: Ch. Prof. Eugenio Tondello.

April 2009 – March 2010: master thesis project

Study title: *“Synthesis and characterization of single wall carbon nanotubes-pyrene derivatives”.*

Organic Synthesis and Materials Laboratory, Chemical Science Department, Unipd, Italy

Supervisor: Dr. Enzo Menna

3 - Grants

1st September 2008 –15th January 2009

Erasmus exchange student grant for a study period abroad in Europe.

Hosting institute: University College Dublin (UCD), Dublin, Ireland.

Erasmus exchange responsible: Prof. Rory More O’Ferral

25th May 2010 – now

ICIQ predoctoral fellowship, Institute of Chemical Research of Catalonia (ICIQ), Tarragona, Spain.

Supervisor: Dr. Atsushi Urakawa

4 - Participation to seminars and congresses

7-9th September 2010

1st Thomas Young Centre (TYC) Energy Material Workshop, Department of Chemistry of University College London (UCL).

Attendance to the whole seminar sessions and poster sessions.

29th June – 1st July 2011

Sociedad Española de Catálisis (SECAT) congress, Saragoza.

Attendance to the full congress oral presentations and poster sessions.

1st-6th July 2012

15th International Congress on Catalysis 2012 (ICC), Munich.

Co-author in a poster contribution: "Impact of High Pressure and K and Ba promoters on CO₂ Hydrogenation Over Cu/Al₂O₃ catalysts"

A. Bansode, A. Bazzo, A. Urakawa.

1st September – 6th September 2013

11th European Congress on Catalysis (XI Europacat), Lyon.

First author in a poster contribution and presenting the latter in the poster sessions:

Continuous Gas Phase Reduction of CO₂ over Pt/TiO₂ Photo-catalyst

A. Bazzo, A. Urakawa

Attendance to the full congress oral presentations and poster sessions.

13th September – 17th September 2013

The 6th Asia-Pacific Congress on Catalysis (APCAT-6), Taipei.

Oral presentation contribution:

*“Steady and Transient Activities in Continuous Gas and Liquid Phase Photocatalytic
Reduction of CO₂ over Pt/TiO₂”*

A. Bazzo and A. Urakawa

Attendance to the full congress oral presentations and poster sessions.